Universitat de Girona

Rakibul Hasan

Microstructural Analysis of Materials for Liquid Hydrogen (LH_2) Storage Tank

FRP++
Advanced structural analysis and design using composite materials

Master Dissertation
European Master Advanced Structural Analysis and Design using Composite Materials

Work developed under the supervision of
Professor Dr. Jordi Renart Canalias
Professor Dr. Jose Manuel Guerrero Garcia
Mayerlin Salgado Piamba, PhD Candidate

Funded by the European Union

September 2026

DECLARATION

Name: Rakibul Hasan

Email: rakibul.hasan.contact@gmail.com **Phone number:** +34610036685

Citizen Card Number: N/A

Title of the Dissertation: Microstructural Analysis of Materials for Liquid Hydrogen (LH_2) Storage Tank

Supervisors:

Professor Dr. Jordi Renart Canalias

Professor Dr. Jose Manuel Guerrero Garcia

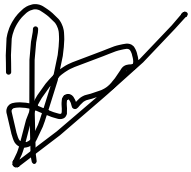
Mayerlin Salgado Piamba, PhD Candidate

Year of Conclusion: 2026

Master Course in Advanced Structural Analysis and Design using Composite Materials

THE ENTIRE REPRODUCTION OF THIS DISSERTATION IS AUTHORIZED ONLY FOR RESEARCH PURPOSES, UPON WRITTEN DECLARATION BY THE INTERESTED PERSON, WHICH IS COMMITTED TO.

University of Girona, 01/09/2026

Signature: 

Acknowledgements

All praise is due to Almighty Allah, the Most Gracious and the Most Merciful, for granting me the health, patience and strength to carry out and complete this work.

My thanks go to my supervisor, Professor Jordi Renart, for his guidance throughout this work and for the trust he placed in me to see it through. I am equally grateful to Professor Jose Manuel Guerrero, whose detailed feedback and patience with the finite element modelling improved this thesis at every stage, and to Mayerlin Salgado, who provided the computed tomography data and was generous with her time whenever I asked. Working alongside them has been the most rewarding part of this experience.

I am thankful to the FRP++ consortium for the opportunity to take part in this master's programme and for all it has allowed me to learn. I would also like to thank the AMADE group at the University of Girona for the welcome I received and for the facilities and support that made this work possible.

To my friends, both those I met during the programme and those who cheered me on from home, thank you for the company and the encouragement, and for keeping things in perspective when the work was hard.

Above all, I thank my parents and my family. Their constant support and belief carried me through, and this work is as much a result of their patience as of my own effort. To them, and to everyone who wished me well along the way, thank you.

Resumen

El hidrógeno líquido es un combustible prometedor para una aviación de bajas emisiones de carbono, pero su almacenamiento a unos 20 K exige paredes de tanque ligeras que se mantengan íntegras a temperatura criogénica. En un material compuesto reforzado con fibras, la matriz polimérica se contrae mucho más que las fibras durante el enfriamiento, y este desajuste genera tensiones residuales a la escala de las fibras que pueden nuclear microgrietas y comprometer la integridad estructural de la pared. Esta tesis desarrolla una metodología basada en microtomografía computarizada de rayos X que predice la respuesta termomecánica efectiva de un compuesto de fibra corta directamente a partir de su microestructura medida, de modo que puedan evaluarse distintas configuraciones de material sin fabricar y ensayar una probeta para cada una. El material estudiado es un compuesto de poliamida 11 reforzado con fibra corta de basalto, fabricado por fabricación aditiva, candidato para el revestimiento interior (liner) de un tanque criogénico de doble pared del proyecto OVERLEAF.

Se segmenta un único escaneo de micro-CT y se identifican sus fibras, con lo que se obtienen la longitud, el diámetro y la orientación de cada fibra. Las distribuciones de probabilidad ajustadas a estas magnitudes alimentan un esquema de Monte Carlo que genera un elemento de volumen representativo (RVE) a la fracción volumétrica de fibra objetivo, que se homogeneiza mediante el método de elementos finitos. Al enfriarlo desde 293 K hasta 20 K se obtiene el coeficiente de dilatación térmica direccional, del orden de 6×10^{-5} por kelvin y ligeramente anisótropo, junto con las tensiones térmicas residuales. El método se implementa como un único script reutilizable cuyos parámetros estadísticos y fracción volumétrica pueden modificarse para modelar otro sistema de fibra corta.

PALABRAS CLAVE: almacenamiento de hidrógeno líquido; poliamida 11 reforzada con fibra de basalto; tomografía computarizada de rayos X; elemento de volumen representativo; coeficiente de dilatación térmica.

Resum

L'hidrogen líquid és un combustible prometedor per a una aviació de baixes emissions de carboni, però emmagatzemar-lo a uns 20 K exigeix parets de tanc lleugeres que es mantinguin íntegres a temperatura criogènica. En un material compost reforçat amb fibres, la matriu polimèrica es contrau molt més que les fibres durant el refredament, i aquest desajust genera tensions residuals a l'escala de les fibres que poden nuclear microesquerdes i comprometre la integritat estructural de la paret. Aquesta tesi desenvolupa una metodologia basada en microtomografia computeritzada de raigs X que prediu la resposta termomecànica efectiva d'un compost de fibra curta directament a partir de la seva microestructura mesurada, de manera que es puguin avaluar diferents configuracions de material sense fabricar i assajar una proveta per a cadascuna. El material estudiat és un compost de poliamida 11 reforçat amb fibra curta de basalt, fabricat per fabricació additiva, candidat per al revestiment interior (liner) d'un tanc criogènic de doble paret del projecte OVERLEAF.

Se segmenta un únic escaneig de micro-CT i se n'identifiquen les fibres, amb la qual cosa s'obtenen la longitud, el diàmetre i l'orientació de cada fibra. Les distribucions de probabilitat ajustades a aquestes magnituds alimenten un esquema de Monte Carlo que genera un element de volum representatiu (RVE) a la fracció volumètrica de fibra objectiu, que s'homogeneïtza mitjançant el mètode dels elements finits. En refredar-lo des de 293 K fins a 20 K s'obté el coeficient de dilatació tèrmica direccional, de l'ordre de 6×10^{-5} per kelvin i lleugerament anisòtrop, juntament amb les tensions tèrmiques residuals. El mètode s'implementa com un únic script reutilitzable els paràmetres estadístics i la fracció volumètrica del qual es poden modificar per modelar un altre sistema de fibra curta.

PARAULES CLAU: emmagatzematge d'hidrogen líquid; poliamida 11 reforçada amb fibra de basalt; tomografia computeritzada de raigs X; element de volum representatiu; coeficient de dilatació tèrmica.

Abstract

Liquid hydrogen is a promising fuel for low-carbon aviation, but storing it at about 20 K requires lightweight tank walls that stay intact at cryogenic temperature. In a fibre-reinforced composite the polymer matrix contracts far more than the fibres on cooling, and this mismatch raises residual stresses at the scale of the fibres that can nucleate microcracks and compromise the structural integrity of the wall. This thesis develops a micro-computed-tomography based methodology that predicts the effective thermomechanical response of a short-fibre composite directly from its measured microstructure, so that different material configurations can be screened without manufacturing and testing a specimen for each one. The material studied is a short basalt-fibre-reinforced polyamide 11 composite produced by additive manufacturing, a candidate for the inner liner of a dual-wall cryogenic tank in the OVERLEAF project.

A single micro-CT scan is segmented and its fibres identified, giving the length, diameter and orientation of each fibre. Probability distributions fitted to these quantities feed a Monte Carlo scheme that generates a representative volume element at the target fibre volume fraction, which is homogenised by the finite element method. Cooling it from 293 K to 20 K yields the directional coefficient of thermal expansion, of the order of 6×10^{-5} per kelvin and mildly anisotropic, together with the residual thermal stresses. The method is implemented as a single reusable script whose statistical inputs and volume fraction can be changed to model another short-fibre system.

KEYWORDS: liquid hydrogen storage; basalt-fibre-reinforced polyamide 11; X-ray computed tomography; representative volume element; coefficient of thermal expansion.

1. TABLE OF CONTENTS

1. Introduction 1

1.1 Background and Motivation 1

1.2 The OVERLEAF Project and Industrial Context 3

1.3 Aim and Objectives 5

1.4 Structure of the Report 6

2. STATES of the Art 7

2.1 Liquid Hydrogen Storage and Type IV Tanks 7

2.2 Coefficient of Thermal Expansion 9

2.3 Thermomechanical Stresses 11

2.4 Short Fibre Composites 12

2.5 Representative Volume Elements for Short Fibre Composites 15

2.5.1 Homogenisation and RVE Fundamentals 15

2.5.2 Research Gap: Three-Dimensional, Short-Fibre RVEs 17

2.6 X-ray Computed Tomography of Fibre-Reinforced Composites 18

2.7 Summary and Research Gap 20

3. Methodology 23

3.1 Overview of the pipeline 23

3.2 Micro-CT acquisition and image processing 24

3.2.1 Sample preparation and scanning parameters 24

3.2.2 Analysed region and sub-volume extraction 27

3.2.3 Image segmentation: binarisation in Fiji 33

3.2.4 Validation of the binarisation 37

3.3 Microstructural characterisation 38

3.3.1 Fibre identification and geometric measurement 38

3.3.2 Validation of the fibre extraction 46

3.3.3 Statistical distribution fitting 50

3.3.4 Goodness-of-fit assessment 54
3.4 Representative volume element generation and thermal analysis 56
3.4.1 Monte Carlo generation of the fibre architecture 56
3.4.2 Finite element model 59
4. Result and Discussion 65
4.1 Microstructural characterisation results 65
4.2 Fitted statistical distributions 66
4.3 Homogenised coefficient of thermal expansion 68
4.4 Sensitivity and limitations 69
5. Conclusions and further developments 71
5.1 Main conclusions 71
5.2 Further developments 72

List of Figures

Figure 1.1 Schematic cross-section of a dual-wall cryogenic liquid hydrogen storage tank, showing the outer structural wall, thermal insulation, inner liner and stored liquid hydrogen. The short basalt-fibre PA11 inner liner is the material studied in this thesis. Cross-section not to scale. 4
Figure 1.2 Workflow adopted in this thesis, from micro-CT of the composite to the homogenised thermal response. The first three stages characterise the microstructure; the last three predict the effective properties by homogenisation. 6
Figure 3.1 The CT-to-RVE-to-FEM pipeline as a whole. 24
Figure 3.2 Visual representation of build/print orientations. 25
Figure 3.3 Representation of the μ-CT scan geometry: the XZ-Z coupon of Figure 3.2 mounted between the X-ray source and detector, with the analysis region near mid-length. The arrow marks the printing direction, along which the fibres are laid. Axes are those of the reconstructed volume, with the bar length along y and the fibres along z. 26
Figure 3.4 Analysed region, matrix is the black background and fibres are in grey, in its different views: a) x-direction (yz view), b) z-direction (xy view) and c) y-direction (xz view). 28
Figure 3.5 Selection of regions of interest (ROIs) for microstructural analysis: a) The ImageJ/Fiji ROI Manager listing the ten ROIs defined across the reconstructed volume, each labeled by its slice number and center coordinates and b) the corresponding ROIs (green rectangles) overlaid on a representative cross-sectional slice, showing their size and spatial distribution within the specimen. 30
Figure 3.6 Extraction of a sub-volume in Fiji: a) Selecting the sub-volume region on the y-view of the analysed volume, b) Cropping the selection with Duplicate, over the slice range 100 to 109, c) The cropped sub-volume in the y orientation (195 × 46 px, 682.51 × 161.00 μm), d) Reslicing the crop in Fiji at 3.5 μm spacing (Image>Stacks>Reslice), e) The x orientation obtained by reslicing from the top (195 × 10 px, 682.51 × 35.00 μm) and f) The z orientation obtained by reslicing from the left (46 × 10 px, 161.00 × 35.00 μm). 31
Figure 3.7 Coordinate system and orientation convention for a sub-volume: a) Default three-dimensional (3D) rendering of a sub-volume in Fiji, b) The x, y and z axes of the sub-volume, with the fibres running along z, c) The three orthogonal planes (YZ, XZ and XY planes) of the sub-volume, d) The orientation angles defined relative to the z axis: $\alpha \rightarrow$ Upward/downward tilt (out of plane angle), $\beta \rightarrow$ sideways tilt/rotation (in-plane angle) and e) The origin of the reference coordinate system at (0, 0, 0). The origin

fixes the reference frame only; α and β are computed from each fibre's direction and do not depend on its position..... 33
Figure 3.8 Binarisation of a micro-CT sub-volume in Fiji: a) The greyscale sub-volume before processing, b) Opening the median filter (Process>Filters>Median), c) The median filter set to a radius of one pixel, with live preview, d) Applying the filter to all ten slices of the stack, e) Opening Enhance Contrast (Process, Enhance Contrast), f) Enhance Contrast set to 0.3% saturated pixels, normalised, over all ten slices, g) Opening the threshold tool (Image, Adjust, Threshold), h) The Otsu threshold shown on the stack, dark background, with the selected fibres in red (18.23%), i) Converting the stack to a binary mask by Otsu's method, dark background, with the threshold calculated for all slices and j) The resulting binary sub-volume, fibres in white on a black background. 35
Figure 3.9 Binarisation check on one sub-volume: a) binary mask, b) greyscale slice and c) fibre outlines from the mask overlaid on the greyscale, showing that the binarisation captured the fibres well. 38
Figure 3.10 Fibre volume fraction of the ten sub-volumes obtained from the binarisation, compared with the nominal 20 per cent target. The mean is 18.9 per cent, and all ten values lie close to the target, confirming that the threshold was placed sensibly in each sub-volume..... 38
Figure 3.11 The browser-based fibre-tracking tool used for fibre identification: a) The full interface of the tool, b) Input panel, where the sub-volume is loaded in its three reslice orientations, c) Parameters panel, set to the values used in this fibre identification and d) Run control panel and the note on how the three directions are fused into a single fibre set..... 39
Figure 3.12 Fibre-centre detection by the distance transform, shown for two touching fibres (representative): a) the binary cross-sections, b) the Euclidean distance transform, in which each voxel holds its distance to the nearest background and is largest at the fibre centres, and c) a profile across the two centres, where each fibre appears as a peak and the two are separated at the valley between them. The largest inscribed distance at a centre is the fibre radius and does not change as the fibre tilts. 40
Figure 3.13 The fibre-tracking tool in operation on a sub-volume: a) The three directional stacks loaded into the tool, each as a binary mask with its raw greyscale, b) The parameter values used for the run, c) The fibres reconstructed in three dimensions after fusion, d) Detected fibre cross-sections, marked by circles, on slice 53 of the z-direction stack, e) Direction alignment and export panel: the X and Y detections registered to the Z reference by binary overlap (scores 0.79 and 0.81), and the export options, including

the fused-fibre CSV and f) Summary panel for the sub-volume: the number of fused fibres, their volume fraction, median orientation and median diameter, with the orientation histogram below. 44
Figure 3.14 Example of a fused-fibre CSV exported by the tool for one sub-volume. 46
Figure 3.15 napari overlay of the extracted fibres for one sub-volume: a) The detected fibres, drawn as cylinders, overlaid on the raw greyscale stack; each cylinder sits on a real fibre in the image, b) The same fibre cylinders alone, with the greyscale hidden, showing the recovered population and its orientation, c) The fibre centre-lines and d) The fibre centroids. 49
Figure 3.16 Distribution histograms of length and orientation angles of the fibres: a) Fibre length: measured histogram with the fitted lognormal, gamma and Weibull densities, b) Elevation angle α: measured histogram with the fitted normal, Laplace and generalised generalised normal densities and c) Azimuth angle β: measured histogram with the fitted normal, Laplace and generalised normal densities. 53
Figure 3.17 Fibre diameter: empirical distribution over the nine measured values. 53
Figure 3.18 Quantile-quantile plotting of length and orientation angles of the fibres: a) Q-Q plot for the Weibull fit to the fibre length, b) Q-Q plot for the generalised normal fit to the elevation angle α and c) Q-Q plot for the Laplace fit to the azimuth angle β. 55
Figure 3.19 One realisation of the generated RVE, of size 161.00 × 35.00 × 679.01 μm (one CT sub-volume), at a fibre volume fraction of 20%, showing the basalt fibres within the PA11 matrix and the flat outer faces produced by the trim. 59
Figure 3.20 The two-part primitives created before merging: the matrix box and b) a representative fibre cylinder. 60
Figure 3.21 The mechanical boundary conditions on the RVE, the three boundary conditions named as ROLLER_X0, Y0 and Z0 holding the faces at the origin against motion normal to each, with the three opposite faces left free. 62
Figure 3.22 The RVE meshed with quadratic tetrahedral (C3D10) elements, the mesh conforming across the fibre and matrix. 63
Figure 4.1 Displacement magnitude (U, in mm) over the RVE at the end of the cooldown from 293 K to 20 K, showing the thermal contraction. The fixed faces remain in place and the free faces displace most, reaching a peak of 1.19×10^{-2} mm. Deformation exaggerated 10× for clarity. 69

List of Tables

Table 2.1 Classification of hydrogen storage pressure vessels. 8
Table 2.2 Representative RT properties of common reinforcing fibres and the polyamide 11 matrix.... 14
Table 2.3 Canonical boundary conditions used in the homogenisation of a representative volume element. 16
Table 3.1 Micro-CT acquisition parameters. 26
Table 3.2 Otsu threshold grey percentage [as shown in Figure 3.8 (h)] used for each of the ten sub-volumes. 36
Table 3.3 Parameters used in the fibre-tracking tool. 45
Table 3.4 Binary overlap of the X and Y reslices with the Z reference, for each sub-volume. 46
Table 3.5 Number of fibres detected in each sub-volume..... 50
Table 3.6 Candidate distributions and their probability density functions. Γ denotes the gamma function. 51
Table 3.7 Material Properties. 63
Table 4.1 Descriptive statistics of the measured fibre geometry (n = 307 fibres). 65
Table 4.2 Adopted distribution and fitted parameters for each geometric quantity. 66
Table 4.3 Pearson chi-square goodness-of-fit comparison of the candidate distributions. The degrees of freedom are the number of bins minus one minus the number of fitted parameters. 67
Table 4.4 Empirical distribution of the fibre diameter over its nine measured values. 67
Table 4.5 Directional thermal strain and secant coefficient of thermal expansion over the cooldown from 293 K to 20 K, the coefficient being the secant value referred to the stress-free reference of 293 K. .. 68

Abbreviations

CFRP	Carbon-fibre-reinforced polymer
CTE	Coefficient of thermal expansion
FOV	Field of view
HTML	HyperText Markup Language
KUBC	Kinematic uniform boundary conditions
LH_2	Liquid hydrogen
µCT (micro-CT)	Micro-computed tomography
ROI	Region of interest
RT	Room temperature

Symbols

Latin

E_i	Expected number of fibres in bin i (chi-square test)
m	Number of histogram bins
n	Sample size (number of fibres)
O_i	Observed number of fibres in bin i (chi-square test)
p	Significance (p-value)

Greek

$\bar{\alpha}$	Secant coefficient of thermal expansion
ε	Thermal strain
θ_0	Reference (stress-free) temperature
λ	Scale parameter of the Weibull distribution
μ	Location parameter (mean) of a fitted distribution
χ^2	Pearson chi-square statistic

THIS PAGE WAS INTENTIONALLY LEFT BLANK

1. INTRODUCTION

1.1 Background and Motivation

Reducing greenhouse gas emissions from transport is one of the central objectives of current energy and climate policy, and aviation is among the hardest sectors to decarbonise because almost all of its energy is supplied by liquid hydrocarbon fuel. Hydrogen has emerged as a leading candidate for a low-carbon aviation fuel, since oxidising it in an engine or a fuel cell produces no carbon dioxide at the point of use [1]. It also has the highest energy content per unit mass of any chemical fuel, about 120 MJ/kg, roughly three times that of conventional jet fuel [2]. The obstacle is not producing hydrogen but storing it. At ambient conditions its energy per unit volume is very low, so a usable store must either compress the gas to high pressure or cool it into its liquid state, and for an aircraft, where both mass and volume are limited, on-board storage is widely regarded as the principal barrier to adoption [2], [3].

Liquefying hydrogen raises its volumetric energy density enough to be practical for flight, at the cost of holding it at about 20 K. Liquid hydrogen carries around 2.8 times the energy per unit mass of conventional jet fuel, although it still occupies several times the volume for the same energy, so the tank and its insulation dominate the design of a liquid hydrogen aircraft [3]. The choice of tank material is therefore decisive. Metallic cryogenic tanks are heavy, and their mass penalty erodes the payload and range that make hydrogen attractive in the first place [4]. Carbon fibre-reinforced polymer composites (CFRP) offer far lower density at high specific strength and stiffness, and linerless composite tanks have been shown to reduce structural mass by roughly 20 to 40 per cent relative to metal [4], [5]. For this reason, the field has moved steadily towards composite cryogenic tanks, and the demands placed on the wall material are severe: high strength and stiffness, high fracture toughness, low density and a low coefficient of thermal expansion, each retained down to cryogenic temperature [1].

The materials problem at the centre of this thesis follows from that final requirement. A fibre-reinforced composite is a two-phase material whose fibre and matrix contract by different amounts as the temperature falls. The coefficient of thermal expansion of a polymer matrix is typically about an order of magnitude larger than that of the reinforcing fibre, so cooling from the processing temperature to 20 K forces a large strain incompatibility between the two phases [6]. This mismatch raises thermal residual stresses at the scale of the fibres, and where those stresses exceed the local strength of the cooled and

embrittled matrix they nucleate microcracks [6], [7]. Left unchecked, microcracks can grow and coalesce into macroscopic cracks that compromise the structural integrity of the tank wall [7]. Anticipating, and ultimately preventing, this progression from microscale residual stress to global cracking is the reason the thermomechanical response of the composite has to be understood at the scale of the individual fibres.

The material studied here is a short basalt-fibre-reinforced polyamide 11 (PA11) composite, shaped by additive manufacturing. PA11 is a semi-crystalline thermoplastic produced from castor oil rather than from petroleum, which gives it a favourable sustainability profile, and it combines good chemical resistance with unusually high toughness at low temperature [8]. A thermoplastic matrix also offers weldability, repairability and recyclability that thermoset composites do not, and it can be shaped by out-of-autoclave routes, including the extrusion-based printing used to build the specimens studied here [9], [10]. Basalt fibre is drawn from molten volcanic rock and gives mechanical performance comparable to glass fibre, with better thermal and chemical durability, at a fraction of the cost of carbon fibre and with a lower environmental burden [11]. It remains usable across a wide temperature range that extends well below zero, and it has been identified as a cost-effective reinforcement for hydrogen pressure vessels, in which carbon fibre is otherwise the dominant cost driver [12]. A short basalt fibre in a printable PA11 matrix therefore offers a recyclable, lower-cost composite that can be formed into complex tank geometries, and such short basalt-fibre PA11 systems have already been demonstrated by melt processing [13].

Manufacturing flexibility comes at a price: the internal architecture of an additively manufactured short-fibre composite is not uniform. As the fibre-filled polymer is deposited along the print path, the fibres align preferentially with the direction of deposition, and the finished part contains distributions of fibre length, diameter and orientation, together with a fibre volume fraction that varies from place to place [13], [14]. Because the fibre scale governs the stiffness, strength and thermal expansion of the composite, these microstructural features control the thermomechanical response directly, and a model that assumes a regular or perfectly aligned arrangement cannot represent the real behaviour [14], [15]. The as-manufactured microstructure must therefore be measured before that behaviour can be predicted with any confidence.

X-ray computed tomography makes this measurement possible. It images the interior of the composite without destroying it and resolves the individual fibres in three dimensions, so their lengths, diameters, orientations and volume fraction, together with the matrix and any voids or manufacturing defects, can

be extracted directly from the reconstructed volume [15]. Those statistics can then be used to build a representative volume element, a small region of material whose fibre population reproduces the measured architecture, and finite element homogenisation of that element returns the effective properties of the composite, among them the coefficient of thermal expansion and the internal stresses that develop on cooling [16]. Predicting properties in this way, from a microstructurally faithful model rather than from a physical coupon, is the essence of virtual testing, and it is attractive here for a practical reason: characterising a composite at cryogenic temperature is slow and costly, so a validated model that captures the real microstructure allows different material configurations, such as different fibre volume fractions, to be screened without manufacturing and testing a specimen for each one [17]. Building such a model from tomographic data, and demonstrating it on a short basalt-fibre PA11 composite, is the approach taken in this work.

1.2 The OVERLEAF Project and Industrial Context

This thesis was carried out within the OVERLEAF project (Novel low-pressure cryogenic liquid hydrogen storage for aviation), a research and innovation action funded by the European Union under grant agreement number 101056818 [18]. The project addresses the barrier described above directly. Its aim is to develop a low-pressure liquid hydrogen storage system for aircraft, so that hydrogen propulsion can contribute to the decarbonisation targets set for the aviation sector [18]. The concept is a dual-wall tank that holds liquid hydrogen at around 23 K and a maximum pressure of 6 bar, storing of the order of 105 kg of hydrogen with a low boil-off rate, and it is designed to reach a gravimetric index near 40 per cent together with a substantial reduction in overall system weight compared with the current state of the art [18].

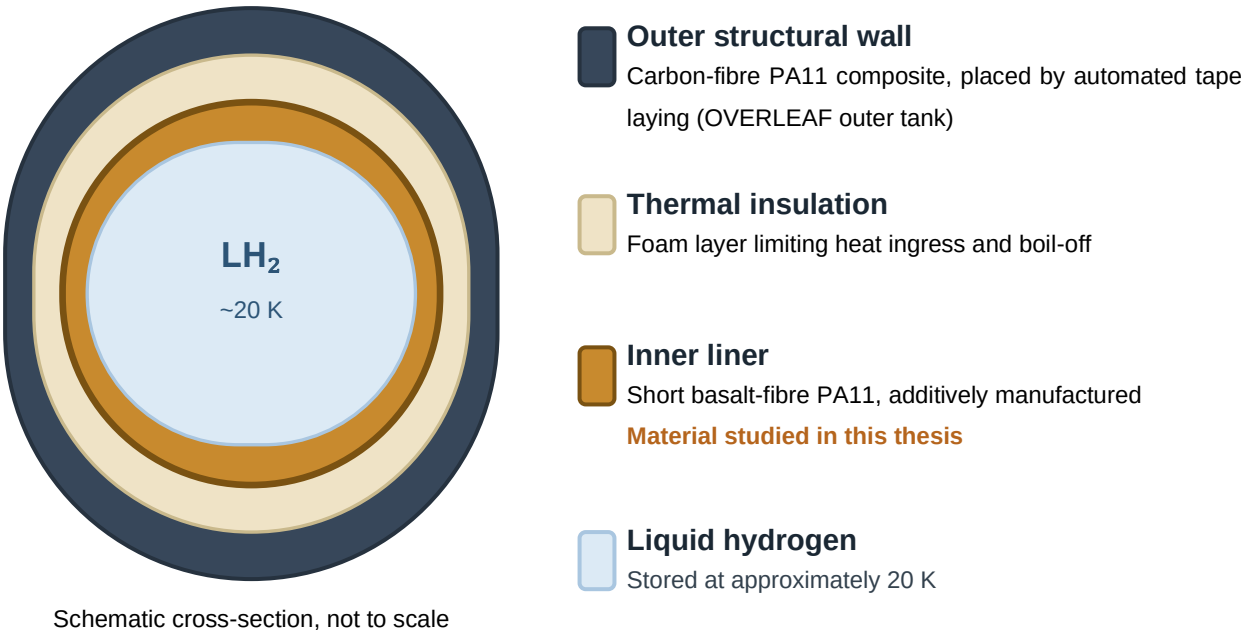


Figure 1.1 Schematic cross-section of a dual-wall cryogenic liquid hydrogen storage tank, showing the outer structural wall, thermal insulation, inner liner and stored liquid hydrogen. The short basalt-fibre PA11 inner liner is the material studied in this thesis. Cross-section not to scale.

Several material and manufacturing innovations are combined in the design, illustrated schematically in Figure 1.1. The outer tank is a linerless thermoplastic composite structure produced by automated tape laying from carbon-fibre-reinforced polyamide 11 tape, the matrix supplied as Rilsan grade by Arkema and chosen because it is bio-based and recyclable [18]. The inner tank is produced by additive manufacturing, thermal insulation is provided by advanced foams that limit heat ingress and boil-off, and fibre-optic sensors based on metal-hydride thin films detect any hydrogen leak [18]. The work is delivered by a consortium of industrial and academic partners coordinated by Aciturri, within which the AMADE group at the University of Girona is responsible for numerical simulation and for the mechanical testing of composite coupons [18].

The contribution of this thesis sits within that simulation and characterisation remit. Whereas the outer tank uses a continuous carbon-fibre tape, this thesis investigates a short basalt-fibre-reinforced PA11 composite, produced by additive manufacturing in the same spirit as the inner tank, as a candidate material for the inner liner. Basalt is considered in place of carbon because, as set out in Section 1.1, it offers a lower-cost and more sustainable reinforcement while remaining serviceable at low temperature. The thesis develops the methodology needed to characterise the microstructure of this composite and to predict its thermomechanical properties from that microstructure. By establishing a repeatable route from a tomographic scan to a homogenised property, the work supports the project's wider need for validated

models of composite behaviour at cryogenic temperature, and it provides a tool that can be reapplied to other short-fibre systems and other fibre contents as the material selection develops.

1.3 Aim and Objectives

The aim of this thesis is to develop a micro-computed-tomography based computational methodology that predicts the effective thermomechanical properties of a short-fibre-reinforced polymer composite directly from its measured microstructure, so that different material configurations, such as different fibre volume fractions, can be evaluated without manufacturing and physically testing a specimen for each one. The methodology is applied to a short basalt-fibre-reinforced polyamide 11 composite, a candidate material for the inner liner of a cryogenic liquid hydrogen storage tank, and is used to predict the coefficient of thermal expansion and the residual stresses that develop when the material is cooled from room temperature (RT) to the storage temperature.

The overall workflow, from the tomographic scan through to the homogenised properties, is shown in Figure 1.2. The aim is met through the following objectives:

1. Acquire and reconstruct a micro-computed-tomography volume of the additively manufactured short basalt-fibre PA11 composite, and extract a set of representative sub-volumes for quantitative analysis.
2. Segment the fibres from the polyamide 11 matrix, validate the binarisation through the fibre volume fraction, and measure the length, diameter, and elevation and azimuth angles of each fibre.
3. Represent the measured geometry by fitting candidate probability distributions to the fibre length and the two orientation angles, selecting the most suitable for each by a goodness-of-fit test, and describing the resolution-limited diameter by its empirical distribution.
4. Generate a representative volume element that reproduces the fitted distributions at the target fibre volume fraction, implemented as a single self-contained script whose inputs, the distribution parameters and the volume fraction, can be changed to model a different configuration or material.
5. Predict the effective coefficient of thermal expansion and the residual thermal stresses of the composite by finite element homogenisation of the generated volume, cooling it from RT (293 K) to the liquid hydrogen storage temperature (20 K).

6. Discuss the predictions in the light of the constituent properties, and identify the principal limitations and the priorities for developing the methodology into a fully validated predictive tool.

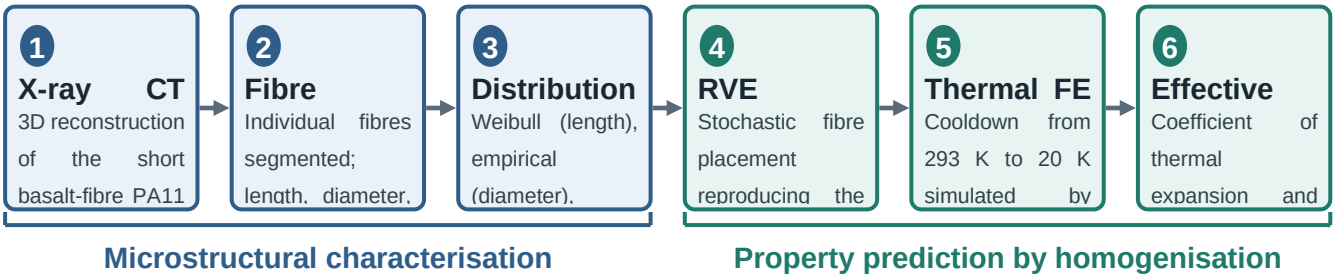


Figure 1.2 Workflow adopted in this thesis, from micro-CT of the composite to the homogenised thermal response. The first three stages characterise the microstructure; the last three predict the effective properties by homogenisation.

1.4 Structure of the Report

The remainder of this report is organised as follows. Chapter 2 reviews the state of the art, covering liquid hydrogen storage and composite tank concepts, the thermomechanical behaviour of short-fibre composites at low temperature, the coefficient of thermal expansion and the residual stresses that arise from thermal contraction mismatch, X-ray computed tomography of fibre-reinforced materials, and the representative volume element approach to homogenisation. Chapter 3 sets out the methodology in four stages: micro-CT acquisition and image segmentation, identification and measurement of the individual fibres, statistical fitting of the fibre geometry, and generation and thermal analysis of the representative volume element. Chapter 4 presents and discusses the results, comprising the measured microstructure, the fitted distributions, the generated volume element and its mesh, and the effective coefficient of thermal expansion and residual stresses obtained by cooling it to the storage temperature, and it closes with the sensitivity of these results and the limitations of the model. Chapter 5 draws the conclusions and sets out recommendations for future work.

2. STATES OF THE ART

This chapter reviews the body of work on which the present study is built. It begins with the storage of liquid hydrogen and the composite pressure vessels developed for it, and with the reasons that a polymer-lined tank must retain its integrity at cryogenic temperature (Section 2.1). It then examines the coefficient of thermal expansion, the material property that governs the response of a two-phase composite to cooling (Section 2.2), and the thermomechanical stresses that the mismatch in expansion between fibre and matrix produces (Section 2.3). The material system of interest, a short basalt-fibre-reinforced polyamide 11 composite, is placed in the context of short-fibre thermoplastic composites in Section 2.4. Section 2.5 reviews homogenisation and the representative volume element, the framework used here to predict effective properties, and identifies the gap that this thesis addresses. Section 2.6 surveys X-ray computed tomography as the means of measuring the real fibre architecture, and Section 2.7 draws the review together and states the research gap.

2.1 Liquid Hydrogen Storage and Type IV Tanks

Among the routes to storing hydrogen on board an aircraft, liquefaction offers the highest volumetric energy density, at the cost of holding the fuel at its normal boiling point of about 20 K [1]. Liquid hydrogen is considerably denser than the compressed gas: at its boiling point it reaches a density of the order of 71 kg/m³, roughly 1.8 times that of hydrogen compressed to 700 bar at ambient temperature, which is the property that makes it attractive where volume is constrained [19]. The penalty is the need for continuous refrigeration and thermal insulation, since heat ingress causes boil-off that must be vented or otherwise managed [19]. The tank and its insulation therefore dominate the design of a liquid hydrogen system, and the choice of wall material is decisive [1].

Pressure vessels for hydrogen are conventionally grouped into five types according to their construction (Table 2.1) [20], [21]. Type I is an all-metal cylinder; Type II a metallic liner hoop-wrapped with composite; Type III a metallic liner fully overwrapped with composite; and Type IV a polymer liner fully overwrapped with a fibre-reinforced composite [20]. In a Type IV vessel, the polymer liner acts as a gas barrier while the composite overwrap carries the structural load, an arrangement that reduces weight and cost relative to the metal-lined types and has made Type IV the primary choice for on-board compressed hydrogen [19]. A fifth, linerless concept (Type V), in which the composite provides both the barrier and the structure, remains under development and is not yet commercially mature [21].

Table 2.1 Classification of hydrogen storage pressure vessels.

Type	Construction	Liner	Principal characteristics
I	All-metal cylinder	Metal (is the structure)	Heaviest; lowest cost
II	Metal liner, hoop-wrapped with composite	Metal	Partial composite reinforcement
III	Metal liner, fully overwrapped with composite	Metal	Composite carries most of the load
IV	Polymer liner, fully overwrapped with composite	Polymer (e.g. HDPE, polyamide)	Lightweight; primary choice for on-board hydrogen
V	Linerless composite	None	Composite is barrier and structure; under development

Compiled from [19], [20], [21].

In a Type IV vessel, the liner is typically a thermoplastic such as high-density polyethylene or a polyamide, selected for its gas-barrier performance, and the overwrap is a carbon- or glass-fibre-reinforced polymer applied by filament winding [19], [20]. Because filament-wound vessels are prone to failure in their dome regions, the geometry of the dome governs the structural design [22]. Carbon fibre dominates the cost of such vessels, which has motivated interest in lower-cost reinforcements [19]. Standards place limits on the permissible steady-state hydrogen permeability of the liner, and much of the Type IV literature is concerned with characterising and modelling permeation through the polymer [20].

The great majority of this work addresses compressed hydrogen at ambient temperature, where the principal liner concern is permeation [20]. Cryogenic storage introduces a different and more severe demand. A tank that holds liquid hydrogen must retain the integrity of its wall through cooling to about 20 K and through repeated thermal cycling, conditions under which the mismatch in thermal contraction between the fibres and the polymer matrix generates internal stresses at the scale of the microstructure [6], [7]. Where these stresses exceed the strength of the cooled and embrittled matrix they nucleate microcracks, and unchecked microcracking can coalesce into macroscopic cracks that compromise the load-bearing capacity of the wall [7]. The structural consequences of this progression, rather than permeation alone, are the motivation for understanding the thermomechanical response of the composite at low temperature. The complexity of the failure modes of composite overwrapped vessels, and the need to detect damage before it becomes critical, are recognised challenges that have prompted the development of structural health monitoring for these structures [23].

Managing heat ingress is as important to a liquid hydrogen tank as the structural design of its wall. Because the fuel is held only a little above absolute zero, even a small heat leak drives boil-off, and the tank must therefore combine a structural wall with an effective thermal insulation system, whether a vacuum, a foam, or a multi-layer arrangement, chosen to limit the heat flux within an acceptable mass [3], [19]. The dual-wall configuration adopted in the present project separates these two functions, with an outer structural wall and an inner containment wall between which the insulation is placed [18]. The material studied in this thesis belongs to the inner wall, where it must remain intact at the storage temperature while the insulation controls the thermal environment around it.

The storage system considered in this work departs from the automotive Type IV vessel in operating at low pressure and very low temperature. The OVERLEAF concept is a dual-wall tank that holds liquid hydrogen at around 23 K and a maximum pressure of 6 bar, in which a linerless carbon-fibre-reinforced polyamide 11 outer structure provides the load path and an additively manufactured inner tank, the subject of this thesis when reinforced with short basalt fibre, serves as the liner [18]. Composite construction is pursued because linerless composite tanks can reduce structural mass by a substantial margin relative to metal, preserving the payload and range advantages that motivate hydrogen propulsion in the first place [1], [5]. The remainder of this chapter concerns the material behaviour that determines whether such a composite wall can meet these demands, beginning with the property that governs its response to cooling.

2.2 Coefficient of Thermal Expansion

The coefficient of thermal expansion (CTE) quantifies the change in dimension of a material with temperature. The linear coefficient is defined as $\alpha = (1/L)\,(dL/dT)$, where L is a characteristic length and T the temperature, so that the strain accompanying a change in temperature is the integral of α over that interval. A distinction is drawn between the tangent coefficient, the local slope at a given temperature, and the secant coefficient, the average value between a reference temperature and the temperature of interest; the two differ when α varies with temperature, as it does over a wide range. For most solids the coefficient is not constant but falls as the temperature decreases, approaching very small values at cryogenic temperature, so that the contraction accumulated on cooling is smaller than a RT coefficient alone would suggest [6].

In a fibre-reinforced composite the coefficient of the two constituents differs markedly. The polymer matrix typically has a coefficient about an order of magnitude larger than that of the reinforcing fibre, so that

cooling from the processing temperature to the service temperature forces the matrix to contract far more than the fibres it surrounds [6]. For the system studied here the disparity is pronounced: basalt fibre has an axial coefficient of the order of 5 to 6 × 10^{-6} K^{-1}, whereas polyamide 11 contracts at around 100 to 120 × 10^{-6} K^{-1} at RT. The constrained contraction of the matrix against the stiffer fibres is the origin of the thermal residual stresses examined in Section 2.3, and the effective coefficient of the composite, together with its anisotropy, is therefore a property of first importance for a cryogenic tank wall.

The effective coefficient of a composite has long been predicted from the properties and arrangement of its constituents. The simplest estimates are variants of the rule of mixtures, but these neglect the mechanical interaction between the phases that constrains their free expansion. Schapery derived upper and lower bounds, and practical expressions for the longitudinal and transverse coefficients, from energy principles, accounting for this interaction [24]. Comparative studies of unidirectional composites have found that the Schapery model represents the longitudinal coefficient well, while models such as that of Chamis better capture the transverse coefficient, and that both agree reasonably with experiment and with finite element predictions [25].

A more general treatment of the interaction between phases is provided by mean-field homogenisation. The Mori-Tanaka method [26], which builds on Eshelby's solution for the stress in an ellipsoidal inclusion embedded in an infinite matrix [27], estimates the effective thermoelastic properties of a composite from the constituent properties, the inclusion shape and the volume fraction, and has been applied to the effective coefficient of fibre- and nanotube-reinforced composites with good agreement against measurement [28]. These analytical methods are efficient and give useful insight, but they represent the microstructure only through averaged quantities and idealised inclusion shapes, and cannot capture the full distribution of fibre length and orientation present in a real short-fibre composite.

Where the geometry matters, the effective coefficient is instead computed by finite element homogenisation of a representative volume element, the approach adopted in this thesis and reviewed in Section 2.5. Such models apply a uniform temperature change to a volume containing an explicit fibre arrangement and recover the effective coefficient from the resulting deformation. This route has been used to predict, and even to tune, the effective coefficient of composites containing randomly distributed fibres, with the fibre volume fraction and orientation as the controlling variables and periodic boundary conditions applied to the volume [29]. It has the advantage of representing the microstructure directly, at the cost of greater computational effort than the analytical estimates.

The effective coefficient is also sensitive to the defects that a real material contains. Finite element studies of composites with explicit defects have shown that matrix cracks and porosity alter the coefficient in opposite senses, cracks tending to raise it and voids to lower it, so that a model aiming at quantitative accuracy must eventually account for them [30]. Experimentally, the coefficient is measured by dilatometry or thermomechanical analysis, and increasingly by full-field optical methods, although such measurements are demanding at cryogenic temperature, which is part of the motivation for the predictive approach taken here. The stresses that the mismatch in coefficient produces are considered next.

2.3 Thermomechanical Stresses

When a composite is cooled, the difference in thermal contraction between its constituents cannot be accommodated freely, because the phases are bonded across their interface. The matrix, which would contract more if unconstrained, is held back by the stiffer, lower-expansion fibres, and the fibres are correspondingly compressed; the result is a field of residual stress that is locked into the material at the scale of the individual fibres [6]. The magnitude of this stress grows with the temperature interval, and for a tank cooled from a processing or RT state to the storage temperature of about 20 K the interval is large, of the order of 270 K, so that the residual stresses can be substantial even though the material is nominally unloaded.

These residual stresses are consequential because they can initiate damage. Where the local stress exceeds the strength of the matrix, which is itself reduced and embrittled at low temperature, microcracks nucleate, typically as transverse cracks within the matrix and as debonding at the fibre-matrix interface [6], [7]. Individually such microcracks are small, but under continued or cyclic thermal loading they can grow and link together, and the coalescence of microcracks into macroscopic cracks is the mechanism by which the structural integrity of a cryogenic composite wall is ultimately compromised [7]. Direct evidence for this progression has been obtained by in-situ X-ray computed tomography of carbon-fibre laminates cooled to cryogenic temperature, which records a pronounced increase in the volume of transverse matrix cracks and delaminations and attributes it to the brittle transition of the matrix and to the thermal stresses that develop on cooling [31]. The severity of the cracking rises as the temperature falls: in-situ observation of cross-ply laminates loaded at 30 K, close to the storage temperature of interest here, has shown that the matrix crack density is higher and the strain at which cracking begins lower than at RT, an effect traced by finite element analysis to the thermal strains set up in the transverse plies [32].

It is this progression, from microscale residual stress to microcracking to macroscopic cracking, that a predictive model of the thermomechanical response seeks to anticipate.

The susceptibility of a composite to this damage is aggravated by the behaviour of the polymer matrix at cryogenic temperature, where it becomes stiffer and less able to yield, and so less tolerant of the stress concentrations around the fibres. Efforts to improve the cryogenic performance of composites have accordingly focused on toughening the matrix, for instance by the addition of low-expansion nanoparticles that reduce the local mismatch and impede crack growth [7]. The resistance of additively manufactured fibre composites to microcracking under cryogenic conditions has been studied specifically, reflecting the relevance of the printing route used for the material in this thesis [9].

Because the damage of interest begins at the scale of the matrix and the fibres, its characterisation requires methods that resolve individual cracks within the bulk of the material. X-ray computed tomography, reviewed in Section 2.6, has been used to detect and quantify transverse matrix cracking in laminates intended for liquid hydrogen tanks, where the cracking is driven precisely by the mismatch in CTE between fibre and matrix under thermal cycling; automated image analysis of the reconstructed volumes allows the crack density to be measured and its progression tracked [33]. The ability to measure crack density in this way provides the experimental counterpart to the stresses that a homogenisation model predicts.

The stresses that develop, and the damage they cause, depend not only on the average microstructure but on its local detail and on the defects it contains. Micromechanical analyses that incorporate material variability and microvoids have shown that these features influence the predicted stresses and the onset of failure, and that a deterministic model based on an idealised, defect-free microstructure may misrepresent the real response [34]. Modelling the cooldown itself has proved informative: multiscale simulations of a stress-free cooldown to the liquid hydrogen temperature have been used to predict the onset of matrix microcracking in thermoplastic-matrix composite tanks and to compare candidate matrices and layups, which underlines the value of a micromechanical treatment of the cooldown of the kind developed in this thesis [35]. These observations motivate a modelling approach that represents the actual fibre architecture and, in due course, its defects, rather than an idealised unit cell. The representative volume element provides the framework for such an approach, and its foundations are reviewed in Section 2.5, after the material system itself has been introduced.

2.4 Short Fibre Composites

The matrix of the composite studied here is a thermoplastic, chosen in preference to the thermosetting resins that have traditionally dominated structural composites. A thermoplastic matrix can be melted and reshaped, which confers weldability, repairability and recyclability, and it can be processed by out-of-autoclave routes, including the extrusion-based additive manufacturing used to build the specimens of this work [9], [10]. These attributes are attractive for a hydrogen tank, both for manufacturability and for end-of-life recycling, and they align with the sustainability objectives of the wider project [18].

Polyamide 11 is a semi-crystalline thermoplastic distinguished by its origin: it is produced from castor oil rather than from petroleum, giving it a favourable sustainability profile relative to conventional polyamides [8]. It combines good chemical resistance with an unusually high toughness that is retained at low temperature, which is the property most relevant to cryogenic service [8]. Short basalt-fibre-reinforced polyamide 11 has been produced by melt extrusion and its processing and mechanical properties characterised, establishing it as a viable biocomposite [13], and its recyclability when reinforced with basalt fibre has also been demonstrated [10]. Work on the closely related polyamide 6,6 system reinforced with short basalt fibre, produced by injection moulding, has shown that the fibre length and content are the primary factors controlling its stiffness and strength, and that its performance approaches that of the equivalent glass-fibre composite [36].

Basalt fibre is drawn from molten volcanic rock and offers mechanical performance comparable to that of glass fibre, with an elastic modulus of the order of 89 GPa, together with superior thermal and chemical durability [11], [12]. As a reinforcement it is more ductile and more thermally resistant than carbon fibre, and considerably cheaper, which has prompted its study as a partial or complete replacement for carbon in structural composites [12], [37]. Its cost lies between that of glass and carbon fibre, and its environmental burden is lower than that of carbon, which has led to its consideration as a cost-effective reinforcement for applications, including hydrogen pressure vessels, in which carbon fibre would otherwise be the dominant cost [12]. It remains serviceable across a wide temperature range extending well below zero, which is a prerequisite for the cryogenic application considered here [11]. Table 2.2 summarises representative RT properties of the three common reinforcing fibres alongside the polyamide 11 matrix, illustrating the position of basalt between glass and carbon and the large disparity in thermal expansion between fibre and matrix that underlies the residual stresses of Section 2.3.

Table 2.2 Representative RT properties of common reinforcing fibres and the polyamide 11 matrix.

Material	E (GPa)	Density (g/cm³)	Axial CTE (10^{-6} K^{-1})	Relative cost
Basalt fibre	≈ 89	≈ 2.65	≈ 5 to 8	Low to moderate
E-glass fibre	≈ 73	≈ 2.58	≈ 5	Low
Carbon fibre (PAN, standard)	≈ 230	≈ 1.78	≈ −0.5 (axial)	High
Polyamide 11 (matrix)	≈ 1.3	≈ 1.04	≈ 100 to 120	–

Indicative values compiled from [11], [12], [37] *and the constituent data adopted in this thesis (Chapter 3). Carbon fibre has a slightly negative axial coefficient.*

The composite of this work is reinforced with short fibres rather than continuous ones. Short-fibre reinforcement permits shaping by injection moulding and by extrusion-based printing, and so the fabrication of complex geometries, but it introduces a dependence of the properties on the fibre architecture that continuous, aligned reinforcement does not. During compounding and moulding the fibres are broken, producing a distribution of fibre lengths, and they are reoriented by the flow, producing a distribution of orientations [38]. The mechanical properties of the resulting composite, its stiffness, strength and toughness, depend critically on these fibre length and orientation distributions [38], [39]. In basalt-fibre thermoplastics specifically, the fibre orientation induced during processing has been shown to govern the transfer of stress from the matrix to the fibres, and hence the stiffness of the moulded part [40].

Two features of the architecture are particularly influential. The transfer of load from matrix to fibre requires a minimum embedded length, the critical fibre length, below which a fibre cannot be stressed to its full capacity; the strength of a short-fibre composite therefore depends on the fibre length relative to this critical value, and on the quality of the fibre-matrix interface [39], [41]. The orientation distribution determines the degree of anisotropy, since fibres aligned with a loading or cooling direction reinforce and constrain the matrix along it more than misaligned fibres do. In an additively manufactured part these distributions are set by the deposition process: the fibres align preferentially along the print path, so that the finished material is strongly anisotropic and its fibre volume fraction varies from place to place [14].

Because the fibre-scale architecture governs the stiffness, strength and thermal expansion of the composite, a model that assumes a regular or perfectly aligned arrangement cannot represent the real behaviour, and the as-manufactured distributions of fibre length, diameter and orientation must be measured before the thermomechanical response can be predicted [14], [15]. The measurement of this

architecture is the subject of Section 2.6, and its use in a predictive model is the subject of Section 2.5, to which the discussion now turns.

2.5 Representative Volume Elements for Short Fibre Composites

2.5.1 Homogenisation and RVE Fundamentals

The prediction of the effective properties of a composite from those of its constituents is the object of homogenisation, which connects the behaviour of the material at the scale of the microstructure to its behaviour as a continuum at the scale of the structure. The strategy underlies the concept of virtual testing, in which the response of a material is obtained from a microstructurally faithful model rather than from a physical coupon, allowing different configurations to be screened by computation [17]. Its central device is the representative volume element.

A representative volume element is a sample of the microstructure that is at once large enough to be statistically representative of the material, containing a sufficient number of heterogeneities that its effective response does not depend on the boundary conditions applied to it, and small enough to be treated as a material point of the continuum [42]. The requirement that the response be independent of the boundary conditions is the operational definition proposed by Hill, and it is met exactly only in the limit of a large volume; for finite volumes the computed properties are apparent rather than effective, and depend on the size of the volume and on the conditions imposed on its boundary [42].

Two broad families of homogenisation method exist. The analytical, mean-field methods discussed in Section 2.2, among them the Eshelby-based Mori-Tanaka scheme [26], [27], estimate effective properties from averaged fields and idealised inclusion geometries. The computational methods, by contrast, solve the boundary-value problem on an explicit finite element model of the microstructure and average the resulting fields, so that an arbitrary and realistic arrangement of fibres can be represented [29]. The computational route is the more demanding but the more faithful, and it is the one adopted in this thesis.

The properties computed from a finite volume depend on the conditions imposed on its boundary. Three canonical choices are used (Table 2.3): kinematic uniform (Dirichlet) conditions, which prescribe displacements on the boundary; static uniform (Neumann) conditions, which prescribe tractions; and periodic conditions, which require the deformation of opposite faces to be compatible [43], [44]. The uniform displacement and uniform traction conditions bound the true effective property from above and below respectively, and the two bounds converge as the volume approaches the representative size [43]. Periodic boundary conditions generally give the most accurate estimate for a given volume, because they

suppress the artificial boundary layers that the uniform conditions introduce, and they converge fastest with increasing size [43]. For this reason, periodic conditions are regarded as the rigorous choice for homogenisation, although their application requires a mesh whose opposite faces match, or a large set of constraint equations.

Table 2.3 Canonical boundary conditions used in the homogenisation of a representative volume element.

Boundary condition	Prescribed on the boundary	Effect on the apparent property
Kinematic uniform (Dirichlet, KUBC)	Uniform displacement	Over-stiff; provides an upper bound
Static uniform (Neumann, SUBC)	Uniform traction	Over-compliant; provides a lower bound
Periodic (PBC)	Compatible deformation of opposite faces	Most accurate for a given size; fastest convergence

After [42], [43], [44].

Underlying the homogenisation of a representative volume element are two assumptions. The first is the separation of scales, which requires the microstructural features to be much smaller than the volume element, and the volume element in turn much smaller than the structure, so that the two scales can be treated independently. The second is the equivalence of energy between the scales, the condition that the work done by the macroscopic stress on the macroscopic strain equals the average of the microscopic work over the volume. This energy equivalence, known as the Hill-Mandel condition, is what allows an effective constitutive response to be defined for the volume, and each of the boundary conditions in Table 2.3 is admissible precisely because it satisfies it [42], [43].

Determining the size of volume that is genuinely representative is itself a subject of study. A quantitative approach generates an ensemble of realisations of the microstructure at a given volume and examines the mean and the scatter of the computed property, taking the volume to be representative when the scatter is acceptably small; equivalently, a set of smaller volumes may be used in place of a single large one, provided their average converges [45]. To obtain the full effective stiffness tensor, six independent load cases are applied, one for each component of macroscopic strain, while a single uniform temperature change suffices to obtain the effective coefficient of thermal expansion, which is the quantity of primary interest here.

In the present work the volume is generated to be periodic in its geometry, but the mechanical boundary conditions applied for the thermal analysis are a symmetric roller arrangement, a relaxation of strictly periodic conditions adopted because the free tetrahedral mesh used does not produce the matching

opposite faces those periodic conditions require. This choice, and its implications, are discussed with the methodology in Chapter 3. The more fundamental question for the present review is whether the microstructure represented in such a volume corresponds to that of a real short-fibre composite, which is the subject of the following section.

2.5.2 Research Gap: Three-Dimensional, Short-Fibre RVEs

Much of the established work on representative volume elements concerns continuous, unidirectional composites, or short-fibre composites represented by idealised arrangements: a single fibre in a unit cell, perfectly aligned fibres, or fibres confined to a plane. Such models are tractable and have yielded valuable understanding, but they do not capture the three-dimensional distribution of fibre length and orientation that a real, processed short-fibre composite possesses. The influence of this architecture is not incidental; systematic studies have shown that the fibre packing, the fibre geometry and, above all, the distributions of fibre length and orientation are each essential to a faithful prediction of the effective properties, and that neglecting them changes the result appreciably [46].

Constructing a volume that reproduces a realistic three-dimensional short-fibre architecture is not straightforward. The fibres must be placed into the volume without overlapping, at the target volume fraction, and with lengths and orientations drawn from the measured distributions. Sequential placement schemes, in which fibres are added one at a time subject to a non-overlap condition, are commonly used, but the attainable volume fraction is limited by geometric jamming, which becomes more severe as the fibres become longer or more randomly oriented. Approaches that address these difficulties, generating discrete fibre length and orientation distributions within a representative volume, have been developed for short-fibre thermoplastics [46], and algorithms that grow randomly oriented fibres under explicit control of their in-plane and out-of-plane angles, and then homogenise the volume under periodic boundary conditions to obtain the effective coefficient of thermal expansion, have been demonstrated [29].

The statistical description of fibre orientation is commonly formalised through the orientation tensor introduced by Advani and Tucker, which compactly represents an orientation distribution and is widely used to transfer measured orientation information into a model [47]. In the present work the orientation is described instead by fitting probability distributions to two orientation angles measured for every fibre, a choice suited to the strongly aligned population produced by printing, as set out in Chapter 3.

A further limitation of many representative volume models is that they represent an idealised, defect-free and statistically averaged microstructure. Analyses that incorporate the variability of the material and the presence of microvoids have shown that these features affect the predicted response and should not be neglected in a quantitative model [34]. A related distinction is between volumes generated synthetically, from statistical descriptors, and volumes derived directly from an image of the real material. Most representative volume elements are synthetic; image-based volumes, built from the actual microstructure recorded by tomography, are less common, particularly for short-fibre composites and particularly for the prediction of thermal properties.

Bringing these threads together reveals the gap that the present work addresses. The homogenisation of representative volume elements is a mature technique, and X-ray computed tomography is an established means of characterising fibre architecture, but the two have not been combined into a single, repeatable methodology that proceeds from the direct tomographic measurement of a short-fibre composite, through the statistical description of its measured fibre length, diameter and orientation, to the generation of a three-dimensional representative volume element that reproduces those statistics, and finally to the finite element homogenisation of that volume to predict its effective coefficient of thermal expansion and the residual stresses developed on cooling to cryogenic temperature. No such end-to-end pipeline has been reported for a short basalt-fibre-reinforced polyamide 11 composite intended for liquid hydrogen storage. The development and demonstration of this methodology is the contribution of the present thesis. Its first stage, the measurement of the fibre architecture by tomography, is reviewed in the following section.

2.6 X-ray Computed Tomography of Fibre-Reinforced Composites

X-ray computed tomography reconstructs a three-dimensional map of a specimen's internal structure from a series of radiographic projections taken at many angles as the specimen is rotated. In a laboratory micro-focus system, the specimen is placed between an X-ray source and a detector, and the geometric magnification set by their relative positions determines the effective voxel size of the reconstruction, which for the imaging of individual fibres must be of the order of a few micrometres [48]. Because the method is non-destructive, it resolves the internal architecture of a composite without sectioning it, and it has become a principal tool for the three-dimensional characterisation of fibre-reinforced materials [48].

The path from a set of projections to a quantitative measurement passes through several stages, each of which can affect the result. The projections are first reconstructed into a volume, commonly by filtered back-projection, a step sensitive to artefacts such as beam hardening and ring artefacts that must be

corrected if the grey-scale values are to be interpreted reliably [48]. The reconstructed volume is then segmented to separate fibre from matrix and void, and only after this binarisation can the fibres be identified and their geometry measured. Because the segmentation threshold controls the apparent fibre volume fraction, it is usual to validate the binarisation against an independent estimate of that fraction, a check adopted in the present work and described in Chapter 3.

From the reconstructed volume a range of microstructural quantities can be extracted: the orientation and length of the fibres, the fibre volume fraction, the content and distribution of voids, and the presence of manufacturing defects and damage [15], [16]. For short-fibre composites in particular, the mapping of the fibre orientation distribution from tomographic data, including from the large volumes and comparatively low resolutions typical of industrial components, has been developed as a means of feeding measured orientation information into a model [15]. Reviews of the field document the breadth of quantities now recoverable from tomographic data and the growing role of image post-processing, including machine learning and digital volume correlation, in extracting them [16].

The extraction of individual fibres from a reconstructed volume is not trivial, and its difficulty is governed by the ratio of the voxel size to the fibre diameter. When the fibres are only a few voxels across, their cross-sections are poorly resolved, and closely spaced or touching fibres are difficult to separate, so that standard segmentation methods such as the distance-transform watershed tend either to merge neighbouring fibres or to split single fibres. The imaging of short natural- and synthetic-fibre composites by tomography, and the associated difficulties of segmentation at limited resolution, have been reported for a range of material systems [49]. These difficulties are directly relevant to the present work, in which the fibre diameter is a large fraction of the voxel size, and they motivate the dedicated fibre-identification procedure described in Chapter 3.

Beyond the measurement of the undamaged architecture, tomography is used to detect and quantify damage within composites. It has been applied to follow the development of matrix cracking and delamination under mechanical loading [50], and in-situ tomography of laminates cooled to cryogenic temperature has linked the growth of transverse cracks and delaminations directly to the thermal stresses that arise on cooling [31]. As noted in Section 2.3, it has likewise been used to measure the density of transverse matrix cracks in laminates intended for liquid hydrogen tanks, where the cracking arises from the mismatch in thermal expansion between fibre and matrix under thermal cycling [33]. At the highest resolutions, synchrotron tomography resolves the behaviour of individual fibres, including fibre breakage, providing data at the scale of the constituents themselves [51].

The value of tomography for the present work lies not only in the quantities it measures but in the model those quantities inform. The statistical description of the fibre architecture obtained from a tomographic scan is the input to the representative volume element of Section 2.5, and the extraction of that description, its reduction to fitted distributions, and its use in a homogenisation model together constitute the image-based pipeline developed in this thesis. The measurement of the architecture and its use in prediction are thus two halves of a single methodology, whose place in the existing literature is summarised in the following section.

2.7 Summary and Research Gap

The literature reviewed in this chapter establishes both the need for the present work and the tools available to it. The storage of liquid hydrogen for aviation calls for lightweight composite tanks whose walls must retain their integrity at about 20 K and through repeated thermal cycling (Section 2.1). The property that governs the response of such a wall to cooling is the CTE, which differs by an order of magnitude between the polymer matrix and the reinforcing fibre (Section 2.2), and this mismatch generates thermal residual stresses that can nucleate microcracks and, through their coalescence into macroscopic cracks, compromise the structural integrity of the wall (Section 2.3). A short basalt-fibre-reinforced polyamide 11 composite is an attractive candidate for such a wall, offering a recyclable, lower-cost and serviceable material, but it's as-manufactured architecture, the distributions of fibre length, diameter and orientation and its locally varying volume fraction, is non-uniform and governs its thermomechanical response directly (Section 2.4).

The representative volume element, homogenised by the finite element method, is the established framework for predicting the effective properties of such a material from its microstructure (Section 2.5), and X-ray computed tomography is the established means of measuring the real fibre architecture in three dimensions (Section 2.6). Yet the representative volume elements used in most studies are idealised or synthetic, reproducing an assumed rather than a measured microstructure, and the substantial body of work on tomographic characterisation has largely been directed at measuring architecture and damage rather than at supplying the input to a thermal homogenisation.

The gap that this thesis addresses lies precisely in the junction between these two mature techniques. No reported methodology proceeds, in a single and repeatable workflow, from the direct micro-computed-tomography measurement of a short-fibre composite, through the statistical characterisation of its measured fibre geometry and the generation of a three-dimensional representative volume element that

reproduces that geometry, to the finite element homogenisation of that volume for the effective coefficient of thermal expansion and the residual stresses developed on cooling to the liquid hydrogen storage temperature. Developing this end-to-end pipeline, and demonstrating it on a short basalt-fibre-reinforced polyamide 11 composite, is the contribution of the present work. The methodology by which it is achieved is set out in the following chapter.

THIS PAGE WAS INTENTIONALLY LEFT BLANK

3. METHODOLOGY

3.1 Overview of the pipeline

The route followed in this thesis takes a single micro-computed tomography (micro-CT) scan of the short fibre composite and returns a homogenised set of thermo-elastic properties, in four stages: a) imaging and segmentation, b) statistical description of the fibre population, c) reconstruction of a periodic representative volume element (RVE), and d) finite element modelling. Each stage was validated before the next was built on it, so that an error introduced early, during segmentation for instance, could not move forward unnoticed into the RVE. The homogenised properties computed here may need further refinement that was not possible in this thesis: the material properties below RT are engineering estimates rather than measured values, the model contains no voids, and only a single realisation of the microstructure was analysed. These limitations are discussed in full in Section 4.5. The pipeline itself is complete, and each stage has been validated in isolation.

The first stage works on the reconstructed volume directly from the micro-CT. The greyscale scan is binarised to separate the fibres from the polyamide 11 matrix, and the individual fibres are then identified and measured, which gives a length, a diameter and two orientation angles, and their end points for every fibre in the analysed volume. The second stage treats those per-fibre measurements as samples drawn from underlying distributions and fits a probability model to each geometric quantity, so that the microstructure is described by a handful of parameters rather than by the raw voxel data. The third stage uses those distributions to grow a synthetic microstructure: fibres are placed one at a time into a cubic domain by a periodic random sequential addition scheme until the target volume fraction is reached, with the geometry kept periodic across opposite faces. The fourth stage meshes that domain, imposes periodic boundary conditions, and runs the load cases needed to recover the homogenised stiffness and the coefficient of thermal expansion, see Figure 3.1.

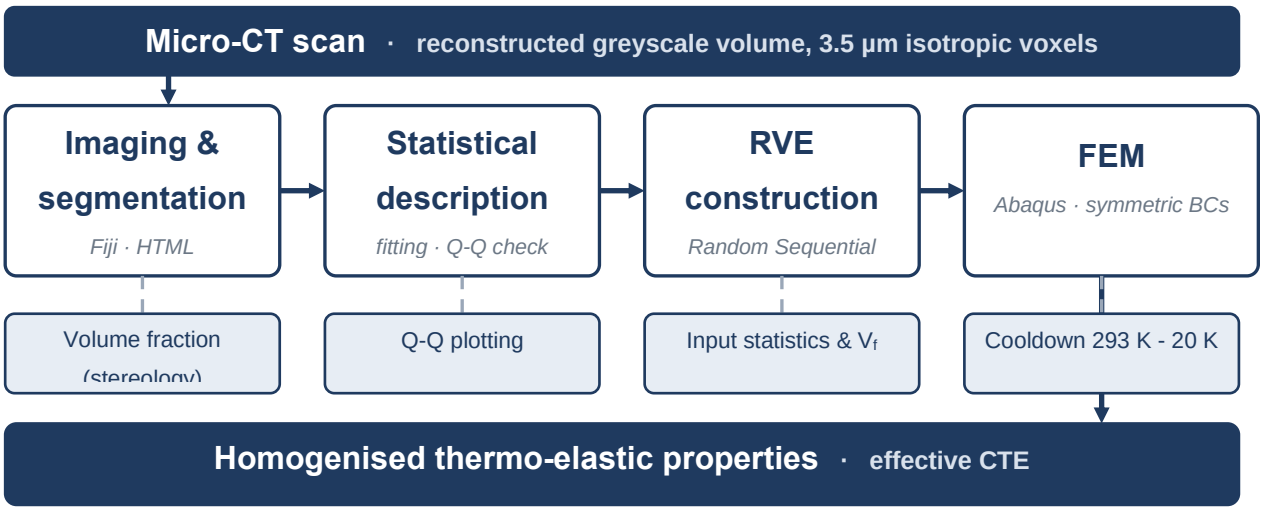


Figure 3.1 The CT-to-RVE-to-FEM pipeline as a whole.

3.2 Micro-CT acquisition and image processing

3.2.1 Sample preparation and scanning parameters

The material studied in this work is a short basalt-fibre-reinforced polyamide 11 composite, produced by additive manufacturing. The specimen scanned here is one of a set of coupons printed in different build orientations; the one used throughout is the XZ-Z coupon, where XZ denotes the plane in which the layers were deposited and the final Z the direction of the print path along which the fibres are laid, a bar of square cross-section measuring 4.5 mm by 4.5 mm and 50 mm long. In the reconstructed volume the length of the bar runs along y, while x and z span the cross-section, and the printed raster, and therefore the fibres, run mainly along z.

This alignment is the physical origin of the microstructure analysed in the rest of the chapter. Because the fibres are laid down along the print path, see Figure 3.2, they emerge strongly oriented along z, and the small scatter of individual fibres about that direction is exactly what the orientation angles of Section 3.3.1 measure. The specific printer and process parameters were not available and so are not reported here; the build orientation, XZ-Z, is the detail that matters for this analysis.

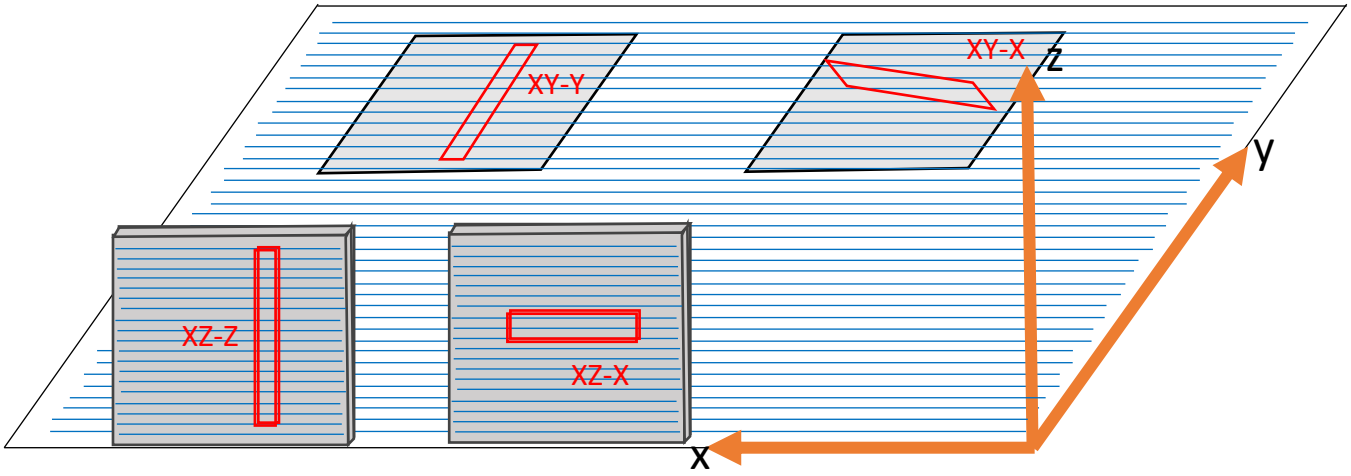


Figure 3.2 Visual representation of build/print orientations.

The specimen was imaged by cone-beam X-ray micro-computed tomography on a laboratory system, with the coupon mounted between the X-ray source and the detector as shown in Figure 3.3. The scan was reconstructed to an effective voxel size of 3.5 µm, isotropic in all three directions, which sets the finest scale resolved in the analysis that follows. The complete set of acquisition parameters, covering the source and detector, the tube voltage and current, the number and range of projections, the exposure, the source-to-object and source-to-detector distances, the reference frames and the reconstruction software, is listed in Table 3.1.

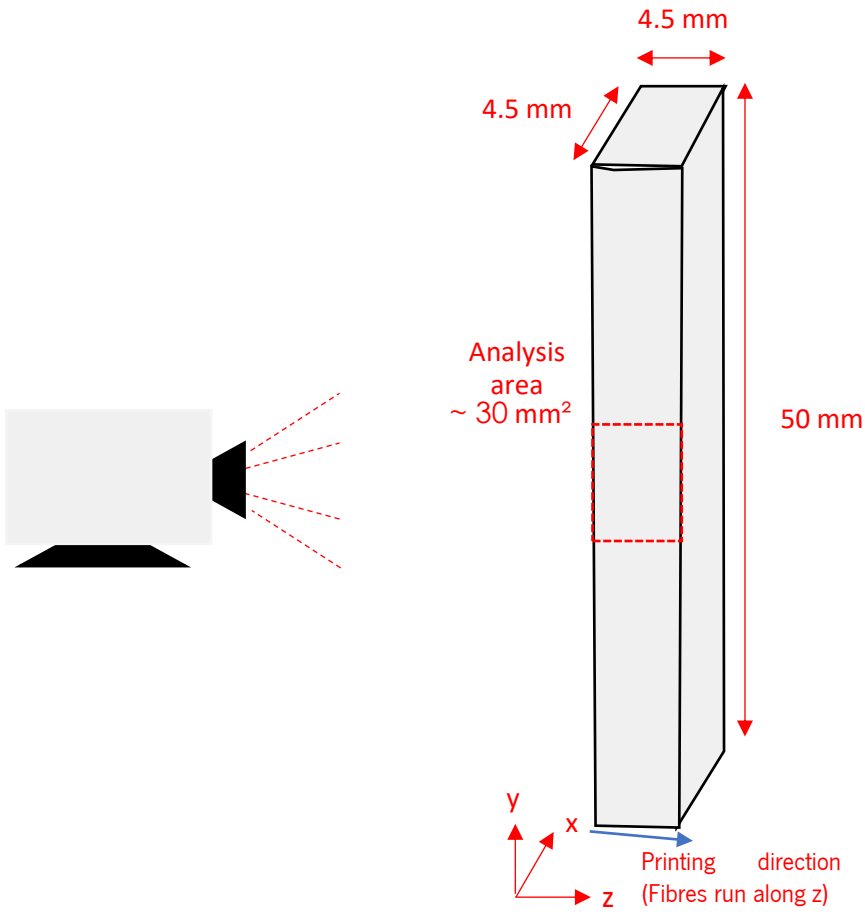


Figure 3.3 Representation of the μ-CT scan geometry: the XZ-Z coupon of Figure 3.2 mounted between the X-ray source and detector, with the analysis region near mid-length. The arrow marks the printing direction, along which the fibres are laid. Axes are those of the reconstructed volume, with the bar length along y and the fibres along z.

Table 3.1 Micro-CT acquisition parameters.

Parameter	**Value**	
Scanner	**X-ray source**	**Detector**
	Hamamatsu L10101	Hamamatsu C7942CA-22 flat-panel, 2400 × 2400 px, 50 μm pixel
Tube voltage	53.0 kV	
Tube current	52 μA	
Beam filter	None	
Projections	1600 over 360°	
Exposure per projection	3 s, averaged over 3 integrations	

Parameter	Value
Source-to-object distance (SOD)	26.827 mm
Source-to-detector distance (SDD)	383.240 mm
Geometric magnification	approximately 14
Effective voxel size	3.5 µm (isotropic)
Flatfield / darkfield frames	26 / 25
Reconstruction software	X-AID (MITOS)
Field of view (FOV)	7.84 mm

3.2.2 Analysed region and sub-volume extraction

A region near the mid-length of the specimen was carried forward for analysis using Fiji [52]. The reconstructed volume covering it measured 442 × 2320 × 433 voxels, which at 3.5 µm per voxel is about 1.55 × 8.12 × 1.52 mm along x, y and z. The length of the bar runs along y, the longest of the three axes; the cross-section lies in the x-z plane, and the fibres run mainly along z. This is clearest in the z view, where each fibre is seen end-on and shows up as a bright dot, so that the slice reads as a field of fibre cross-sections rather than of streaks. Figure 3.4 shows the region in its three orthogonal views, which contain 442, 2320 and 433 slices along x, y and z respectively; these are the three directions along which the tracking tool detects fibres in Section 3.3.1.

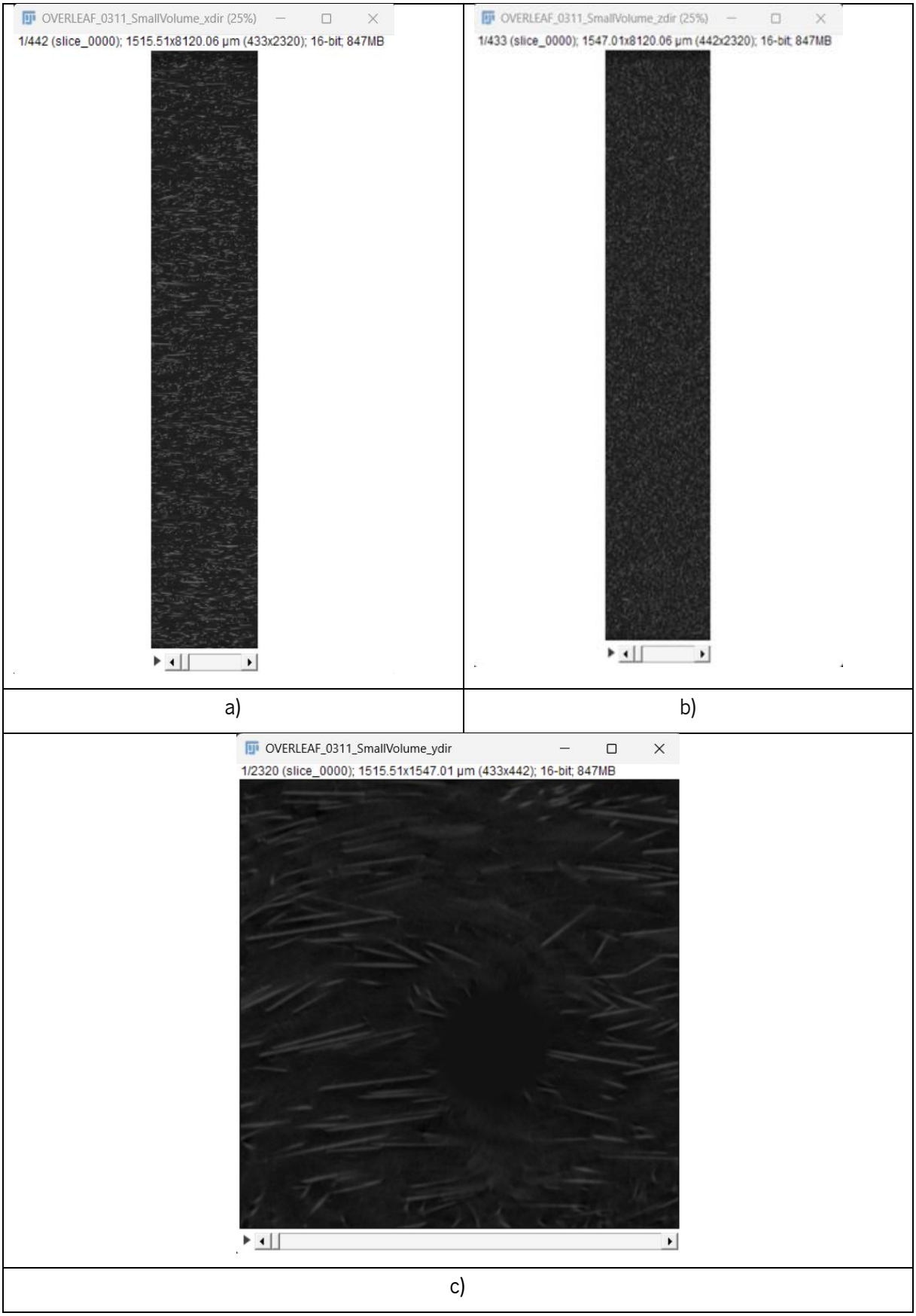
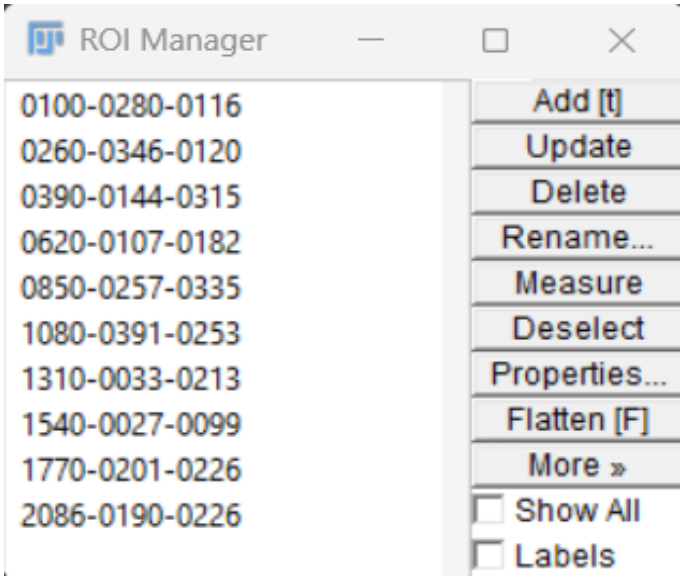
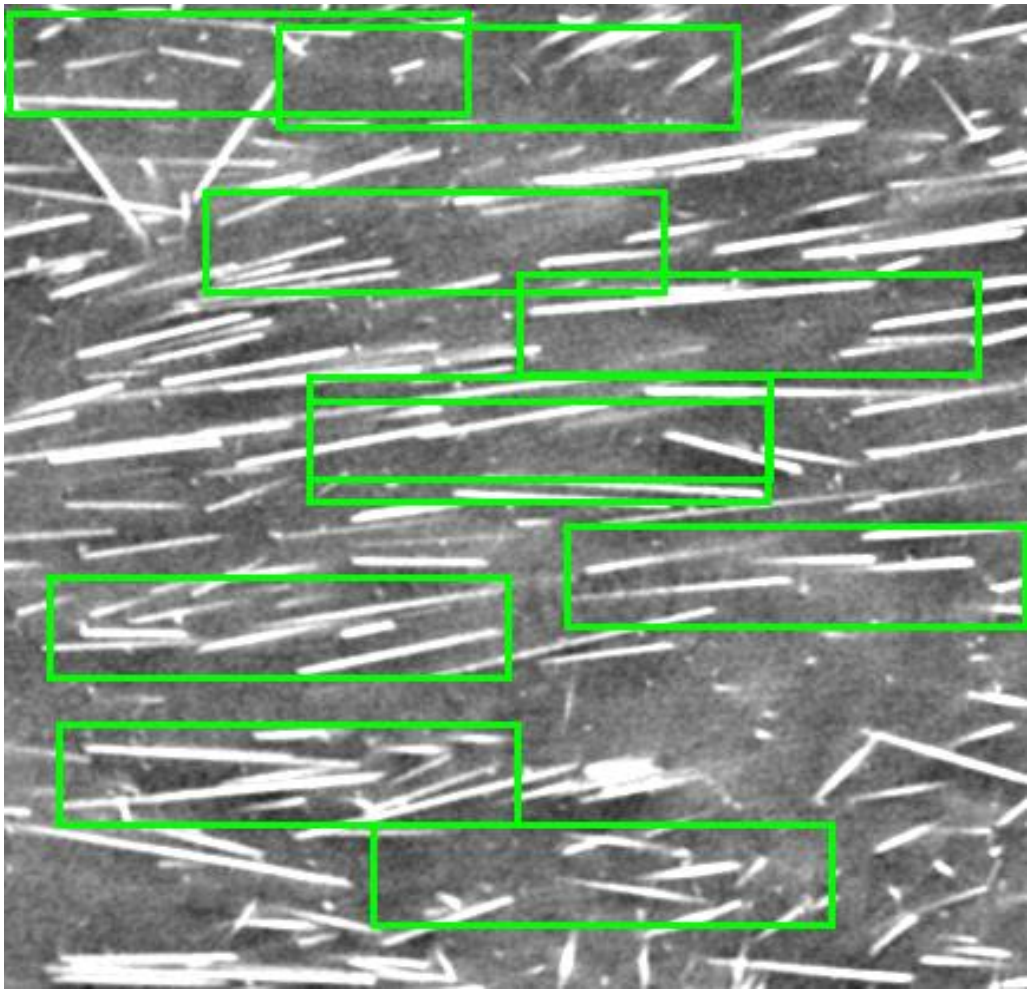


Figure 3.4 Analysed region, matrix is the black background and fibres are in grey, in its different views: a) x-direction (yz view), b) z-direction (xy view) and c) y-direction (xz view).

Rather than analyse the whole reconstructed region at once, ten small sub-volumes were taken from it at different positions. The complete region is too large to pass through the fibre-detection tool of Section 3.3.1 in a single run and even if it passes through the tool, there is a high probability of getting wrong data as an output, so dividing it into smaller sub-volumes keeps each analysis tractable. Sampling ten different positions, rather than a single window, also lets the reported distributions reflect several independent regions of the microstructure. This matters because the fibre content of a printed short-fibre composite varies from place to place. Each sub-volume measured 46 × 10 × 194 voxels, that is 0.161 × 0.035 × 0.679 mm, with its longest side lying along z, the fibre direction. Figure 3.5 shows the ten sub-volumes marked on the region. The slice in Figure 3.5 is displayed with its brightness and contrast enhanced, so that the fibres and the boxes drawn over them stand out clearly. This is a display setting only and does not change the data; the same voxels appear darker and lower in contrast in the raw reconstruction of Figure 3.4.



a)



b)

Figure 3.5 Selection of regions of interest (ROIs) for microstructural analysis: a) The ImageJ/Fiji ROI Manager listing the ten ROIs defined across the reconstructed volume, each labeled by its slice number and center coordinates and b) the corresponding ROIs (green rectangles) overlaid on a representative cross-sectional slice, showing their size and spatial distribution within the specimen.

Each ROI is labeled using Fiji's default three-part convention, `slice-Y-X`, where the first number is the stack slice on which the region was defined and the remaining two give the Y- and X-coordinates (in pixels) of the ROI's center. For example, 0100-0280-0116 denotes a region on slice 100 centered at (X = 116, Y = 280). The different slice numbers in the labels simply record where each region sits in the volume; the regions are placed at different slices and locations on purpose, so the statistics sample several independent parts of the specimen.

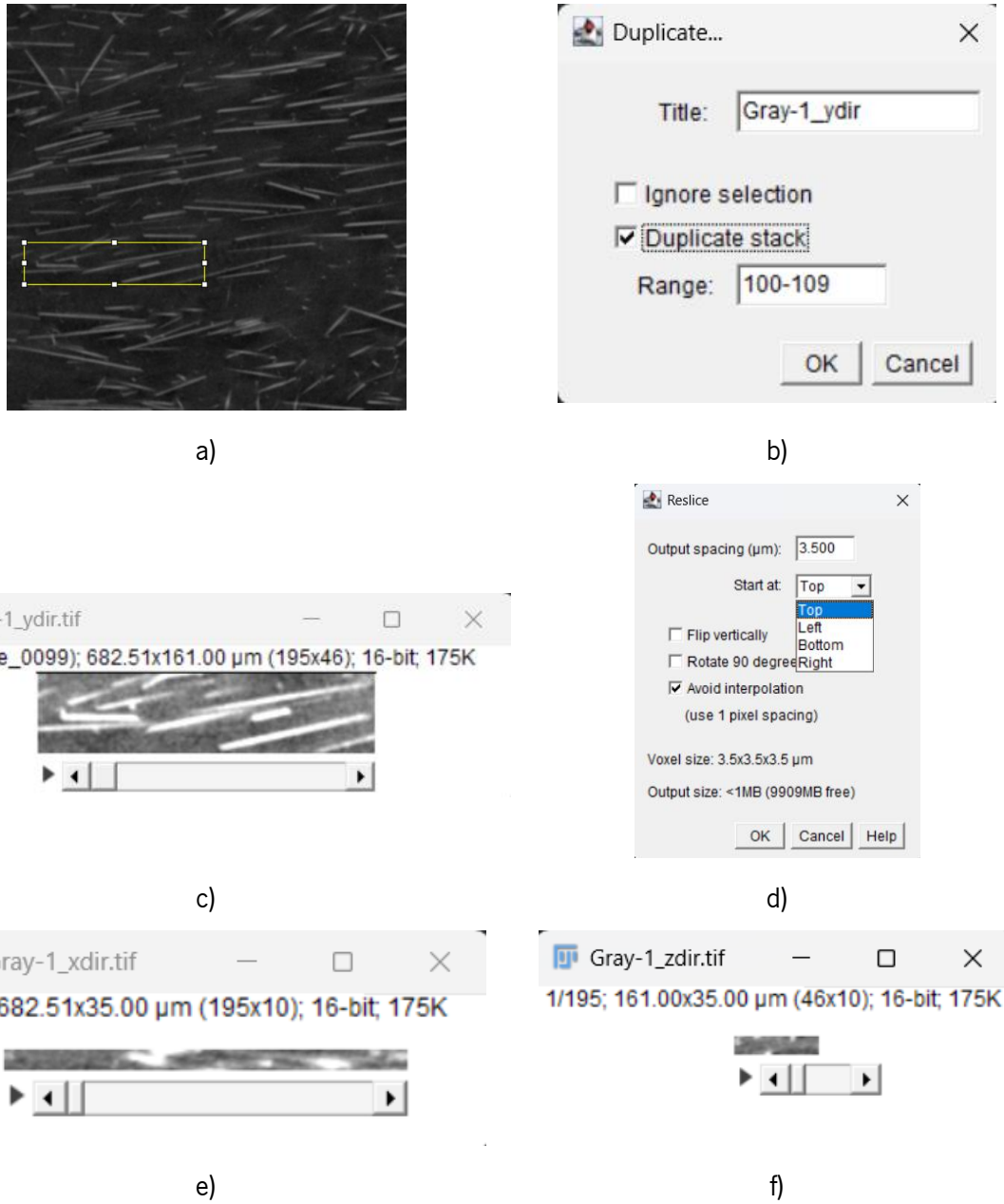
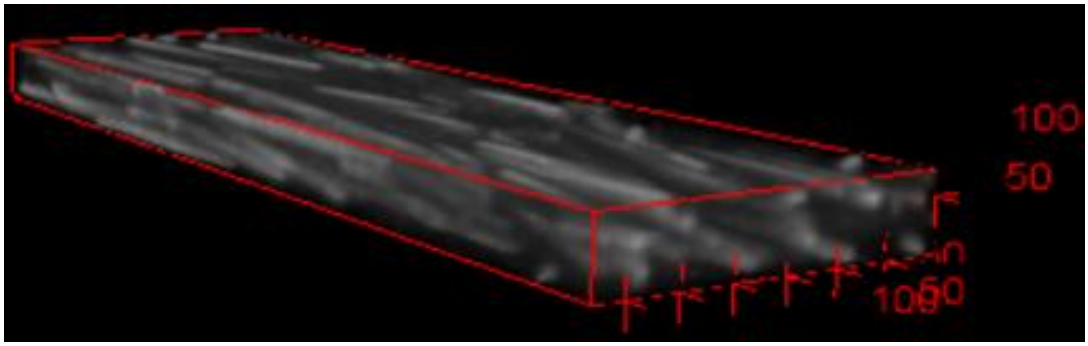
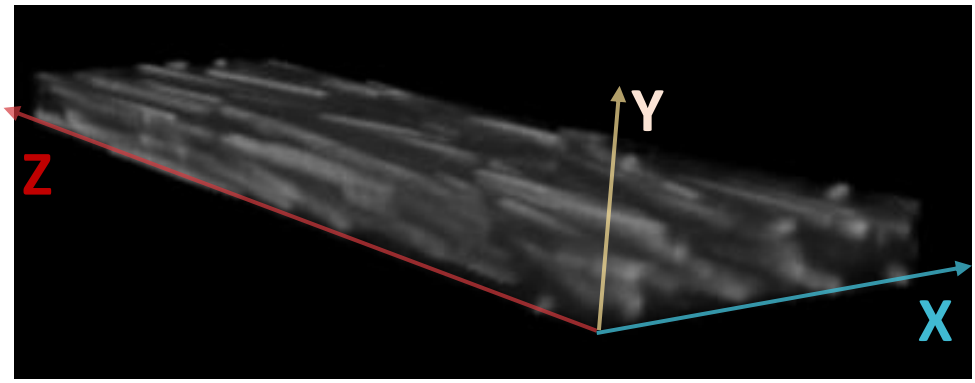


Figure 3.6 Extraction of a sub-volume in Fiji: a) Selecting the sub-volume region on the y-view of the analysed volume, b) Cropping the selection with Duplicate, over the slice range 100 to 109, c) The cropped sub-volume in the y orientation (195 × 46 px, 682.51 × 161.00 µm), d) Reslicing the crop in Fiji at 3.5 µm spacing (Image>Stacks>Reslice), e) The x orientation obtained by reslicing from the top (195 × 10 px, 682.51 × 35.00 µm) and f) The z orientation obtained by reslicing from the left (46 × 10 px, 161.00 × 35.00 µm).

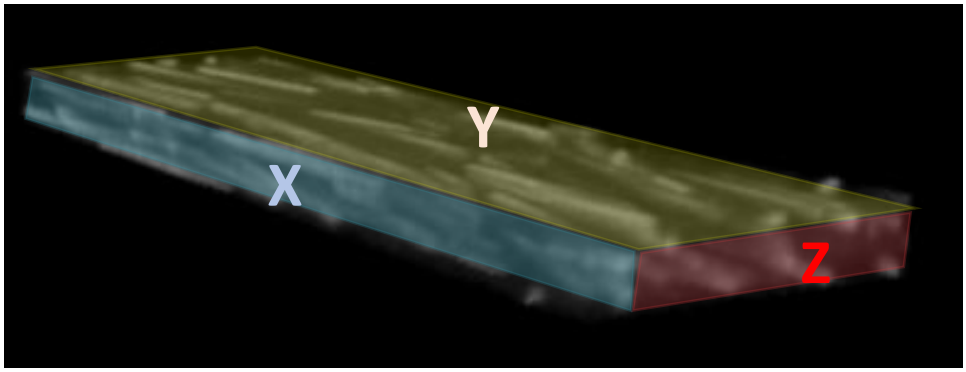
Each sub-volume was cropped once, in the y view of the region, and then resliced in Fiji to produce its x and z orientations. Reslicing the single crop, rather than returning to the region and cropping it again in each direction, guarantees that the three orthogonal views of a sub-volume are one and the same physical volume rather than three separately cut windows that might not align. Figure 3.6 shows the extraction of sub-volume and their reslicing step in Fiji and Figure 3.7 shows the coordinate system and orientation convention of those sub-volumes.



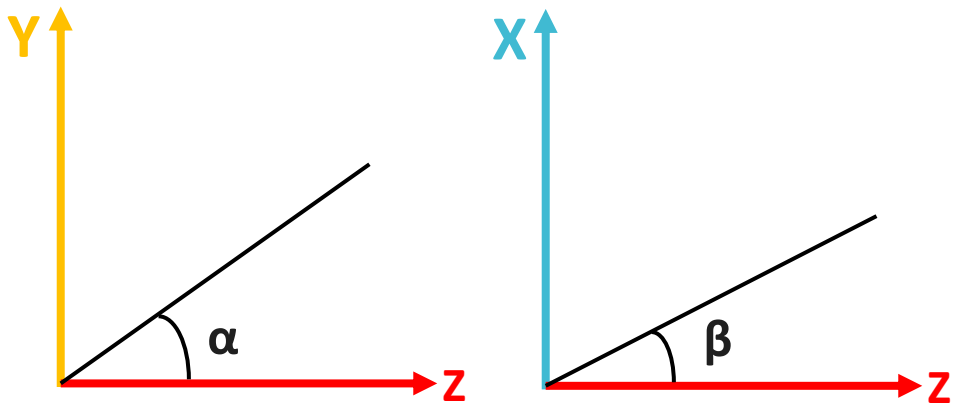
a)



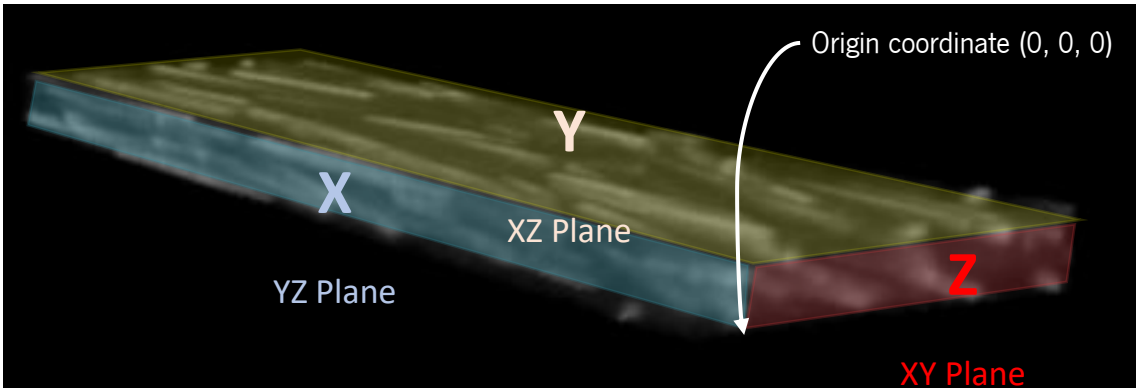
b)



c)



d)



e)

Figure 3.7 Coordinate system and orientation convention for a sub-volume: a) Default three-dimensional (3D) rendering of a sub-volume in Fiji, b) The x, y and z axes of the sub-volume, with the fibres running along z, c) The three orthogonal planes (YZ, XZ and XY planes) of the sub-volume, d) The orientation angles defined relative to the z axis: $\alpha \rightarrow$ Upward/downward tilt (out of plane angle), $\beta \rightarrow$ sideways tilt/rotation (in-plane angle) and e) The origin of the reference coordinate system at (0, 0, 0). The origin fixes the reference frame only; α and β are computed from each fibre's direction and do not depend on its position.

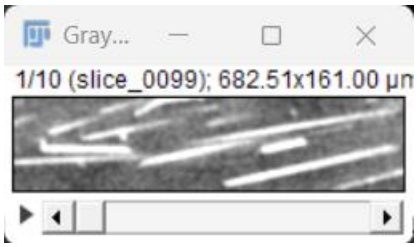
Each of these ten sub-volumes was then binarised (Section 3.2.3) and passed through the fibre-tracking tool (Section 3.3.1).

3.2.3 Image segmentation: binarisation in Fiji

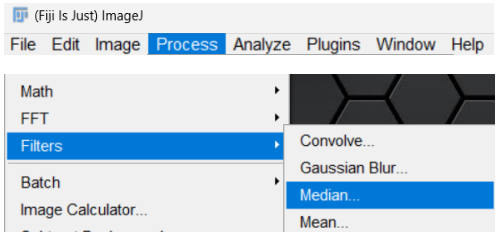
Binarising the scan means converting the greyscale volume, in which each voxel holds a grey level, into a two-value image in which each voxel is either fibre or matrix. Here the fibre material is set to foreground (white) and the polyamide 11 matrix to background (black), which is the binary volume the fibre-detection tool requires. The fibre-extraction tool of Section 3.3.1 takes two inputs: the original greyscale volume and a binary volume in which the fibre material (Basalt fibre) is marked as foreground (white) and the matrix material (Polyamide 11) is marked as background (black). Each of the ten sub-volumes was binarised separately, so that the threshold could follow the local grey levels of that sub-volume rather than be forced to a single value across the whole scan. This produced ten binary sub-volumes and, with them, ten threshold values, which are listed in Table 3.2.

The binarisation was carried out in Fiji in three steps, shows in Figure 3.8, applied to each sub-volume in turn. First, a median filter of radius one voxel was applied across the whole stack (Process>Filters>Median, with Stack selected) to suppress voxel-scale noise without softening the fibre edges. Second, the contrast was stretched with Enhance Contrast (0.3% saturated pixels, normalised, applied to all slices), which pushes the fibre and matrix grey levels as far apart as the data allow. Third,

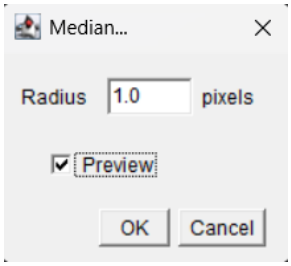
the volume was thresholded by Otsu's method (Image>Adjust>Threshold>Otsu), with the threshold bar then nudged by eye around the value Otsu returned until the binary fibres matched the greyscale image without bridging neighbours or breaking apart as much as possible. The threshold finally used for each sub-volume is given in Table 3.2.



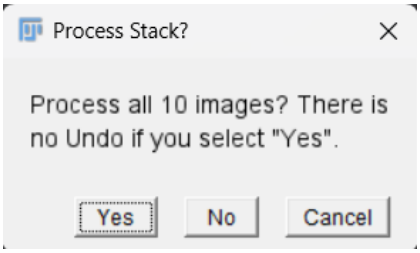
a)



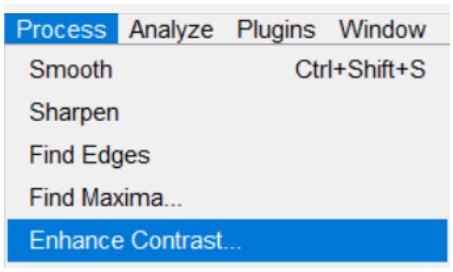
b)



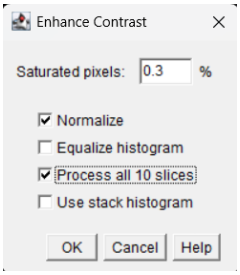
c)



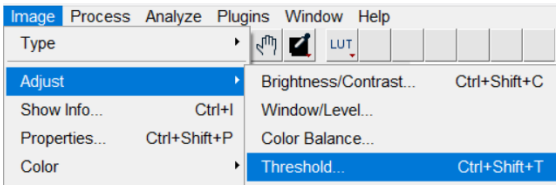
d)



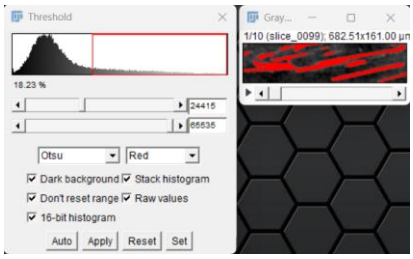
e)



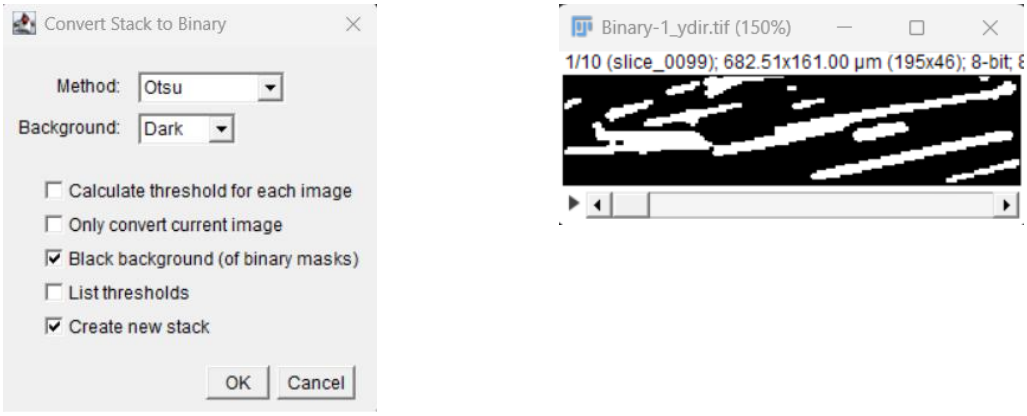
f)



g)



h)



i) j)

Figure 3.8 Binarisation of a micro-CT sub-volume in Fiji: a) The greyscale sub-volume before processing, b) Opening the median filter (Process>Filters>Median), c) The median filter set to a radius of one pixel, with live preview, d) Applying the filter to all ten slices of the stack, e) Opening Enhance Contrast (Process, Enhance Contrast), f) Enhance Contrast set to 0.3% saturated pixels, normalised, over all ten slices, g) Opening the threshold tool (Image, Adjust, Threshold), h) The Otsu threshold shown on the stack, dark background, with the selected fibres in red (18.23%), i) Converting the stack to a binary mask by Otsu's method, dark background, with the threshold calculated for all slices and j) The resulting binary sub-volume, fibres in white on a black background.

Because these steps are identical for every sub-volume, and there are many stacks to work through, they were not repeated by hand each time but wrapped in an ImageJ macro that fixes every setting and stops only for the one decision a person has to make, the threshold. The macro is listed in full in Appendix 1; but its main parts are described here.

The macro is pointed at a folder and works through the stacks inside it, opening only the greyscale files, so that the originals and any binaries already written are left untouched:

```
inDir = getDirectory("Choose the folder containing your stacks");
list  = getFileList(inDir);
for (i = 0; i < list.length; i++) {
   name = list[i];
   // only open raw greyscale .tif stacks: protects originals, skips outputs
   if (endsWith(toLowerCase(name), ".tif") && indexOf(name, "Gray") >= 0) {
      open(inDir + name);
      // ... process this stack ...
   }
}
```

For each stack it forces a black background, so the fibres will come out white, and then runs the two preprocessing steps automatically at their fixed settings:

```
setOption("BlackBackground", true);   // fibres end up white on black
```

```
run("Median...", "radius=1 stack");    // denoise the whole stack, radius 1
run("Enhance Contrast...", "saturated=0.3 normalize process_all"); // stretch contrast
```

It then opens the threshold tool, sets an Otsu value as a starting point, and pauses. This is the only interactive moment in the run: the user slides the threshold until the fibres are picked out in red, exactly as in Figure 3.8(h), and clicks OK. The value settled on here is the one entered in Table 3.2.

```
run("Threshold...");
setAutoThreshold("Otsu dark stack");   // an Otsu value as a starting guess only
waitForUser("Set threshold",
   "Adjust the sliders until the fibres are red, then click OK.");
```

Once the user confirms, the macro finishes on its own. It converts the thresholded stack to a binary mask using the value just set, then saves the result in the same folder under a new name, with "Gray" swapped for "Binary":

```
run("Convert to Mask");                // apply the threshold just set
outBase = replace(base, "Gray", "Binary"); // Gray-1_xdir  ->  Binary-1_xdir
saveAs("Tiff", inDir + outBase + ".tif");
```

Since everything but the threshold is fixed, the ten sub-volumes are binarised in an identical way apart from that single value, which is what keeps the step both fast and repeatable.

Each sub-volume is binarised on its own grey levels because the brightness and contrast of the reconstruction are not uniform across the scanned region. Local intensity variation, from the cone-beam geometry and from beam hardening, shifts the fibre and matrix grey levels from one sub-volume to another, so a single threshold applied to the whole scan would select too much fibre in the brighter regions and too little in the darker ones. Setting the threshold separately for each sub-volume therefore separates fibre from matrix faithfully everywhere, and the ten resulting values are checked against the expected fibre content in Section 3.2.4.

Table 3.2 Otsu threshold grey percentage [as shown in Figure 3.8 (h)] used for each of the ten sub-volumes.

Sub-volume	Threshold (%)
1	18.23
2	22.12

Sub-volume	Threshold (%)
3	21.49
4	14.34
5	16.19
6	23.30
7	15.73
8	18.83
9	17.91
10	20.83

The obvious next step, and the standard one, would have been to separate the individual fibres inside these binary sub-volumes with a distance-transform watershed, for example the 3D watershed using the MorphoLibJ plugin [53] in Fiji. This route was tried first and did not produce usable fibres. The low contrast of the scan and the density of touching fibres defeated the watershed in both directions at once: single fibres were split into several fragments, while neighbouring fibres were merged into one cluster, and neither could be tuned away without making the other worse. That failure is what motivated the custom detection-and-tracking tool described in Section 3.3.1, which works from the greyscale and the binary together rather than from the binary alone.

3.2.4 Validation of the binarisation

The binarisation was checked through the fibre volume fraction. Since the binary marks fibre material as foreground, the proportion of foreground voxels in a sub-volume is its fibre volume fraction, which is the percentage already reported for each sub-volume in Table 3.2. Averaged over the ten sub-volumes this fraction is 18.897% (about 19%), close to the target fibre fraction of 20% (as shown in Figure 3.10) for this basalt-fibre-reinforced polyamide 11 composite.

The agreement is a check on the threshold rather than on the fibres themselves. A threshold set too high would have discarded fibre material and pulled the fraction below the target, while one set too low would have counted matrix as fibre and pushed it above; that all ten sub-volumes sit close to 20% shows the threshold was placed sensibly in each, see Figure 3.9. The fibre extraction carried out on these binary volumes is validated separately in Section 3.3.2.



a) b) c)

Figure 3.9 Binarisation check on one sub-volume: a) binary mask, b) greyscale slice and c) fibre outlines from the mask overlaid on the greyscale, showing that the binarisation captured the fibres well.

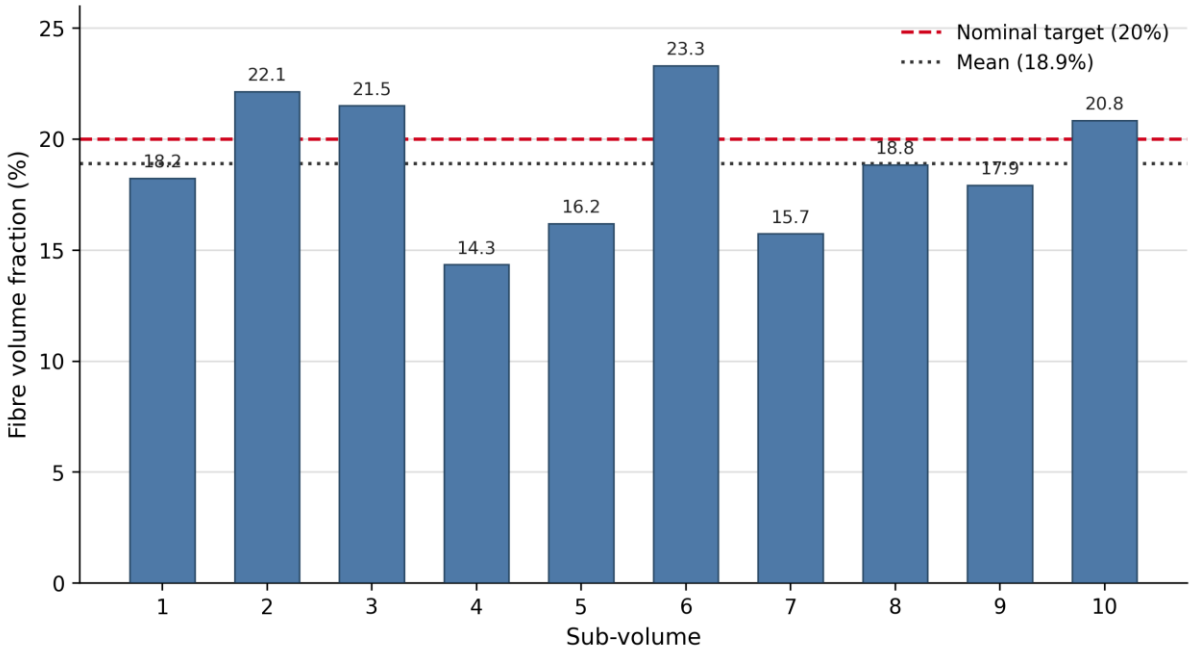


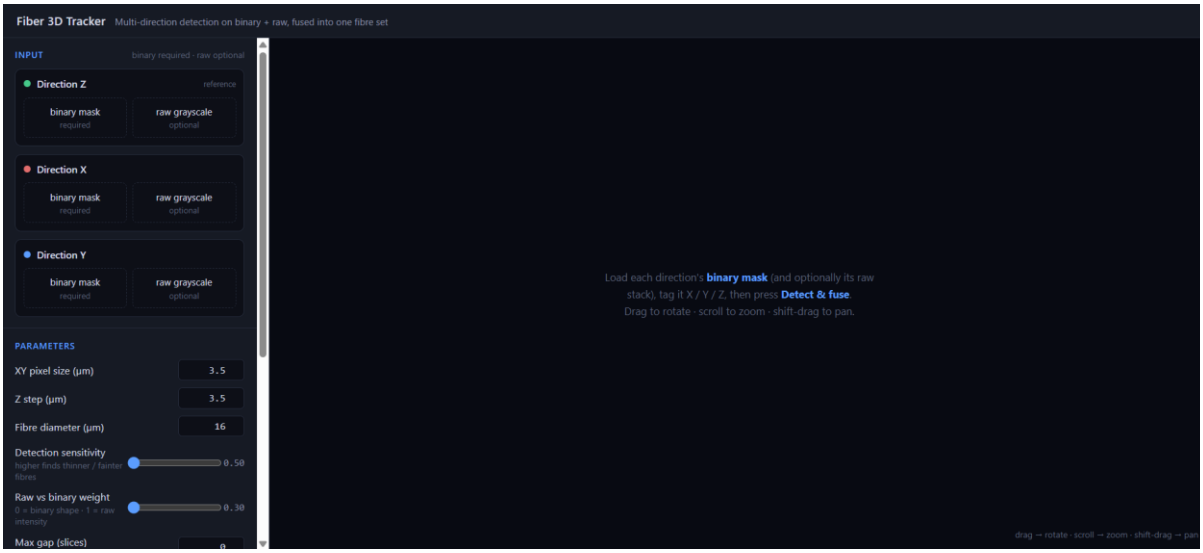
Figure 3.10 Fibre volume fraction of the ten sub-volumes obtained from the binarisation, compared with the nominal 20 per cent target. The mean is 18.9 per cent, and all ten values lie close to the target, confirming that the threshold was placed sensibly in each sub-volume.

3.3 Microstructural characterisation

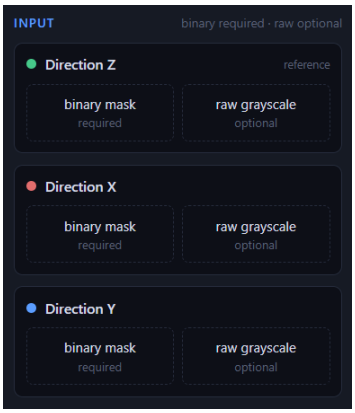
3.3.1 Fibre identification and geometric measurement

The individual fibres were identified and measured with a custom-built HTML code-based tool, implemented as a browser-based application, that takes the greyscale and binary volumes of Section 3.2.2 and returns, for every fibre, its length, its diameter and its orientation, shows in Figure 3.11 and 3.12. Rather than segment the three-dimensional binary directly, the tool works slice by slice: it locates fibre cross-sections in each slice and links them through the stack, from one slice to the next at the 3.5 µm slice spacing of the reconstruction, into three-dimensional fibres. The reasoning is that a fibre crossing a slice close to end-on appears as a compact, near-circular cross-section that is easy to find and to follow, whereas the same fibre viewed along its length appears only as an ambiguous streak. The stages below

build on that observation. In each, the essential lines of the routine are shown, and the complete source is listed in Appendix 2.



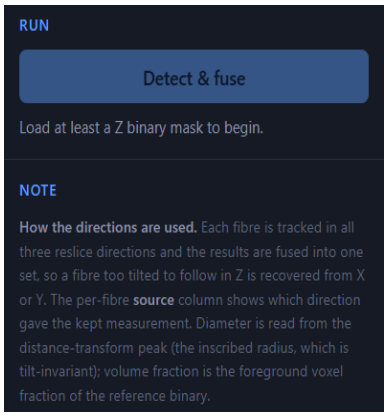
a)



b)



c)

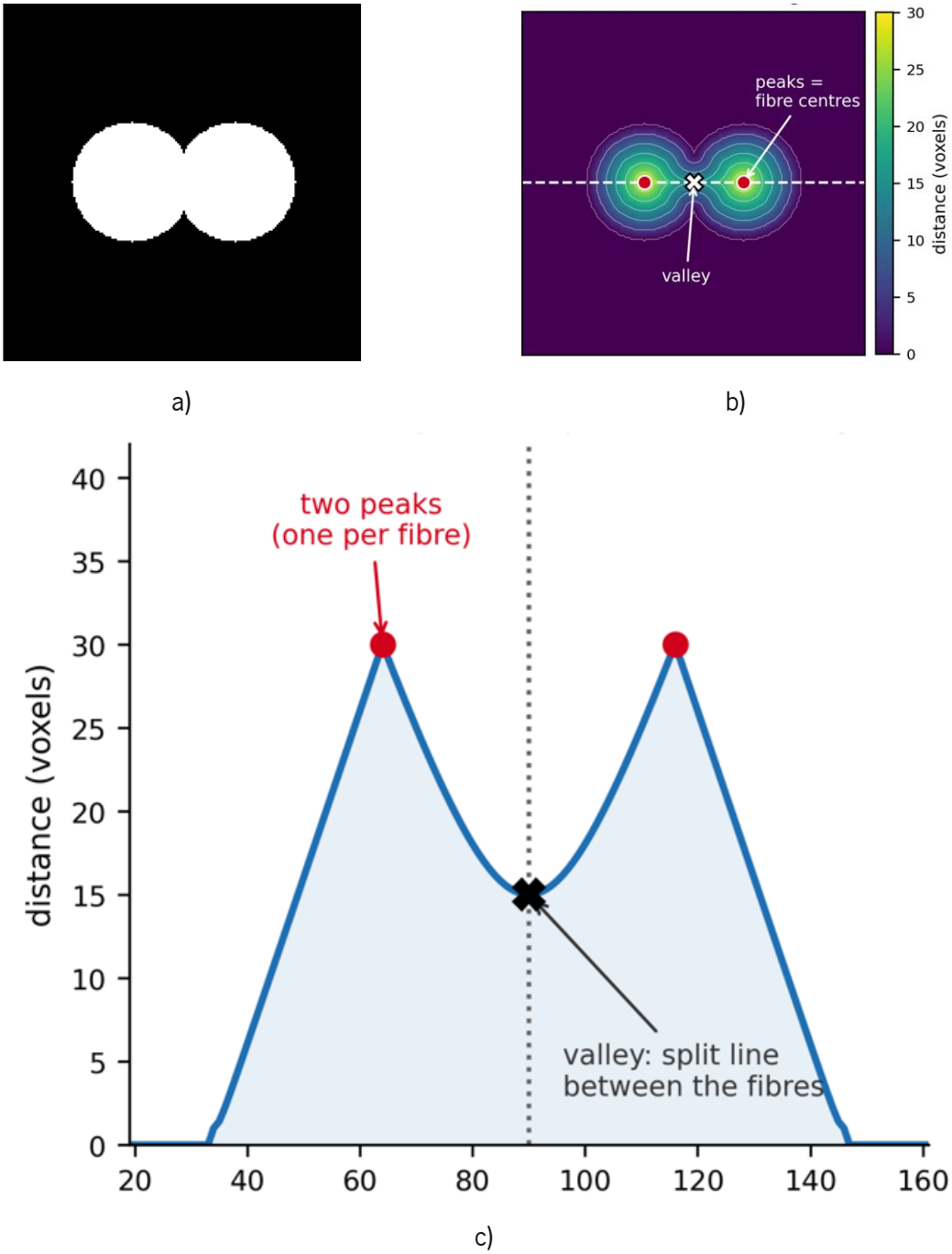


d)

Figure 3.11 The browser-based fibre-tracking tool used for fibre identification: a) The full interface of the tool, b) Input panel, where the sub-volume is loaded in its three reslice orientations, c) Parameters panel, set to the values used in this fibre identification and d) Run control panel and the note on how the three directions are fused into a single fibre set.

Cross-section detection: Within each slice the binary supplies the fibre foreground, on which an exact Euclidean distance transform is computed. This returns, at every foreground voxel, the distance to the nearest background, which for a fibre cross-section is the radius of the largest circle that fits inside it and does not change as the fibre tilts. Fibre centres are taken as the local maxima of this distance map, so that two touching fibres are split at the valley between their peaks. Where fibres touch so closely that the binary leaves no valley, the greyscale intensity is blended into the response, in the proportion set by the raw-versus-binary weight, to recover the separation the binary lost. Each centre is refined to sub-voxel

precision, detections closer than about one fibre radius are suppressed, and a compactness test discards any detection whose surrounding foreground forms a long streak rather than a compact blob, which removes fibres caught side-on, as shown in Figure 3.12.



a) b) c)

Figure 3.12 Fibre-centre detection by the distance transform, shown for two touching fibres (representative): a) the binary cross-sections, b) the Euclidean distance transform, in which each voxel holds its distance to the nearest background and is largest at the fibre centres, and c) a profile across the two centres, where each fibre appears as a peak and the two are separated at the valley between them. The largest inscribed distance at a centre is the fibre radius and does not change as the fibre tilts.

```
// blend the binary distance-transform shape (dn) with the raw intensity (rt)
```

```
R[i] = (1 - alpha) * dn + alpha * rt;

// keep only local maxima of R that clear the sensitivity-set minimum radius
if (isMax) cand.push({ x: x, y: y, r: dist[idx], val: R[idx] });

// compactness gate: drop side-on fibres seen as long streaks
if (longestChord(mask, w, h, cx, cy) > 2.5 * Math.max(2 * r, 2)) reject();
```

Linking across slices. The detected centres are joined from one slice to the next into tracks, each track being one fibre followed through the stack. A fibre's position is predicted from slice to slice at constant velocity, so that an inclined fibre is followed along its diagonal path, and each centre is joined to the nearest prediction. Short interruptions, where a fibre is missed on a slice or two, are bridged up to a set maximum gap, and tracks shorter than a minimum length are discarded as noise.

```
// predict the next centre by constant velocity from the last two slices
predX = last.x + (last.x - p2.x) / dz * gap;
predY = last.y + (last.y - p2.y) / dz * gap;

// join the nearest centre within tolerance; up to maxGap missed slices allowed
if (dPred <= maxDist * gap) pairs.push({ ti: ti, j: j, cost: dPred / gap });

// tracks shorter than the minimum length are discarded
```

Three viewing directions. Detection and linking are carried out three times, slicing the volume along each of its axes in turn. This is necessary because a fibre lying nearly parallel to one slicing direction is exactly the side-on case that direction cannot resolve, yet it is close to end-on for one of the other two. Running all three directions therefore captures fibres of every orientation. The three sets are then brought into one common frame by testing the axis assignments that map each direction onto the others and keeping the one that makes their foregrounds overlap best.

```
// run detection and linking with each axis in turn as the slice normal
for (var axis = 0; axis < 3; axis++) perDir[axis] = track(detect(axis));

// register the directions into one common frame by the best foreground overlap
best = transform maximising jaccard(occupancy(dir, transform), refOcc);
```

Fusion. Because a fibre near the diagonal can be caught in more than one direction, the same physical fibre may be detected twice or three times. These duplicates are merged. Fibres are processed from the longest and most end-on capture downward, and a shorter detection is absorbed into a longer one when its centre-line runs along the longer fibre's axis, within a tolerance of about one fibre radius. Because the tolerance scales with radius, genuinely separate parallel fibres, whose centres sit at least a diameter apart, are never merged. Each fibre is then represented by its single fullest and most end-on capture.

```
// process the longest, most end-on fibres first as anchors
// absorb a shorter fibre when its centre-line follows the anchor's axis
if (anchorDist(anchor, cand) < 1.2 * Math.max(radius, voxel)) merge(cand);


// the tolerance scales with radius, so distinct parallel fibres stay separate
```

Measurement. For each fused fibre the axis is fitted to its centre-line points by principal component analysis, which gives the fibre's unit direction. The length is the extent of the points along that axis, and the diameter is twice the median of the inscribed radii measured along the fibre.

```
// fibre axis by PCA: power iteration on the covariance of the centre-line points
for (var it = 0; it < 40; it++) v = normalise(matMulVec(C, v));


length   = maxProj - minProj;        // extent along the fitted axis
diameter = 2 * median(radii);        // twice the median inscribed radius
```

Orientation. Orientation was described by the fibre's unit direction vector u = (u_x, u_y, u_z), with the sign fixed so that u_z is non-negative. Two angles were derived from it: an elevation, α, the tilt of the fibre out of the x-z plane towards y, and an azimuth, β, the rotation within the x-z plane measured from the z axis towards x,

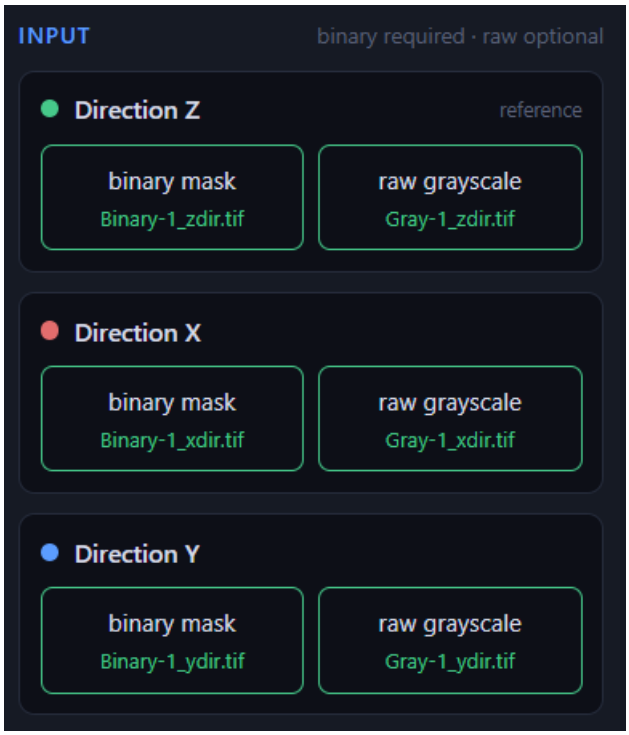
$$\alpha = arcsin(u_y) \tag{3.1}$$

$$\beta = arctan2(u_x, u_z) \tag{3.2}$$

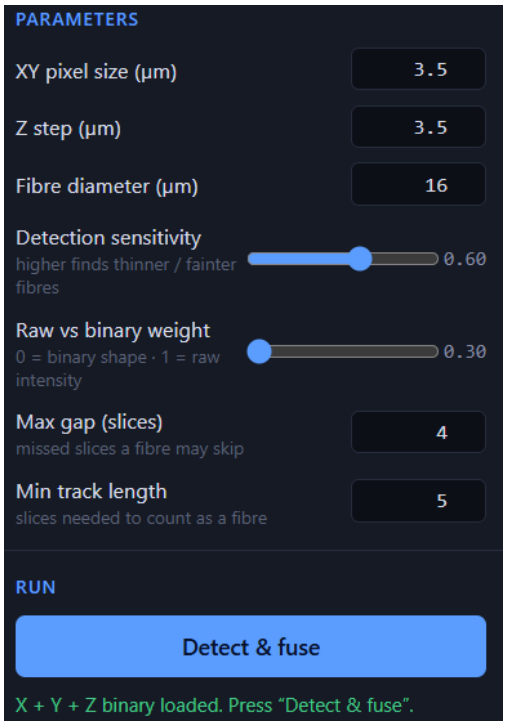
A fibre aligned with the z axis has α and β both close to zero, and because the population is strongly z-aligned, the two angles are small. That is what makes them suitable for the distribution fitting of Section 3.3.2. A raw azimuth, by contrast, would jump between +180° and −180° for these near-axial fibres and could not be fitted directly.

```
var sgn = d[2] < 0 ? -1 : 1;                    // fix the sign so u_z >= 0
```

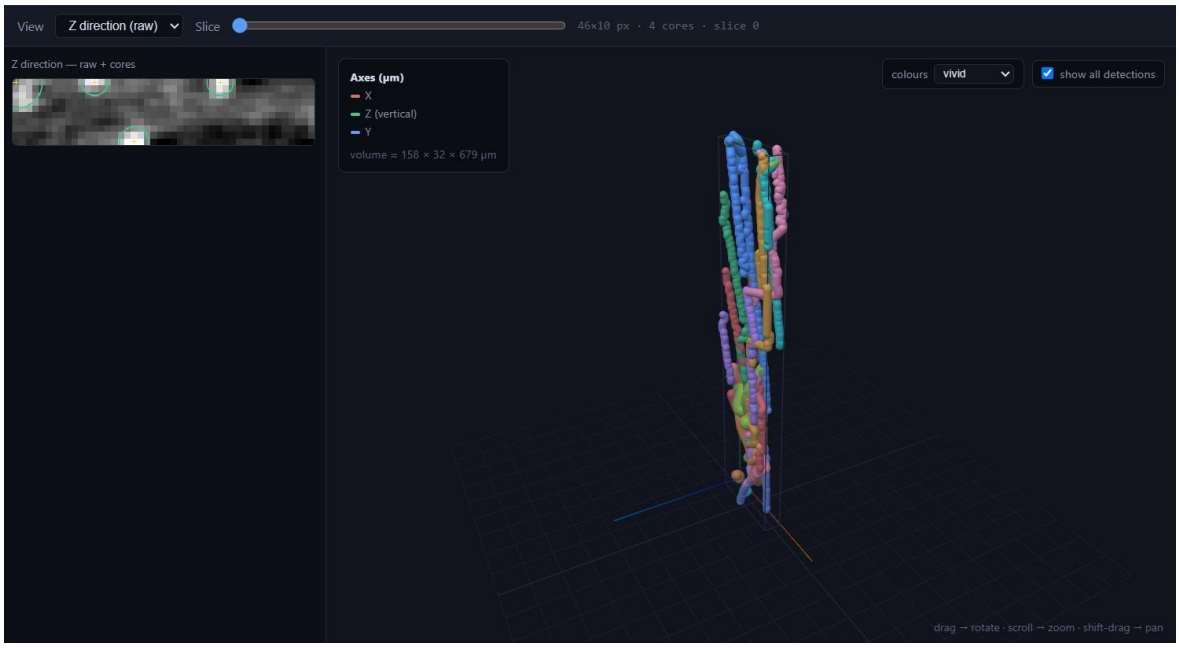
```
var alpha = Math.asin(uy) * 180 / Math.PI;      // arcsin(u_y)
var beta  = Math.atan2(ux, uz) * 180 / Math.PI; // arctan2(u_x, u_z)
```



a)



b)



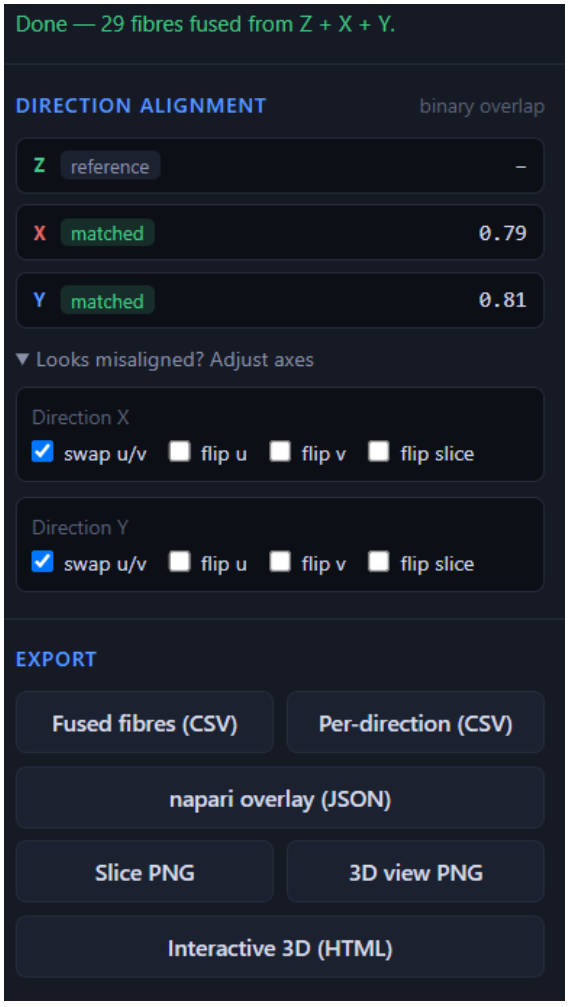
c)

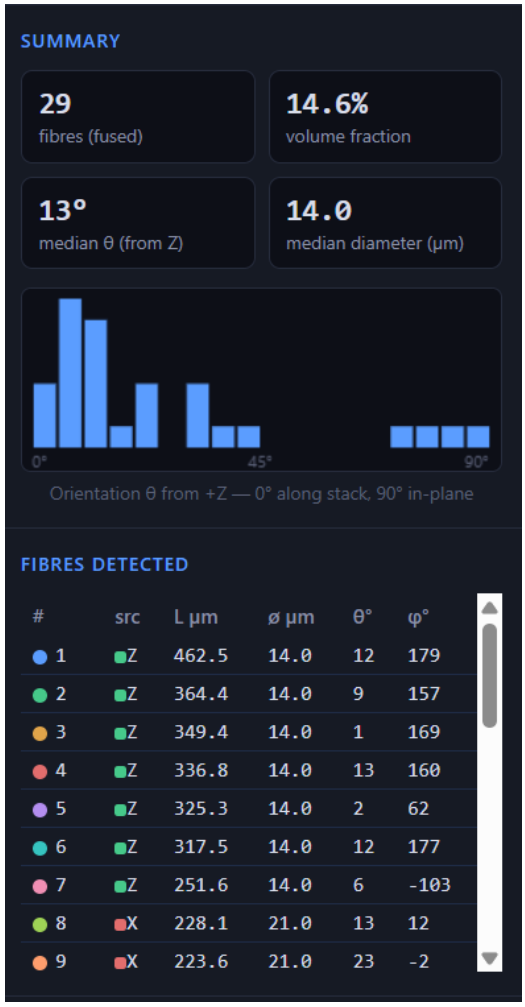




d)

After clicking “Detect & fuse”





e) f)

Figure 3.13 The fibre-tracking tool in operation on a sub-volume: a) The three directional stacks loaded into the tool, each as a binary mask with its raw greyscale, b) The parameter values used for the run, c) The fibres reconstructed in three dimensions after fusion, d) Detected fibre cross-sections, marked by circles, on slice 53 of the z-direction stack, e) Direction alignment and export panel: the X and Y detections registered to the Z reference by binary overlap (scores 0.79 and 0.81), and the export options, including the fused-fibre CSV and f) Summary panel for the sub-volume: the number of fused fibres, their volume fraction, median orientation and median diameter, with the orientation histogram below.

The parameter values used for the analysis reported here are listed in Table 3.3.

Table 3.3 Parameters used in the fibre-tracking tool.

Parameter	Value	What it controls
Voxel size (isotropic)	3.5 µm	The physical size of a voxel, so pixel and slice spacing are in real units. Fixed by the scan.
Nominal fibre diameter	16 µm	The expected fibre diameter, so the detector searches for cross-sections of the right size. Fixed by the material.
Detection sensitivity	0.60	How readily a cross-section is accepted as a fibre. Higher values detect fainter and thinner fibres, at the risk of false detections.
Raw-versus-binary weight	0.30	The balance between the binary shape and the raw greyscale when separating touching fibres. 0 uses the binary alone; higher values lean on the greyscale to split fibres the binary has merged.
Maximum gap	4 slices	The largest run of missed slices bridged within a single fibre track, so a fibre briefly lost is not broken into two.
Minimum track length	5 slices	The fewest slices a track must span to be kept as a fibre, which discards short spurious detections as noise.

Two of these values are fixed rather than chosen: the voxel size is that of the reconstructed scan, and the nominal fibre diameter is the expected fibre diameter. The other four were tuned to suit this dataset and confirmed by the overlay check of Section 3.3.2, where the detected fibres are compared directly against the raw image.

The output of the tool is a table, exported as a CSV file with one row per fused fibre (Figure 3.14). Each row records that fibre's geometry: an identifier (fibre_id), its length and diameter in micrometres (length_um, diameter_um), its orientation angles α and β in degrees (alpha_deg, beta_deg), and the two endpoints of its axis in image coordinates (x1_um, y1_um, z1_um and x2_um, y2_um, z2_um). The rows are ordered by fibre length. One such file is produced for each of the ten sub-volumes, so that the ten files together hold the full population of measured fibres. This is the form in which the microstructure passes to every later step: the distributions of Section 3.3.3 are fitted to the length, diameter and orientation columns pooled across the ten files, and the overlay of Section 3.3.2 is drawn directly from the endpoints and diameters of one file.

	A	B	C	D	E	F	G	H	I	J	K
1	fibre_id	length_um	diameter_um	alpha_deg	beta_deg	x1_um	y1_um	z1_um	x2_um	y2_um	z2_um
2	1	678.24	14	-0.9	-9.7	134.64	10.29	14.05	19.9	-0.1	682.43
3	2	336.77	9.9	4.3	-11.8	69.02	-2.58	122.65	0.18	22.48	451.35
4	3	317.86	14	1.1	-12.2	148.28	-1.23	367.93	81.19	4.85	678.57
5	4	285.41	14	-1.2	-6.6	164.09	33.08	365.73	131.19	26.95	649.17
6	5	254	14	4.4	-10.6	42.04	5.27	334.04	-4.64	24.78	582.96
7	6	207.44	15.65	3.6	-17.7	57.8	1.58	59	-5.07	14.71	256.25
8	7	225.04	9.9	0	-3.3	115.72	31.5	226.02	102.76	31.5	450.69
9	8	215.87	14	-5.2	-7.9	161.43	19.4	469.07	131.9	-0.03	682.03
10	9	204.84	14	-0.4	-13.4	83.99	31.42	469.25	36.5	30.08	668.5
11	10	155.26	15.65	1.5	5.3	81.72	-0.68	37.44	96.04	3.3	191.98
12	11	138.04	15.65	-8.8	20.9	63.42	34.82	1.13	112.08	13.64	128.56
13	12	134.4	14	0.4	-10.9	106.96	24.69	126	81.5	25.52	257.97
14	13	134.37	14	0	-9.1	161.46	31.5	546.17	140.14	31.5	678.83
15	14	130.55	14	-0.5	12.5	120.89	28.77	132.61	149.14	27.57	260.06
16	15	125.19	14	0.6	-14.2	27.89	30.55	249.08	-2.87	31.87	370.42
17	16	106.64	14	5.6	-22.9	2.99	8.71	677.79	44.26	-1.71	580.02
18	17	106.18	14	13.8	45.3	51.17	-3.34	51.14	124.46	21.93	123.7
19	18	100.83	14	21.2	37.8	54.69	-4.74	174.62	112.31	31.74	248.88
20	19	93.21	14	20	48.1	47.14	0.84	343.14	112.28	32.76	401.66
21	20	76.08	14	23.6	30.8	-9.47	-6.45	618.15	26.29	23.95	678.02
22	21	75.98	14	7.6	-15.8	98.08	12.62	317.76	77.6	22.71	390.24
23	22	73.38	14	27.6	32.6	4.64	-0.94	628.7	39.69	33.02	683.5
24	23	70.97	14	0	-11	88.02	0	434.17	74.52	0	503.83
25	24	62.37	14	-13.9	-30.4	92.46	18.78	428.26	123.14	33.72	376.04
26	25	35.02	9.9	-28.9	26.5	32.36	21.41	180.53	46.04	4.49	207.97
27	26	29.38	14	-25.8	-54.5	122.49	9.71	681.08	144.03	22.49	665.72

Figure 3.14 Example of a fused-fibre CSV exported by the tool for one sub-volume.

3.3.2 Validation of the fibre extraction

The fibres extracted by the tool of Section 3.3.1 were checked in two ways before their measurements were carried forward.

First, before the detections from the three directions are fused, the tool registers the three orthogonal reslices onto the Z reference and reports how well their fibre foregrounds overlap. Since the reslices are three views of one and the same crop (Section 3.2.2), a correct registration should bring those foregrounds into close coincidence, so the reported overlap is a check that the alignment has succeeded. The X and Y directions are each aligned to Z and their binary overlap is given: for the first sub-volume, for example, these overlaps were 0.79 and 0.81. Across the ten sub-volumes they lay between 0.38 and 0.84 (Table 3.4), which confirms that in every case the three reslices were correctly registered as the same physical volume, so that fusion combined aligned data rather than views that had drifted out of register. This checks the registration; the fibres themselves are checked by the overlay described next.

Table 3.4 Binary overlap of the X and Y reslices with the Z reference, for each sub-volume.

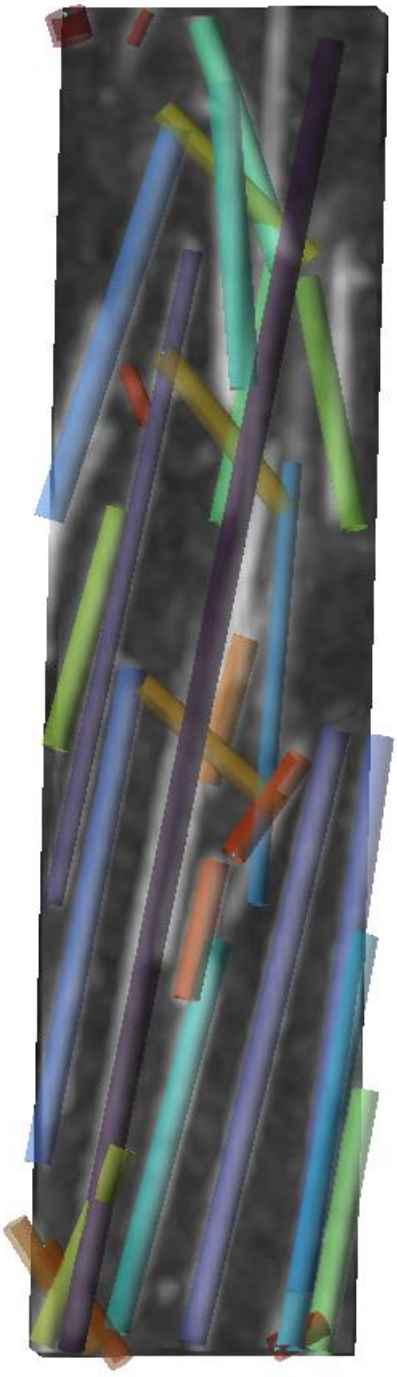
Sub-volume	Overlap, X to Z	Overlap, Y to Z

1	0.79	0.81
2	0.83	0.79
3	0.44	0.38
4	0.82	0.78
5	0.81	0.81
6	0.83	0.84
7	0.82	0.81
8	0.81	0.78
9	0.68	0.73
10	0.59	0.66

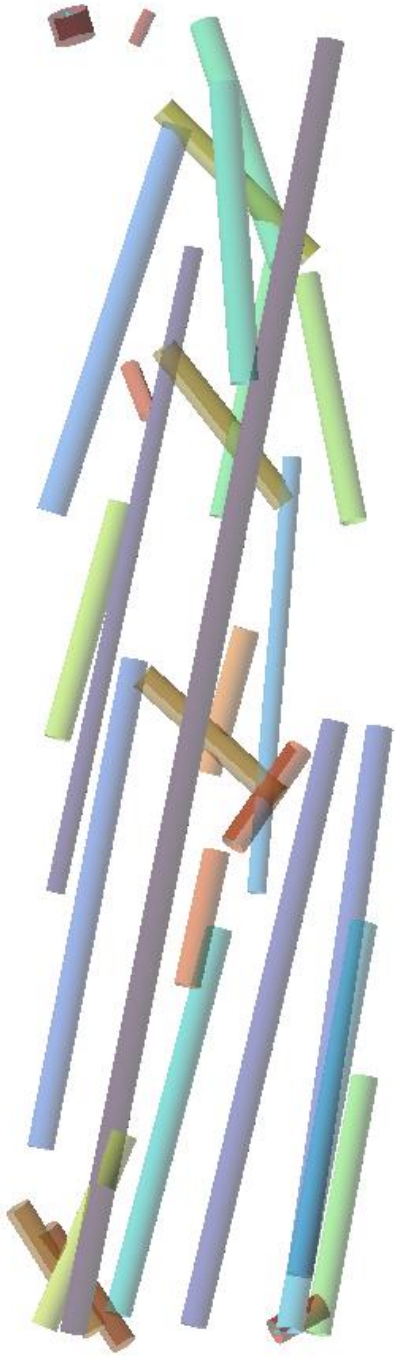
Three sub-volumes gave lower overlaps. Number 3 is the clear outlier, where a strong alignment of the fibres along one axis leaves the reslice in that direction with little structure to register against. Numbers 9 and 10 sit a little below the rest; sub-volume 10 has one of the lowest fibre counts (Table 3.5), so its small fibre foreground makes the overlap more sensitive to slight misregistration. In each case the fibres themselves were confirmed by the overlay check below, which does not depend on the registration score, so these sub-volumes were retained.

Second, the extracted fibres were overlaid back onto the raw greyscale scan and inspected. This was done with a short Python script (listed in Appendix 3) that reads the fused-fibre export and draws, in the napari viewer, one translucent cylinder for every fibre, built from that fibre's measured length, diameter and orientation, on top of the raw stack (Figure 3.15). Because the cylinders come from the measured geometry rather than from the raw detections, the overlay tests the final fibres, the ones carried into the statistics, against the image they are meant to represent. The raw stack loaded for this must be the same z-direction reference stack the tool used, so that the fibre coordinates and the image sit in one frame.

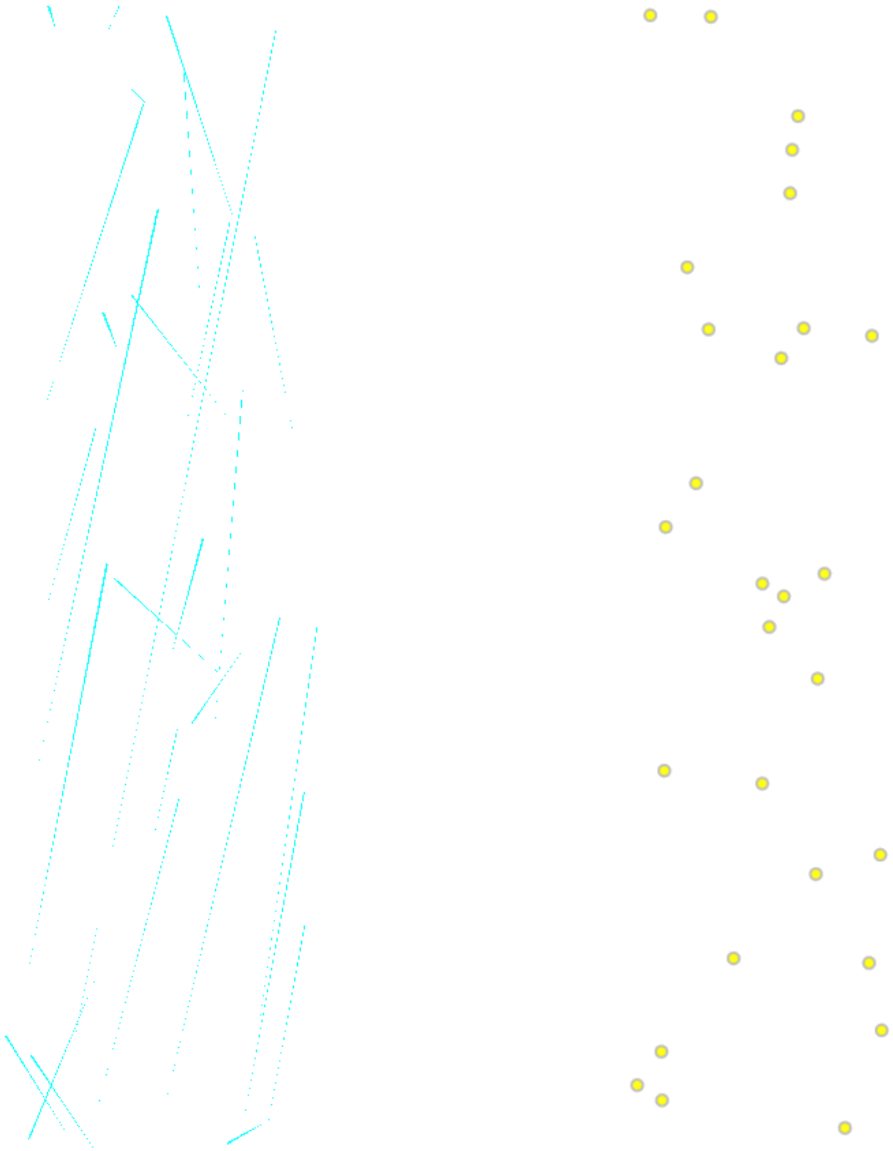
The overlay was examined in three dimensions, rotating the volume so that the fit could be judged from more than one angle. Almost no cylinders were drawn where no fibre was present, so the detected fibres are real, and only a few fibres visible in the raw image were left without a cylinder (i.e., the fiber was not detected).



a)



b)



c) d)

Figure 3.15 napari overlay of the extracted fibres for one sub-volume: a) The detected fibres, drawn as cylinders, overlaid on the raw greyscale stack; each cylinder sits on a real fibre in the image, b) The same fibre cylinders alone, with the greyscale hidden, showing the recovered population and its orientation, c) The fibre centre-lines and d) The fibre centroids.

The few fibres that are missed are the main limitation of the extraction. They tend to be the faint or thin ones that do not clear the detection sensitivity, the short ones that span too few slices to meet the minimum track length, or fibres clipped by the edge of the sub-volume so that only a stub is present. Because so few are missed, and the detected fibres are real, the effect on the measured statistics is small; it falls on the fibre counts more than on the shape of the fitted distributions, and only becomes a bias if the missed fibres are predominantly of one kind. The detection rate was not quantified here. A reliable figure would require counting detected against visible fibres on two-dimensional slices at full

resolution. This count would use the fused detections from all three directions rather than those of any single direction. Establishing it, and with it the completeness of the fibre population, is left for future work.

3.3.3 Statistical distribution fitting

The per-fibre measurements were pooled across the ten sub-volumes to give a combined sample of 307 fibres, distributed between the sub-volumes as listed in Table 3.5. Each geometric quantity, the fibre length, the diameter, the elevation angle α and the azimuth angle β, was treated as a random variable and represented by a probability distribution, so that the fibre population could be regenerated from a small number of parameters rather than stored as a list of individual fibres.

Table 3.5 Number of fibres detected in each sub-volume.

Sub-volume	Fibres detected
1	28
2	30
3	33
4	24
5	41
6	31
7	34
8	29
9	32
10	25
Total	307

Candidate distributions were chosen to match the character of each quantity. The fibre length is positive and right-skewed and was fitted with the lognormal, gamma and Weibull distributions. The two orientation angles are centred near zero and approximately symmetric and were each fitted with the normal, Laplace and generalised normal distributions. The density functions of these candidates are given in Table 3.6.

Table 3.6 Candidate distributions and their probability density functions. Γ denotes the gamma function.

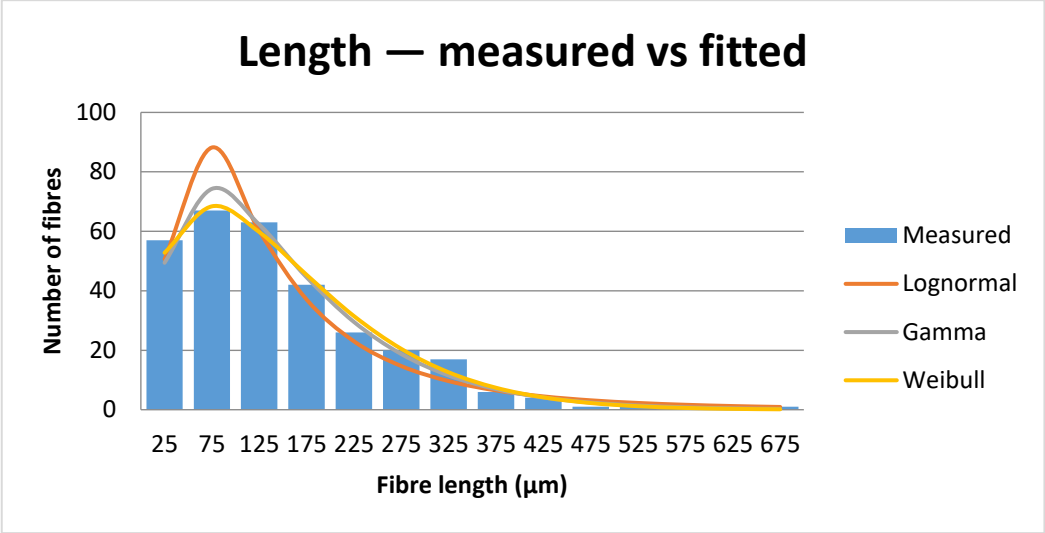
Quantity	Distribution	Density function f(x)	Para.
Length	Lognormal	$f(x) = 1/\left(x\sigma\sqrt{(2\pi)}\right) \cdot exp[-(lnx-\mu)^2/(2\sigma^2)], x > 0$	μ, σ
Length	Gamma	$f(x) = 1/(\Gamma(k)\theta^k) \cdot x^{(k-1)} \cdot exp(-x/\theta), x > 0$	k, θ
Length	Weibull	$f(x) = (k/\lambda)(x/\lambda)^{(k-1)} \cdot exp[-(x/\lambda)^k], x \geq 0$	k, λ
α, β	Normal	$f(x) = 1/\left(\sigma\sqrt{(2\pi)}\right) \cdot exp[-(x-\mu)^2/(2\sigma^2)]$	μ, σ
α, β	Laplace	$f(x) = 1/(2b) \cdot exp(-\lvert x-\mu\rvert/b)$	x – μ
α, β	Generalised normal	$f(x) = \beta/\left(2\alpha\Gamma(1/\beta)\right) \cdot \exp\left[-(\lvert x-\mu\rvert/\alpha)^\beta\right]$	x – μ

Each candidate was fitted to the pooled sample by the method of maximum likelihood. For a distribution with parameter set θ and density f(x; θ), the log-likelihood of the sample $\{x_1, \ldots, x_n\}$ is

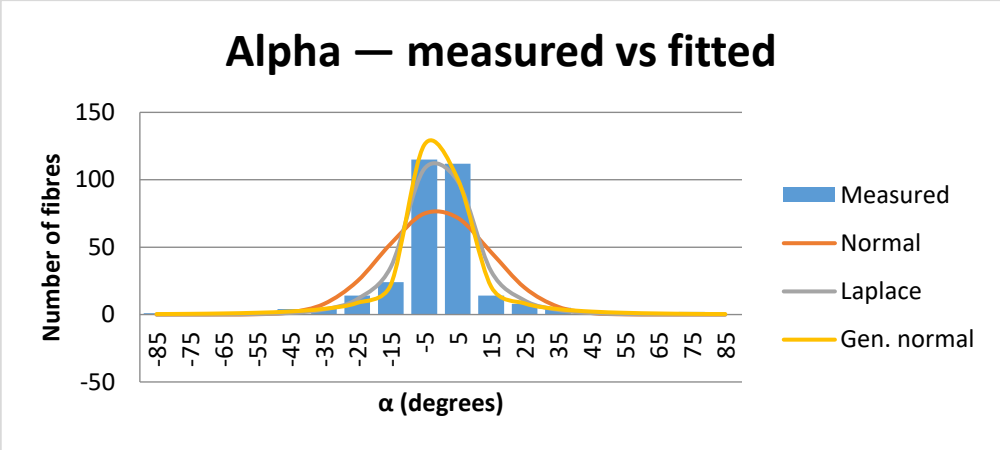
$$\ell(\theta) = \Sigma_{i=1}^{n} lnf(x_i; \theta) \qquad (3.3)$$

and the fitted parameters $\hat{\theta}$ are those that maximise $\ell(\theta)$. For the normal, Laplace and lognormal distributions the maximiser is available in closed form; for the gamma, Weibull and generalised normal distributions it was obtained numerically. The competing fits for each quantity were then compared using the Pearson chi-square test of Section 3.3.4, and the distribution with the highest p-value was adopted.

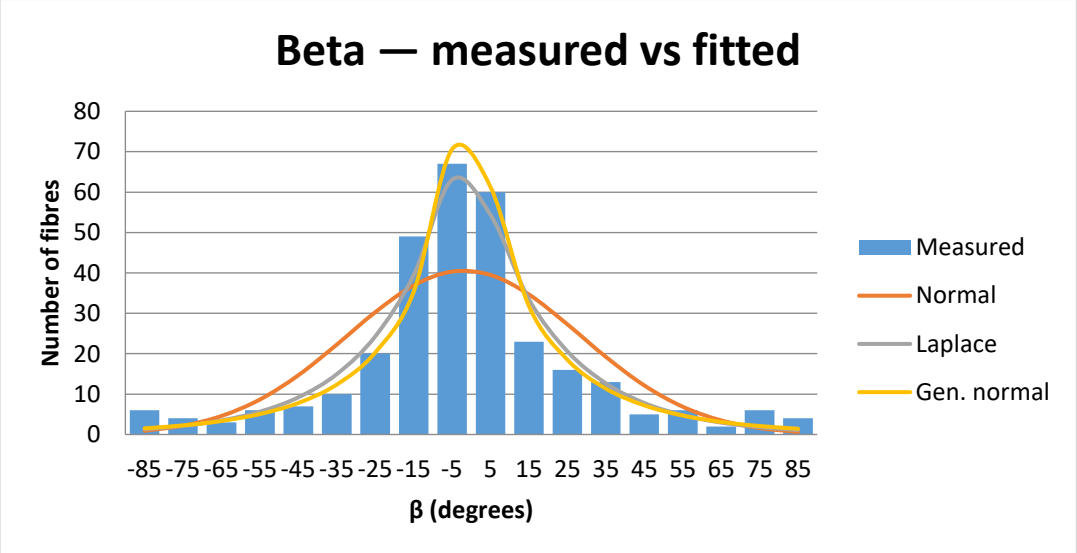
On this basis the fibre length was described by a Weibull distribution, the elevation angle α by a generalised normal distribution, and the azimuth angle β by a Laplace distribution. The measured histograms and the fitted densities are shown in Figure 3.16. The fitted parameter values for the adopted distributions, together with the goodness-of-fit statistics for every candidate, are reported in Chapter 4 (Tables 4.2 and 4.3).


Length — measured vs fitted
Number of fibres
100
80
60
40
20
0
25 75 125 175 225 275 325 375 425 475 525 575 625 675
Fibre length (µm)
Measured
Lognormal
Gamma
Weibull

a)


Alpha — measured vs fitted
Number of fibres
150
100
50
0
-50
-85 -75 -65 -55 -45 -35 -25 -15 -5 5 15 25 35 45 55 65 75 85
α (degrees)
Measured
Normal
Laplace
Gen. normal

b)


Beta — measured vs fitted
Number of fibres
80
70
60
50
40
30
20
10
0
-85 -75 -65 -55 -45 -35 -25 -15 -5 5 15 25 35 45 55 65 75 85
β (degrees)
Measured
Normal
Laplace
Gen. normal

c)

Figure 3.16 Distribution histograms of length and orientation angles of the fibres: a) Fibre length: measured histogram with the fitted lognormal, gamma and Weibull densities, b) Elevation angle α: measured histogram with the fitted normal, Laplace and generalised generalised normal densities and c) Azimuth angle β: measured histogram with the fitted normal, Laplace and generalised normal densities.

The diameter was treated separately. It is obtained as twice the inscribed radius, which on the 3.5 µm voxel grid can take only a discrete set of values. Since the voxel size is a large fraction of the fibre diameter, the measured values fell onto nine distinct diameters rather than a continuous range. A continuous density therefore has no physical meaning for this quantity, and the diameter was represented directly by its nine measured values and their measured relative frequencies, shown in Figure 3.19.

Most fibres fall at the central values, with 14 µm the most common, close to the nominal fibre diameter of 16 µm. The spread across the nine values is a measurement effect rather than genuine variation in fibre thickness: the inscribed radius can take only the discrete steps the distance transform allows on a 3.5 µm grid, and the largest values arise where closely spaced fibres are not fully separated, so the inscribed circle spans more than one fibre. The true fibre diameter is therefore close to the nominal value, and the apparent range reflects the resolution limit of the scan.

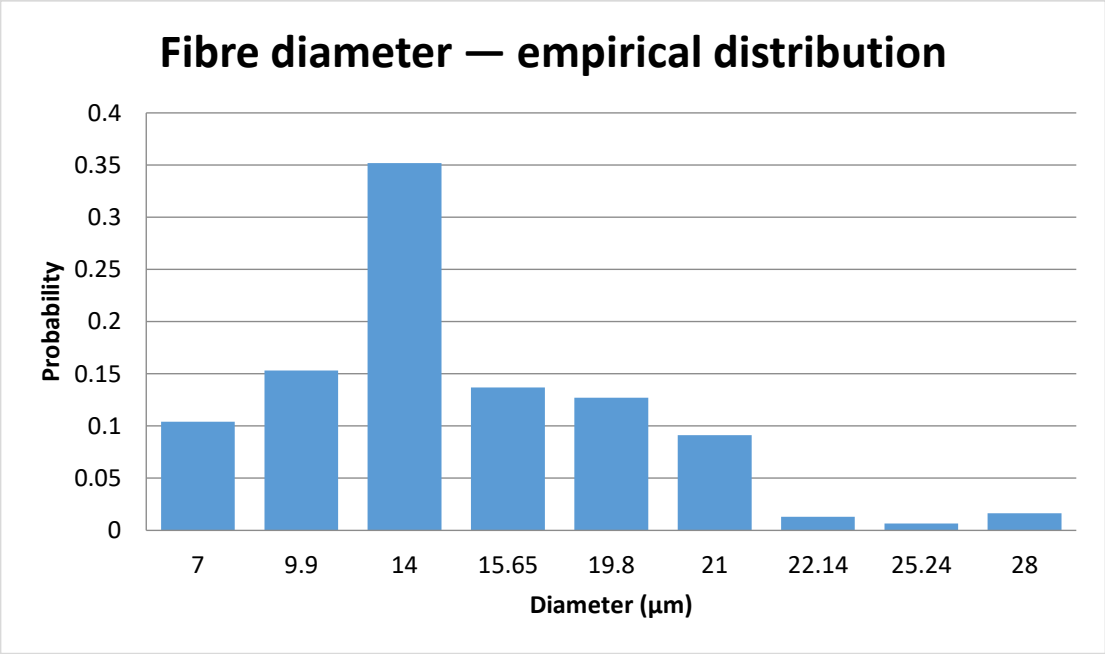


Figure 3.17 Fibre diameter: empirical distribution over the nine measured values.

The fitted parameters of the adopted distributions, together with the goodness-of-fit statistics, are reported in Chapter 4, and the adopted distributions form the input to the representative volume element of Section 3.4.

3.3.4 Goodness-of-fit assessment

Each candidate fit was assessed numerically with the Pearson chi-square test and graphically with a quantile-quantile plot.

For the chi-square test the range of the quantity was divided into m bins. Writing O_i for the number of fibres measured in bin i and E_i for the number expected under the fitted distribution, the test statistic is

$$\chi^2 = \Sigma_{i=1}{}^{m}(O_i - E_i)^2/E_i \qquad (3.4)$$

where the expected count is the sample size multiplied by the probability the fitted distribution places in the bin,

$$E_i = n[F(u_i) - F(l_i)] \qquad (3.5)$$

with F the fitted cumulative distribution function and l_i and u_i the lower and upper edges of bin i. The statistic was referred to a chi-square distribution with

$$\nu = m - 1 - k \qquad (3.6)$$

degrees of freedom, where k is the number of parameters estimated from the sample, and the significance was taken as

$$p = P(\chi^2{}_{\nu} \geq \chi^2) \qquad (3.7)$$

Towards the tails, where few fibres fall, adjacent bins were merged until every expected count E_i was at least five, the condition under which the chi-square approximation is reliable. The histograms in Section 3.3.3 use equal-width bins for clarity of presentation, whereas the test uses these merged bins. For each quantity the candidates were ranked by p, the distribution with the highest value was adopted, and a fit was regarded as acceptable when p exceeded 0.05.

The quantile-quantile plot provided an independent, graphical check. The measured values were sorted into ascending order $x_{(1)} \leq \ldots \leq x_{(n)}$, and each was assigned the plotting position

$$p_i = (i - 0.5)/n \qquad (3.8)$$

The ordered value $x_{(i)}$ was then plotted against the corresponding quantile of the fitted distribution, $F^{-1}(p_i)$. A distribution in agreement with the data falls on the line y = x, and a systematic departure, most commonly in the tails, appears as a curve away from that line. The plots for the three adopted fits are shown in Figure 3.18.

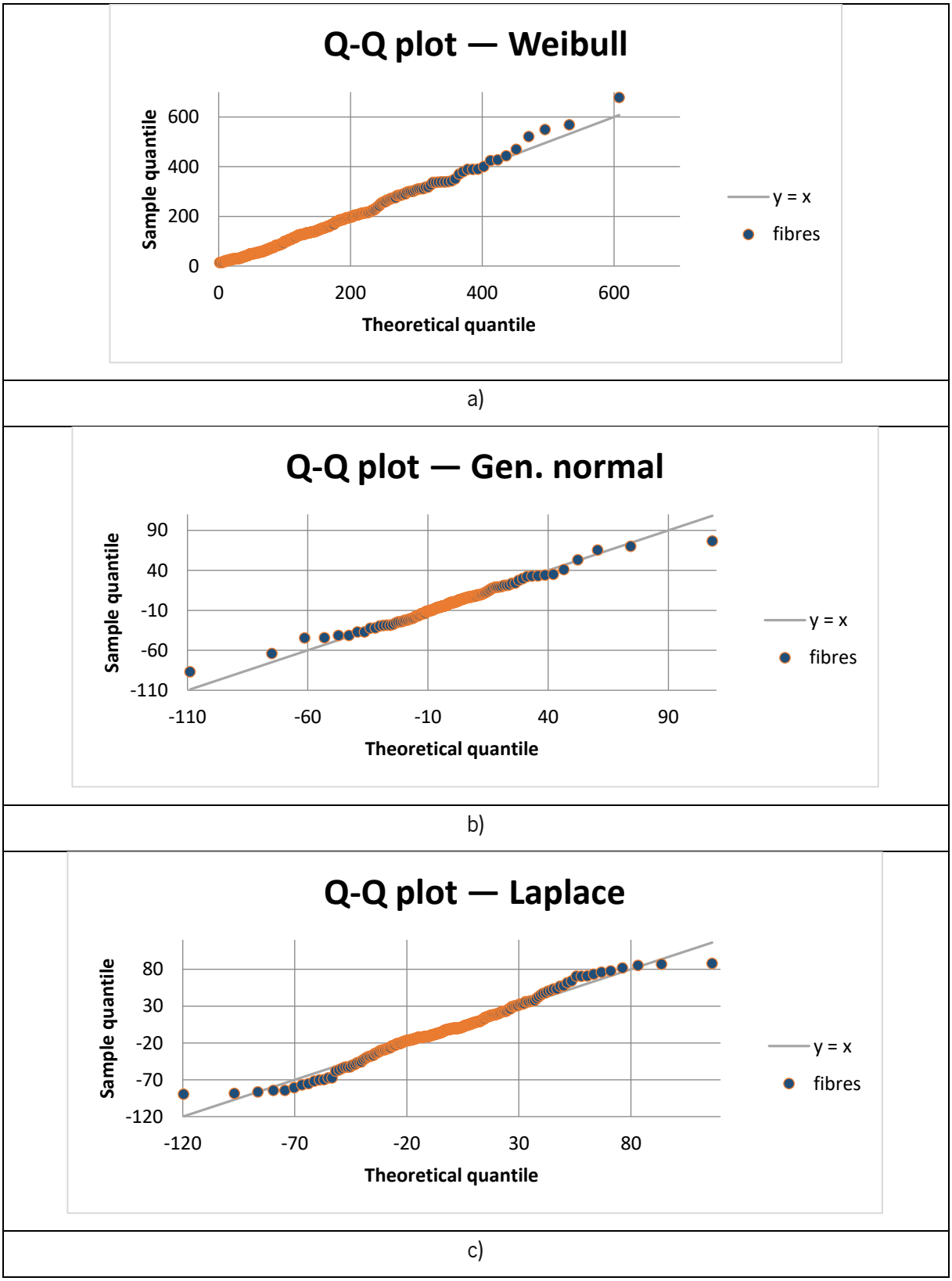


Figure 3.18 Quantile-quantile plotting of length and orientation angles of the fibres: a) Q-Q plot for the Weibull fit to the fibre length, b) Q-Q plot for the generalised normal fit to the elevation angle α and c) Q-Q plot for the Laplace fit to the azimuth angle β.

The Weibull fit for the length, the generalised normal fit for the elevation angle and the Laplace fit for the azimuth angle were each accepted on both criteria and carried forward to the representative volume element. The chi-square statistics, degrees of freedom, p-values and fitted parameters for every candidate are reported in Chapter 4.

The diameter is not tested in this way. Because it takes only nine discrete values, its distribution is the empirical set of relative frequencies given in Section 3.3.3, and no continuous fit is involved. The collapse of the measured diameters onto these few values is a consequence of the voxel resolution rather than a property of the fibres, and it sets the finest scale at which the diameter can be resolved from this scan. It leaves the length and orientation statistics unaffected, since those span many voxels and are well resolved, but any diameter-dependent result should be read with this resolution limit in mind.

3.4 Representative volume element generation and thermal analysis

The fitted distributions of Section 3.3 give a compact statistical description of the fibre architecture, and that description is the input to generate the representative volume element (RVE), that will be later used to perform finite element simulations. Rather than reproducing the 307 measured fibres, the RVE is filled with fibres whose length, orientation and diameter are drawn at random from the adopted distributions, so the generated volume reproduces the measured statistics while remaining small enough to keep low computational efforts. The whole workflow, from generating the fibres to building the finite element model, cooling it and reading off the thermal response, is carried out by a single Abaqus/Python script. Keeping it in one file makes it reproducible: there are no intermediate data files to manage, the random sampling uses only the Python standard library so it runs in any Abaqus installation without numpy or scipy, and every quantity a user might change for a different material, sample or volume fraction is collected in one block at the top. The script is run either in batch, with abaqus cae noGUI=<file_name>.py, or from within Abaqus/CAE through File then Run Script. It produces a conforming RVE of a basalt-fibre-reinforced PA11 composite, cools it from RT to the liquid-hydrogen target, and reports the directional coefficient of thermal expansion and the residual thermal stresses.

3.4.1 Monte Carlo generation of the fibre architecture

The generation is a Monte Carlo procedure. Each fibre is an independent random draw from the fitted distributions, and the fibres are then placed one at a time into the box until the target volume fraction is reached. One run with a fixed random seed is one realisation of the microstructure, in the same way that

the scanned sub-volume is one realisation of the real material. This is the heart of the method, so it is described before the finite element model.

Each fibre carries four random quantities, and each is drawn from the distribution adopted for it in Section 3.3. The length comes from the Weibull distribution (shape k = 1.412, scale λ = 162.9 μm), the out-of-plane angle α from the generalised normal (location μ = −0.3°, scale 0.834, shape 0.439), the in-plane angle β from the Laplace (location μ = −1.7°, scale b = 20.6°), and the diameter from the empirical table of nine measured values. Because the standard library has no statistical distribution functions, each is sampled directly. The length uses inverse-transform sampling, in which a uniform random number u on the interval from zero to one is passed through the inverse of the Weibull cumulative distribution,

$$x = \lambda[-ln(1-u)]^{(1/k)} \tag{3.9}$$

which is exact for the Weibull. The in-plane angle uses the same idea with the inverse of the Laplace cumulative distribution,

$$x = \mu - b \cdot sgn(u) \cdot ln(1-2|u|), u \in (-½, ½) \tag{3.10}$$

again exact. The out-of-plane angle cannot be inverted so simply, so the generalised normal is sampled through its relationship to the gamma distribution: a gamma variate with shape $1/\beta$ is raised to the power $1/\beta$, scaled, and given a random sign, which reproduces the generalised normal density exactly. The three samplers are the marked functions in the script:

```
def _sample_weibull(rng, k, lam, lo, hi):
    u = rng.random()
    x = lam * (-math.log(1.0 - u)) ** (1.0 / k) # inverse Weibull CDF

def _sample_laplace(rng, loc, scale, lo, hi):
    u = rng.random() - 0.5
    x = loc - scale * math.copysign(1.0, u) * math.log(1.0 - 2.0 * abs(u))

def _sample_gennorm(rng, beta, loc, scale, lo, hi):
    t = rng.gammavariate(1.0 / beta, 1.0)
    mag = scale * (t ** (1.0 / beta))
    x = loc + (mag if rng.random() < 0.5 else -mag)
```

Each draw is wrapped in a loop that rejects and redraws any value falling outside the measured range, so the length stays within its measured minimum and maximum and the angles stay within ±90 degrees.

This truncation keeps the generated fibres inside the range the scan actually saw, rather than letting the tails of a fitted curve produce unphysical values. The diameter is handled by its empirical table: a uniform number is compared against the running cumulative probabilities of the nine measured diameters, and the matching diameter is returned, so the generated diameters take exactly the nine values the scan resolved, in their measured proportions.

The two angles are turned into a unit direction using the same convention as the extraction in Section 3.3.1, with the fibres predominantly along the reconstructed z axis and the x-z plane as reference,

$$d = (cos\alpha \cdot sin\beta, sin\alpha, cos\alpha \cdot cos\beta) \qquad (3.11)$$

The fibres are then placed by Random Sequential Addition. A slightly larger set of fibres than needed is drawn first, since some fibre length is lost when a fibre crosses a box face, and the set is sorted longest first, because the long fibres are the hardest to fit and packing them before the short ones improves the achievable volume fraction. Each fibre is placed by trying random centres inside the box, up to a set number of attempts. For every trial the fibre segment is clipped to the box by the Liang-Barsky algorithm, so that only the portion lying inside the RVE is kept and only that portion counts toward the volume fraction, which is the correct accounting for a fibre that runs out through a face. A trial is rejected if the in-box length would be shorter than one diameter, which discards meaningless stubs, and it is rejected if the new fibre would touch any fibre already placed. The contact check is the governing geometric test: the shortest distance between the new fibre axis and each existing fibre axis is computed, and the fibre is accepted only if that distance exceeds the sum of the two radii plus a small surface-to-surface gap,

```
for (pa, pb, pr) in placed_segs:
    if _seg_seg_dist(a, b, pa, pb) < (r + pr + MIN_GAP_UM):
        ok = False # too close to an existing fibre: reject this position break
```

Consequently, two fibres cannot intersect (as in reality) and a minimum matrix ligament is preserved between them, which the mesh later needs to avoid generating close to zero volume elements in-between neighbouring fibres. Fibres are added in this way until the placed in-box volume reaches the target fraction of the box volume, with a top-up loop that continues drawing fresh fibres if the sorted set runs out, and a jamming guard that stops after a run of consecutive failures so the script cannot loop forever when the box is too full to accept more. The achieved volume fraction is reported alongside the target, because in a thin box packed with the thicker fibres the two do not need to coincide.

Reproducibility is deliberate and rests on the random seed. All sampling and all placement draw from a single generator seeded by one integer, so the same seed reproduces the identical RVE every time, and

a different seed produces a different but statistically equivalent realisation. Everything that defines the microstructure sits in the user-input block at the top of the file. The distribution-fitting results from Section 3.3 enter there directly: the empirical diameter table is a short list of value and probability pairs, and the Weibull, generalised normal and Laplace parameters are the adopted fits, each with its truncation range. To model a different sample, a user replaces those numbers with that sample's fitted parameters and its measured diameter list, and runs the script again, without touching anything below the input block. The target volume fraction is a single entry in the same block, so the planned sweep to other fractions is a one-line change. This is what makes the pipeline reusable for any short-fibre system: the geometry, the statistics and the volume fraction are all inputs, not code. The output model should seem like Figure 3.19.

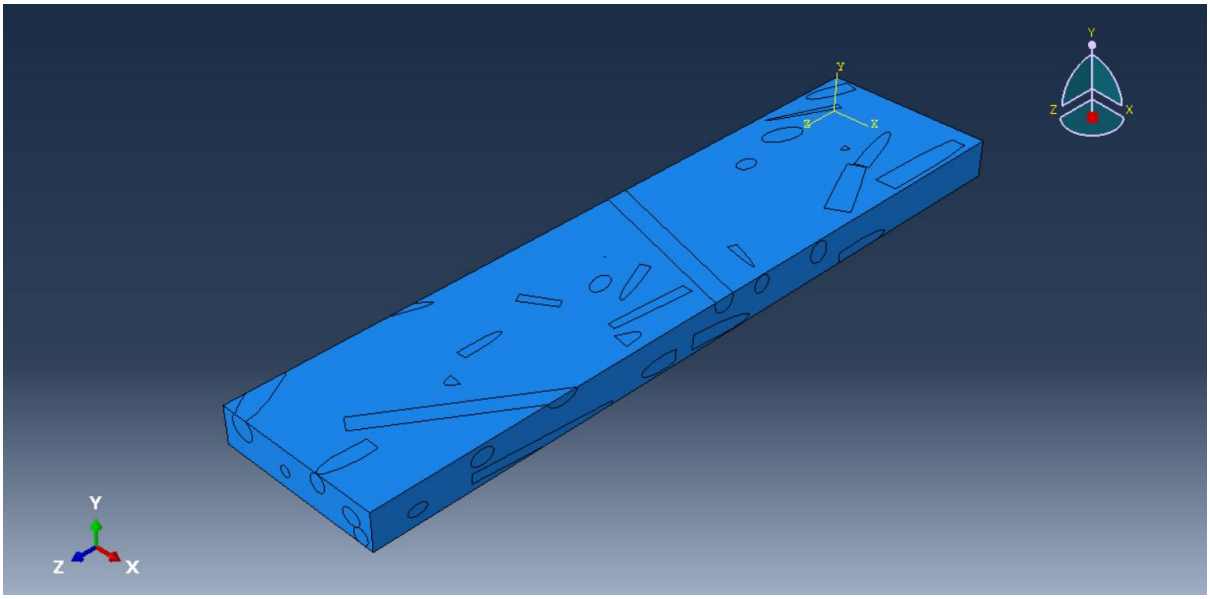


Figure 3.19 One realisation of the generated RVE, of size 161.00 × 35.00 × 679.01 μm (one CT sub-volume), at a fibre volume fraction of 20%, showing the basalt fibres within the PA11 matrix and the flat outer faces produced by the trim.

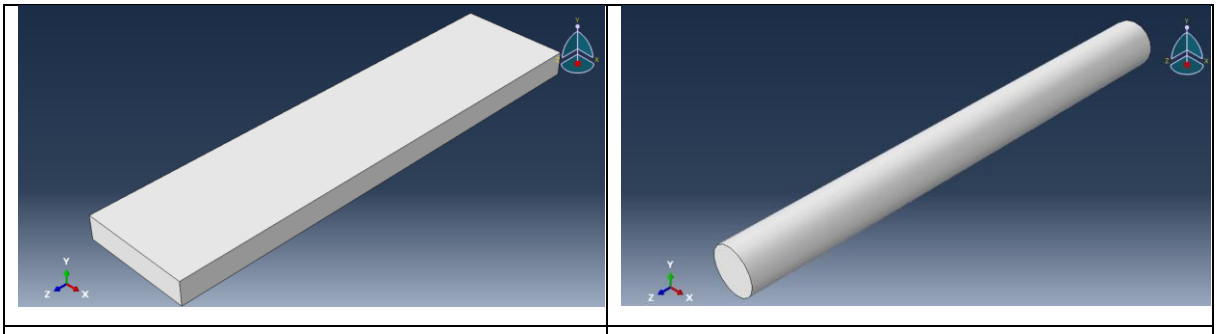
For the realisation carried into the analysis that follows, generated with a fixed seed for exact reproducibility, the Random Sequential Addition placed 54 non-intersecting fibres in the sub-volume-sized box, with its long axis along z, and reached a fibre volume fraction of 20.1%, in close agreement with the 20% target. The generated architecture is shown in Figure 3.19.

3.4.2 Finite element model

Following are the explanations of the finite element model module by module.

Part: Two kinds of solid are created. The matrix is a single rectangular block the size of one CT sub-volume, 161.00 × 35.00 × 679.01 μm, sketched and extruded to the box dimensions; see Figure 3.20. This size is used so that the model represents a real measured region of the material while staying small

enough to mesh and solve at reasonable computational cost. Each fibre is a cylinder, sketched as a circle of its own sampled radius and extruded to its length, then rotated to the direction of equation (3.11) and translated to its placed position. Where a fibre was clipped by a box face, its cylinder is extended a short margin beyond that face before the trimming stage, so the later Boolean operation cuts it cleanly flush with the surface rather than leaving a sliver. At this stage the matrix block and the fibre cylinders occupy the same space, which the assembly stage resolves later.



a) b)

Figure 3.20 The two-part primitives created before merging: the matrix box and b) a representative fibre cylinder.

Property: A material must be created for the fibres and the matrix. Both are temperature dependent, defined by the tables in Section 3.4.3. Each is modelled as isotropic linear elastic, by definition an elasticity table of Young's modulus and Poisson's ratio against temperature, and an isotropic thermal expansion table against temperature. It is worth noting that this approeach is handled in code rather than by hand. The expansion values entered are the physical, tangent coefficients of thermal expansion, but Abaqus by default interprets an expansion table as secant values measured from a stress-free reference temperature. The script therefore converts them. It integrates the tangent coefficient over temperature to obtain the thermal strain, referencing the strain to the RT stress-free point, and then divides by the temperature difference to return the secant coefficient at each table temperature,

$$\bar{\alpha}(T) = [\varepsilon(T) - \varepsilon(\theta_0)] / (T - \theta_0), \varepsilon(T) = \int (\theta_0 \to T)\, \alpha_tan(T')\, dT' \qquad (3.12)$$

with the integral evaluated by the trapezoidal rule between table points. Without this conversion the imposed expansion would be wrong by the difference between the tangent and secant forms, which over a 273 kelvin cooldown is not small. Each material is then wrapped in a solid section and assigned to its region.

Assembly: This is where the overlapping solids become a single conforming body, and it is the most delicate part of the script. The matrix block and all the fibre cylinders are combined by a Boolean merge with retained intersection boundaries. The merge hollows the matrix exactly where the fibres sit and fuses the matrix and the fibres into one part whose fibre and matrix regions share a common interface, so the

two phases meet on matching surfaces rather than as separate overlapping bodies. The protruding fibre ends are then trimmed flat: a large block with an inner box-shaped cavity is built and subtracted from the merged part, cutting everything that lies outside the RVE and leaving all six outer faces flat, which the boundary conditions require. After the merge the script has to tell the fibre cells apart from the matrix cell, since the merge does not label them, and it does this geometrically by selecting the cells that lie within a bounding cylinder around each original fibre axis and collecting the remainder as matrix. These become the fibre and matrix sets that carry the section assignments. The merge and trim are known to be the fragile step in any conforming-RVE script, and the script notes the reliable remedies if it fails, in order: increase the minimum gap slightly, lower the target volume fraction slightly, or switch the trim off. The model is saved to file even when a later step fails, so a failed run is still inspectable.

Step: The analysis is a single static step representing the cooldown from the RT stress-free state to the liquid-hydrogen target. Geometric non-linearity is left off because the analysis is confined to small strains: the cooldown produces directional strains of only a few percent, with the largest being about 2 percent through the thickness, and displacements that are very small relative to the model size, so a geometrically linear small-strain formulation is appropriate and the added cost of a large-displacement solution is not warranted. The step uses automatic time incrementation with a sensible initial increment and minimum and maximum bounds, so the solver can take small steps where the sharply temperature-dependent matrix properties demand it and larger steps elsewhere.

Interaction: No contact or tie interaction is defined, and this is deliberate rather than an omission. Because the merge produced one conforming part, the fibres and matrix already share nodes along their interface, so displacement is continuous across it and the two phases are perfectly bonded by construction.

Load and boundary conditions: The thermal load is a uniform predefined temperature field applied to the whole model, set to 293 K in the initial state and lowered to 20 K in the cooldown step, so every point cools by the same 273 K and the strains that develop are the composite's thermal response. The 293 K reference is the stress-free state, taken as RT, and 20 K is the liquid-hydrogen storage temperature. The mechanical boundary conditions are the minimum ones required to avoid rigid body motion while still allowing for freely contraction/expansion due to the thermal cool-down without any over-constrains, avoiding the so-called Poisson stresses. Thus, the three faces at the origin are each held against motion normal to themselves, so the face at x equal to zero cannot move in x, the face at y equal to zero cannot move in y, and the face at z equal to zero cannot move in z, while the three opposite faces are

unconstrained, as shown in Figure 3.21. The displacement of the free faces then measures the thermal strain.

```
model.DisplacementBC(name='ROLLER_X0', createStepName='Initial', region=a.sets['FIX_X0'], u1=0.0)
model.DisplacementBC(name='ROLLER_Y0', createStepName='Initial', region=a.sets['FIX_Y0'], u2=0.0)
model.DisplacementBC(name='ROLLER_Z0', createStepName='Initial', region=a.sets['FIX_Z0'], u3=0.0)
```

Periodic boundary conditions are necessary to enforce the relative displacement between any two matching points on opposite boundaries to be constant. This way, even if the RVE is relatively small, it allows to simulate it as if the material was infinite, allowing to later obtain the material properties with high accuracy. Unfortunately, to implement this it is required matching pairs of nodes on opposite faces, which a free tetrahedral mesh (as used here due to the complex geometry) does not produce, and enforcing them would need either a structured mesh or a large set of constraint equations. The applied boundary conditions are enough to give a sound estimate of the free thermal contraction and can also be quite accurate if the RVE is quite large and contains several fibers. In any case, imposing genuine periodic conditions is left as future work.

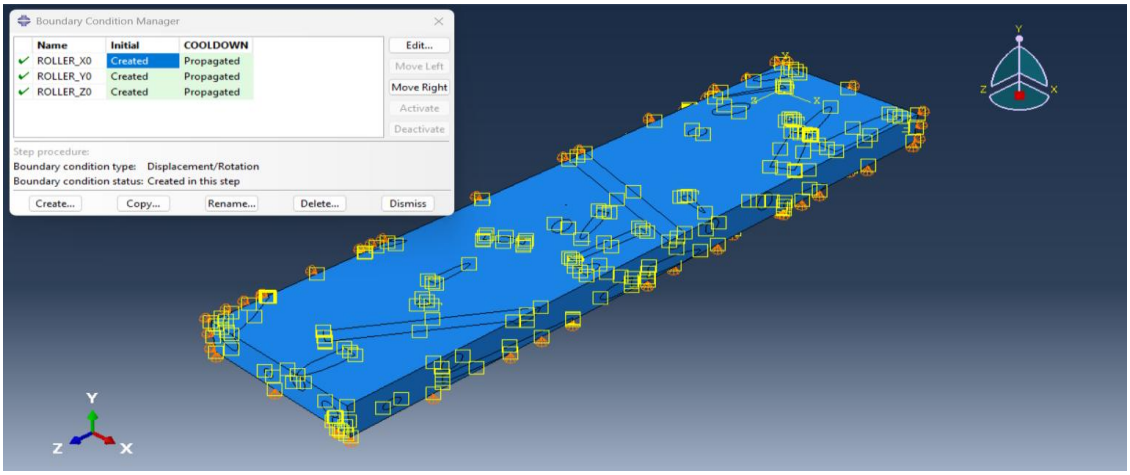


Figure 3.21 The mechanical boundary conditions on the RVE, the three boundary conditions named as ROLLER_X0, Y0 and Z0 holding the faces at the origin against motion normal to each, with the three opposite faces left free.

Mesh: The conforming part is meshed with free tetrahedrons, which is what allows an arbitrary fibre arrangement to be meshed unless complex partitioning is carried out. The elements are ten-node quadratic tetrahedrons by default, which represent the curved fibre surfaces and the strain fields better than linear elements. A single target element size, of the order of the fibre diameter, is seeded over the whole part, fine enough to resolve the matrix ligaments between fibres, as shown in Figure 3.22. For the realisation analysed here, this seed size was 6 micrometres, which produced a conforming mesh of 247,520 quadratic tetrahedral (C3D10) elements and 350,297 nodes.

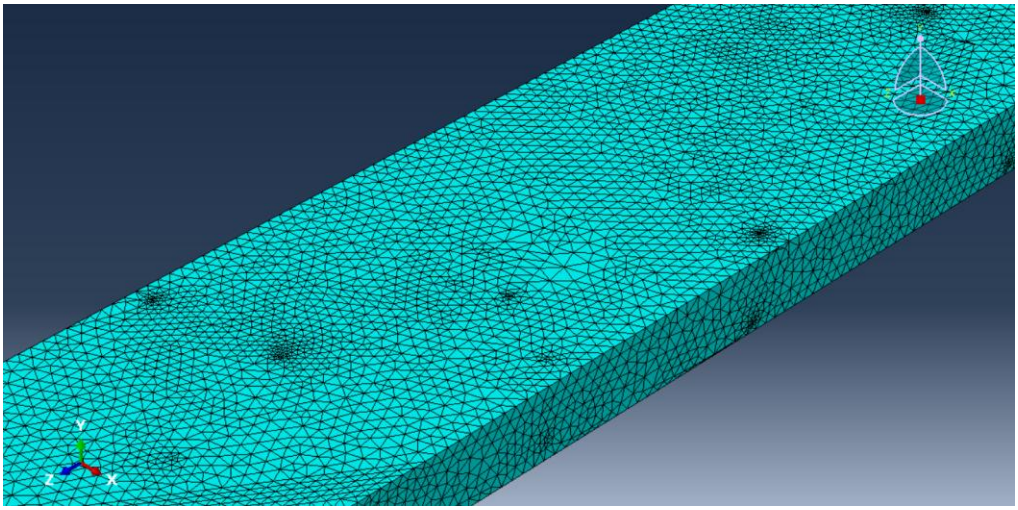


Figure 3.22 The RVE meshed with quadratic tetrahedral (C3D10) elements, the mesh conforming across the fibre and matrix.

3.4.3 Material properties

The elastic and thermal properties used for the two phases are given in Table 3.7. Only the RT values are taken from the literature. The basalt fibre is anchored at RT to a modulus of 89 GPa, a Poisson's ratio of 0.26 and an axial coefficient of thermal expansion of 5.5×10^{-6} per kelvin [54], and the PA11 matrix to a modulus of about 1.3 GPa, a Poisson's ratio of about 0.40 and a coefficient of thermal expansion of about 110×10^{-6}/K [55]. Every row below RT is an engineering estimate, because no cryogenic property table was available for either material. They follow the expected trends, the polymer stiffening markedly and both materials contracting less as they cool, but they are placeholders and are marked as such in the script, to be replaced with measured or datasheet values when these are available.

Table 3.7 Temperature-dependent properties used in the thermal model. RT rows are sourced; all rows below RT are engineering estimates. The coefficient of thermal expansion is given as the physical (tangent) value; the script converts it to the secant form used in the model, with the reference temperature set to the RT stress-free state of 293 K.

Table 3.7 Material Properties.

Material	T (K)	E (MPa)	ν	Tangent CTE (K^{-1})
Basalt fibre	293	89000	0.26	5.5×10^{-6}
	200	90000	0.26	4.6×10^{-6}
	100	92000	0.26	3.2×10^{-6}
	77	92500	0.26	2.7×10^{-6}

	20	93000	0.26	1.0×10^{-6}
PA11 matrix	293	1300	0.40	110×10^{-6}
	200	2600	0.39	80×10^{-6}
	100	3900	0.37	45×10^{-6}
	77	4300	0.36	35×10^{-6}
	20	4800	0.35	12×10^{-6}

3.4.4 Job and extraction of the thermal response

By default, the script builds the model and writes the input file without solving, so it can be checked first and then run the job manually; otherwise, solving and post-processing can be enabled by the RUN_JOB flag in the input block.

The post-processing reads the final frame of the cooldown and reduces it to the quantities of interest. The directional thermal strain is obtained by averaging the displacement of each free face over its nodes and dividing by the corresponding box length, so the mean outward movement of a face divided by the length of the RVE in that direction is the engineering strain in that direction,

```
def face_strain(setname, comp, length):
    ns = odb.rootAssembly.nodeSets[setname]
    vals = [v.data[comp] for v in U.getSubset(region=ns).values]
    return (sum(vals) / len(vals)) / length
```

Writing ū_face for the mean displacement of a free face and L_dir for the length of the RVE in the same direction, the directional thermal strain is

$$\varepsilon_{dir} = \bar{u}_{face} / L_{dir} \tag{3.13}$$

and the directional coefficient of thermal expansion is the secant value over the whole cooldown, this strain divided by the temperature change from 293 K to 20 K, ΔT = −273 K,

$$\alpha_{dir} = \varepsilon_{dir} / \Delta T \tag{3.14}$$

evaluated separately in x, y and z, which gives the anisotropy of the composite's expansion directly. The three strains and the three coefficients are written to a short results file, together with the stress components.

4. RESULT AND DISCUSSION

This chapter presents the results of the microstructural analysis and the thermal simulation described in Chapter 3, and discusses what they show. It reports first the fibre geometry measured from the micro-computed-tomography scan, then the statistical distributions fitted to that geometry, then the representative volume element generated from those distributions, and finally the effective coefficient of thermal expansion and the residual stresses obtained by cooling that volume to the liquid-hydrogen storage temperature.

4.1 Microstructural characterisation results

The segmentation of the ten sub-volumes, validated in Section 3.2.4, gave a mean fibre volume fraction of 18.9%, ranging from 14.3% to 23.3% across the individual sub-volumes as listed in Table 3.2, against the nominal 20 per cent fibre content of the material. The variation between sub-volumes reflects the uneven local dispersion of fibres that is characteristic of a 3D printed short-fibre composite.

The fibre extraction described in Section 3.3 identified 307 fibres across the ten sub-volumes, distributed as given in Table 3.5, and each fibre was measured for its length, diameter and two orientation angles. The descriptive statistics of the pooled sample are summarised in Table 4.1.

Table 4.1 Descriptive statistics of the measured fibre geometry (n = 307 fibres).

Quantity	Mean	Median	Std dev	Minimum	Maximum
Length (μm)	147.6	126.4	110.1	14.0	678.2
Diameter (μm)	14.7	14.0	4.6	7.0	28.0
Elevation angle α (°)	−1.1	−0.4	15.6	−87.0	76.7
Azimuth angle β (°)	−1.9	−1.7	30.1	−89.3	88.0

The fibres are short and broadly distributed in length, with a mean of 148 micrometres over a range from 14 to 678 micrometres. Short fibres of this kind are typically produced by attrition during compounding and moulding, although the measured lengths are also limited by the size of the analysed sub-volume, since the longest fibre found, at 678 micrometres, is almost exactly the 679 micrometres extent of the

sub-volume along z. Fibres longer than the window are therefore truncated at its edge, so the upper end of the length range is set partly by the sub-volume size rather than by the fibre population alone. The diameters are far more tightly grouped, a mean of 14.7 micrometres and a median of 14 micrometres over a narrow range from 7 to 28 micrometres, and their restriction to a small set of discrete values is addressed in Section 4.2. The orientation is strongly concentrated about the reconstructed z axis. Most fibres have both the out-of-plane angle α and the in-plane angle β close to zero, so the population is dominated by fibres lying nearly along the print direction, as the fitted distributions in Section 4.2 show, with a sharp peak at zero and a small number of fibres at much larger angles. The scatter is greater in-plane than out-of-plane, the standard deviation of β being 30.1 degrees against 15.6 degrees for α, so the fibres deviate more within the x-z plane than out of it. The minority of fibres at large angles form small off-axis groups rather than a uniform spread, and these represent the fraction of the printed material that is not aligned with the raster.

4.2 Fitted statistical distributions

Each geometric quantity was fitted by the candidate distributions set out in Section 3.3.3 and the best fit selected by the Pearson chi-square test of Section 3.3.4. The adopted distribution and its fitted parameters for each quantity are given in Table 4.2.

Table 4.2 Adopted distribution and fitted parameters for each geometric quantity.

Quantity	**Adopted distribution**	**Fitted parameters**
Length	Weibull	shape k = 1.412, scale λ = 162.9 μm
Diameter	Empirical	nine discrete values (Table 4.4)
Elevation angle α	Generalised normal	location μ = −0.3°, scale α = 0.834, shape β = 0.439
Azimuth angle β	Laplace	location μ = −1.7°, scale b = 20.6°

The full comparison across the candidate distributions is given in Table 4.3. For the fibre length the Weibull distribution gave the best agreement, with a p-value of 0.73 against 0.51 for the gamma distribution, while the lognormal was rejected. For the elevation angle α only the generalised normal

distribution was accepted, with a p-value of 0.14; the normal and Laplace distributions were both rejected because the measured peak at zero is far sharper than either can represent, as their large chi-square values show. For the azimuth angle β the Laplace distribution gave the best fit at a p-value of 0.11, with the generalised normal also acceptable and the normal rejected.

Table 4.3 Pearson chi-square goodness-of-fit comparison of the candidate distributions. The degrees of freedom are the number of bins minus one minus the number of fitted parameters.

Quantity	Distribution	χ^2	df	p-value	Outcome
Length	Lognormal	16.31	6	0.012	rejected
	Gamma	5.30	6	0.506	not rejected
	Weibull	3.59	6	0.733	adopted
Elevation α	Normal	148.82	7	< 0.001	rejected
	Laplace	30.25	7	< 0.001	rejected
	Generalised normal	9.70	6	0.138	adopted
Azimuth β	Normal	54.02	7	< 0.001	rejected
	Laplace	11.74	7	0.110	adopted
	Generalised normal	11.84	6	0.066	not rejected

The quantile-quantile plots in Section 3.3.4 in Figure 3.18 support these results. For each adopted fit the points lie along the line of equality through the body of the data, departing from it only slightly and only in the extreme tails, which confirms that the fitted distributions describe the measured geometry well over the range that matters for the microstructure.

The diameter was not fitted with a continuous distribution. Because it is measured as twice the inscribed radius on a 3.5 micrometre voxel grid, it takes only the nine discrete values listed in Table 4.4, and it was represented directly by these values and their measured probabilities. The value of 14 micrometres dominates the distribution, accounting for 35% of the fibres.

Table 4.4 Empirical distribution of the fibre diameter over its nine measured values.

Diameter (µm)	Count	Probability
7.00	32	0.104

Diameter (μm)	Count	Probability
9.90	47	0.153
14.00	108	0.352
15.65	42	0.137
19.80	39	0.127
21.00	28	0.091
22.14	4	0.013
25.24	2	0.007
28.00	5	0.016

4.3 Homogenised coefficient of thermal expansion

Cooling the representative volume element from 293 K to 20 K, a temperature change of −273 K, produced the directional thermal strains and coefficients of thermal expansion given in Table 4.6. All three strains are negative, corresponding to contraction of between 1.50 and 1.75 per cent, and the secant coefficients of thermal expansion, defined as in Section 3.4 with the reference temperature taken as the RT stress-free state of 293 K, are correspondingly positive and of the order of 6×10^{-5}/K. The contraction of the volume over the cooldown is shown in Figure 4.1.

Table 4.5 Directional thermal strain and secant coefficient of thermal expansion over the cooldown from 293 K to 20 K, the coefficient being the secant value referred to the stress-free reference of 293 K.

Direction	Thermal strain	Coefficient of thermal expansion (K^{-1})
x	-1.505×10^{-2}	5.512×10^{-5}
y	-1.746×10^{-2}	6.395×10^{-5}
z	-1.698×10^{-2}	6.220×10^{-5}

The expansion is mildly anisotropic. It is largest in the y direction, at 6.40×10^{-5} per kelvin, which is the thin direction of the volume and, because the fibres lie close to the x-z plane, the direction in which fewest fibres are oriented and the matrix is therefore least restrained. The two in-plane directions are lower, at

5.51×10^{-5} per kelvin in x and 6.22×10^{-5} per kelvin in z. The difference between these two is small, and for a single realisation containing 54 fibres it should not be over-interpreted; a firmer statement about the in-plane anisotropy would require the ensemble of realisations discussed in Section 4.5.

The cooldown also locks in residual stress, which arises because the stiff basalt fibres, with their low coefficient of thermal expansion, contract far less than the compliant PA11 matrix and restrain it.

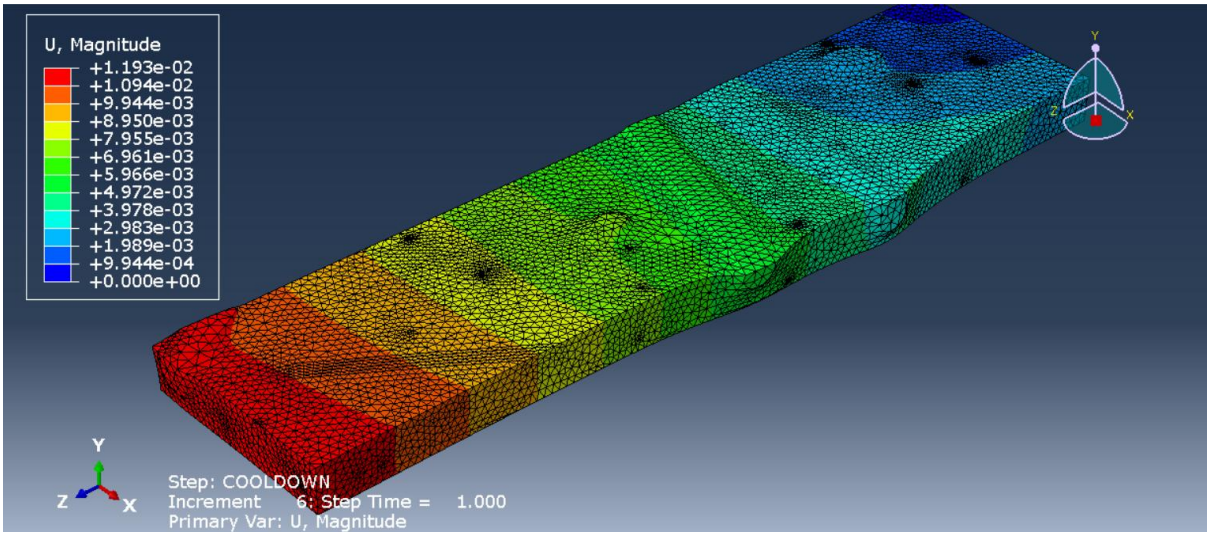


Figure 4.1 Displacement magnitude (U, in mm) over the RVE at the end of the cooldown from 293 K to 20 K, showing the thermal contraction. The fixed faces remain in place and the free faces displace most, reaching a peak of 1.19×10^{-2} mm. Deformation exaggerated 10× for clarity.

4.4 Sensitivity and limitations

Several of the modelling choices made in Chapter 3 limit the results reported above, and they set the direction for further work.

The material properties used below RT are engineering estimates rather than measured values. Only the 293 K row of Table 3.7 is taken from the literature; the values at 200, 100, 77 and 20 K were estimated, because no cryogenic property data were available for either the basalt fibre or the PA11 matrix. Since the predicted coefficient of thermal expansion depends strongly on the matrix stiffness, which is estimated to rise from about 1.3 GPa at 293 K to about 4.8 GPa at 20 K, and on the matrix expansion over the same interval, these estimates are the largest single source of uncertainty in the predictions. Replacing them with measured properties, whether from cryogenic testing of the constituents or from datasheet values covering the temperature range, is the first priority for improving the model, since the real thermal response cannot be obtained from estimated data.

The model also assumes a fully dense composite and contains no voids. In reality, moulded short-fibre composites always hold some porosity, from processing and from the fibre-matrix interfaces, and voids change the effective properties, lowering the stiffness and altering both the thermal contraction and the local stresses around them. They were left out here to keep the geometry tractable, but a representative model must include them, and adding a realistic void content, ideally measured from the same scan, is necessary before the predicted properties can be taken as those of the real material.

Periodic boundary conditions were omitted, and the model dimensions are quite small (only about 54 fibers in total). The three-fixed, three-free arrangement allows the volume to contract while removing rigid-body motion, and it gives a sound estimate of the free thermal contraction, but it does not enforce the periodicity that rigorous homogenisation requires. Imposing genuine periodic boundary conditions, which would need a matched mesh on opposite faces or a large set of constraint equations, is left as future work. Alternatively, a much bigger RVE with thousands of fibers could be used, but this would require the use of super-computers to be solved since the number of elements would be of millions.

The coefficient of thermal expansion reported here is drawn from a single realisation of the microstructure, generated with one random seed, which placed 54 fibres at a volume fraction of 20.10%. Only one realisation was run, because the available time did not allow more. A converged and fully defensible estimate would generate an ensemble of realisations from the same fitted distributions using different seeds, and report the mean and the spread of the predicted coefficient across them, the spread serving as a measure of both convergence and the representativeness of the volume. This is left as future work.

The representative volume is a single CT sub-volume and is thin in the y direction, at 35 micrometres against 161 and 679 micrometres in x and z, so its representativeness in that direction is limited. The fibres and matrix are also perfectly bonded, since the conforming mesh shares nodes across their interface, so no debonding of the fibre from the matrix on cooling is represented. In line with this, matrix plasticity is omitted, although this is less important since at cryogenic temperatures the matrix is generally brittle; but if the stresses are enough to cause yielding at temperatures close to RT, then the model may be overestimating the final stress states.

For this realisation the achieved volume fraction of 20.10% matched the 20% target closely, but this does not need to be always the case: in a thin domain packed with the larger fibre diameters, the Random Sequential Addition can approach jamming before the target is reached, and in that case, it is the achieved fraction, not the target, that describes the model.

5. CONCLUSIONS AND FURTHER DEVELOPMENTS

This thesis set out to predict the thermomechanical response of a short-fibre-reinforced polymer composite directly from its measured microstructure, and to do so through a single repeatable route that could be reapplied to other materials and fibre contents without a physical test for each one. The material chosen to demonstrate it was a short basalt-fibre-reinforced polyamide 11 composite, produced by additive manufacturing and considered as a candidate for the inner liner of a cryogenic liquid hydrogen tank within the OVERLEAF project. This chapter draws together what the work achieved (Section 5.1) and sets out the developments needed to turn it into a fully validated predictive tool (Section 5.2).

5.1 Main conclusions

The principal outcome of the thesis is the methodology itself. A complete pipeline was assembled and demonstrated, running from a single micro-computed-tomography scan, through the segmentation of the fibres and the measurement of their geometry, the statistical description of that geometry, the generation of a representative volume element that reproduces it, and finally the finite element homogenisation of that volume to obtain its thermal response on cooling. Each stage was validated in isolation before the next was built upon it, so that the route is reproducible from end to end rather than dependent on a single favourable case. No equivalent pipeline, proceeding from the direct tomographic measurement of a short-fibre composite to the prediction of its coefficient of thermal expansion and residual stresses at cryogenic temperature, had previously been reported for this material system.

The microstructure of the composite was measured rather than assumed. From ten sub-volumes a population of 307 fibres was extracted and characterised, giving a mean fibre volume fraction of about 19 per cent against the nominal 20 per cent of the material, and confirming a short, strongly aligned fibre architecture with its length broadly distributed and its orientation concentrated about the print direction. This geometry was reduced to a compact statistical description: a Weibull distribution for the fibre length, a generalised normal distribution for the out-of-plane angle, a Laplace distribution for the in-plane angle, and an empirical distribution for the diameter, whose resolution-limited values could not support a

continuous fit. Each fitted distribution was accepted on both a chi-square test and a quantile-quantile comparison, so that the microstructure could be regenerated from a handful of parameters.

Those parameters were used to build the representative volume element. A Monte Carlo procedure placed fibres drawn at random from the fitted distributions into the box by random sequential addition, reaching a fibre volume fraction of 20.1 per cent against the 20 per cent target with 54 non-intersecting fibres in the realisation carried forward. The whole generation and analysis was implemented as a single self-contained script whose statistical inputs and target volume fraction sit in one input block, so that a different sample, material or fibre content can be modelled by changing those numbers alone. This reusability, rather than any single result, is what the methodology is intended to provide, and it is what makes the planned study of other fibre fractions a change of input rather than a new model.

The thermal predictions follow from cooling this volume from RT to the storage temperature, a change of 273 kelvin. The composite contracted by between 1.5 and 1.75 per cent along its three axes, giving a directional secant coefficient of thermal expansion of the order of 6×10^{-5} per kelvin, referred to the RT stress-free state. The expansion was found to be mildly anisotropic, largest in the thin direction of the volume, where the fibres are fewest and the matrix least restrained, and lower in the plane in which the fibres predominantly lie. The cooldown also locks residual stresses into the material, since the stiff basalt fibres, with their far lower coefficient of thermal expansion, contract much less than the compliant polyamide 11 matrix and restrain it; it is these fibre-scale stresses that, in a real wall, drive the microcracking the design must avoid. Taken together, the results show that the effective thermal behaviour of the composite can be recovered from its measured microstructure within the virtual testing framework, although the values obtained should be read as provisional, for the reasons given below.

5.2 Further developments

The predictions rest on constituent properties that are only partly measured, and this is the first priority for further work. Only the RT values of the basalt fibre and the polyamide 11 matrix were taken from the literature; every value below RT was an engineering estimate, made because no cryogenic property data were available for either phase. Since the predicted coefficient of thermal expansion depends strongly on how the matrix stiffens and how both phases contract as they cool, replacing these estimates with measured or datasheet properties across the temperature range is the single change that would most improve confidence in the results.

The model also represents a fully dense composite. Voids are present in any moulded or printed short-fibre part, and although they are visible in the scan they were not quantified or included here, in order to keep the geometry tractable. Because porosity lowers the stiffness and alters both the contraction and the local stresses, a quantitative model should include a realistic void content, ideally measured from the same tomographic volume.

The mechanical boundary conditions were a set of roller constraints that hold the three faces at the origin against motion normal to themselves while leaving the opposite faces free. This arrangement removes rigid-body motion and allows the volume to contract freely, and it gives a sound estimate of the free thermal contraction, but it does not enforce the periodicity that rigorous homogenisation requires. Imposing genuine periodic boundary conditions, which would need a matched mesh on opposite faces or a large set of constraint equations, or alternatively analysing a much larger volume containing many more fibres, is left as future work.

The results reported here also come from a single realisation of the microstructure, generated with one random seed. A converged and fully defensible estimate would draw an ensemble of realisations from the same fitted distributions using different seeds, and report the mean and the spread of the predicted coefficient across them, the spread serving as a measure of both convergence and the representativeness of the chosen volume. In the same spirit, the completeness of the fibre extraction was not quantified, and establishing the detection rate against the visible fibres would put the measured statistics on a firmer footing.

Beyond these refinements, the natural continuation of the work is to exercise the methodology as it was designed to be used. With measured properties, voids and periodic conditions in place, the reusable script can be applied across the intended range of fibre volume fractions, extended from the coefficient of thermal expansion to the full effective stiffness, and used to represent the fibre-matrix debonding and matrix behaviour that the present perfectly bonded, linear-elastic model omits. Validated against experiment in due course, the pipeline would then serve not only this basalt-fibre composite but any short-fibre system for which a tomographic scan can be obtained.

REFERENCES

[1] S. Tiwari, M. J. Pekris, and J. J. Doherty, "A review of liquid hydrogen aircraft and propulsion technologies," *Int. J. Hydrog. Energy*, vol. 57, pp. 1174–1196, Feb. 2024, doi: 10.1016/j.ijhydene.2023.12.263.

[2] E. Rivard, M. Trudeau, and K. Zaghib, "Hydrogen Storage for Mobility: A Review," *Materials*, vol. 12, no. 12, p. 1973, Jun. 2019, doi: 10.3390/ma12121973.

[3] W. L. Johnson, E. Baltman, and F. D. Koci, "Assessment of insulation systems for aircraft liquid hydrogen tanks," *IOP Conf. Ser. Mater. Sci. Eng.*, vol. 1301, no. 1, p. 012062, May 2024, doi: 10.1088/1757-899X/1301/1/012062.

[4] D. Terlizzi, A. Bamoshmoosh, and G. Valenti, "Review of liquid hydrogen tanks for short- and medium-haul aircraft," in *9th European Congress on Computational Methods in Applied Sciences and Engineering*, CIMNE, 2024. doi: 10.23967/eccomas.2024.249.

[5] N. Liu *et al.*, "Progress in research on composite cryogenic propellant tank for large aerospace vehicles," *Compos. Part Appl. Sci. Manuf.*, vol. 143, p. 106297, Apr. 2021, doi: 10.1016/j.compositesa.2021.106297.

[6] F. Huang *et al.*, "Cryogenic Performance and Modelling of Fibre- and Nano-Reinforced Composites: Failure Mechanisms, Toughening Strategies, and Constituent-Level Behaviour," *J. Compos. Sci.*, vol. 10, no. 1, p. 36, Jan. 2026, doi: 10.3390/jcs10010036.

[7] M. S. Islam, L. F. Benninger, G. Pearce, and C.-H. Wang, "Toughening carbon fibre composites at cryogenic temperatures using low-thermal expansion nanoparticles," *Compos. Part Appl. Sci. Manuf.*, vol. 150, p. 106613, Nov. 2021, doi: 10.1016/j.compositesa.2021.106613.

[8] N. Arkema, "Rilsan polyamide 11."

[9] F. Huang *et al.*, "Microcracking resistance of 3D printed fibre composites at cryogenic temperatures," *Addit. Manuf.*, vol. 89, p. 104307, Jun. 2024, doi: 10.1016/j.addma.2024.104307.

[10] M. Barczewski *et al.*, "The Recyclability of Fire-Retarded Biobased Polyamide 11 (PA11) Composites Reinforced with Basalt Fibers (BFs): The Influence of Reprocessing on Structure, Properties, and Fire Behavior," *Molecules*, vol. 29, no. 13, p. 3233, Jul. 2024, doi: 10.3390/molecules29133233.

[11] H. H. Farghal and T. M. Madkour, "Basalt Fiber Composites: Structure, Properties, Sustainability, and Life Cycle Analysis," *J. Compos. Sci.*, vol. 10, no. 5, p. 253, May 2026, doi: 10.3390/jcs10050253.

[12] E. Kessler, R. Gadow, J. Straub, and 1 NuCellSys GmbH, Neue Strasse 95, D-73230 Kirchheim u. Teck, Germany, "Basalt, glass and carbon fibers and their fiber reinforced polymer composites under thermal and mechanical load," *AIMS Mater. Sci.*, vol. 3, no. 4, pp. 1561–1576, 2016, doi: 10.3934/matersci.2016.4.1561.

[13] V. Gigante, F. Cartoni, B. Dal Pont, and L. Aliotta, "Extrusion Parameters Optimization and Mechanical Properties of Bio-Polyamide 11-Based Biocomposites Reinforced with Short Basalt Fibers," *Polymers*, vol. 16, no. 21, p. 3092, Oct. 2024, doi: 10.3390/polym16213092.

[14] S. Yu, H. Bale, S. Park, J. Y. Hwang, and S. H. Hong, "Anisotropic microstructure dependent mechanical behavior of 3D-printed basalt fiber-reinforced thermoplastic composites," *Compos. Part B Eng.*, vol. 224, p. 109184, Nov. 2021, doi: 10.1016/j.compositesb.2021.109184.

[15] R. M. Auenhammer *et al.*, "Fibre orientation distribution function mapping for short fibre polymer composite components from low resolution/large volume X-ray computed tomography," *Compos. Part B Eng.*, vol. 275, p. 111313, Apr. 2024, doi: 10.1016/j.compositesb.2024.111313.

[16] L. Jiang, S. Xiao, J. Wu, Z. Liao, G. Zhu, and B. Zhang, “CT and image post-processing for fiber composites: Defect analysis, deep learning, digital volume correlation, and FE simulation – A review,” *Mater. Des.*, vol. 264, p. 115698, Apr. 2026, doi: 10.1016/j.matdes.2026.115698.

[17] J. LLorca *et al.*, “Multiscale Modeling of Composite Materials: a Roadmap Towards Virtual Testing,” *Adv. Mater.*, vol. 23, no. 44, pp. 5130–5147, Nov. 2011, doi: 10.1002/adma.201101683.

[18] O. project, “Novel low-pressure cryogenic liquid hydrogen storage for aviation.” [Online]. Available: https://cordis.europa.eu/project/id/101056818

[19] J. A. Gómez and D. M. F. Santos, “The Status of On-Board Hydrogen Storage in Fuel Cell Electric Vehicles,” *Designs*, vol. 7, no. 4, p. 97, Aug. 2023, doi: 10.3390/designs7040097.

[20] Y. Su, H. Lv, W. Zhou, and C. Zhang, “Review of the Hydrogen Permeability of the Liner Material of Type IV On-Board Hydrogen Storage Tank,” *World Electr. Veh. J.*, vol. 12, no. 3, p. 130, Aug. 2021, doi: 10.3390/wevj12030130.

[21] S. Khan and A. Kumar, “Manufacturing Challenges in Advanced Cylindrical Composite Pressure Vessels for Hydrogen Storage: A Comprehensive Review,” *Energy Storage*, vol. 7, no. 7, p. e70263, Oct. 2025, doi: 10.1002/est2.70263.

[22] T. Q. Hua *et al.*, “Technical assessment of compressed hydrogen storage tank systems for automotive applications,” *Int. J. Hydrog. Energy*, vol. 36, no. 4, pp. 3037–3049, Feb. 2011, doi: 10.1016/j.ijhydene.2010.11.090.

[23] G. Souza and J. Tarpani, “Using OBR for pressure monitoring and BVID detection in type IV composite overwrapped pressure vessels,” *J. Compos. Mater.*, vol. 55, no. 3, pp. 423–436, Feb. 2021, doi: 10.1177/0021998320951616.

[24] R. A. Schapery, “Thermal Expansion Coefficients of Composite Materials Based on Energy Principles,” *J. Compos. Mater.*, vol. 2, no. 3, pp. 380–404, Jul. 1968, doi: 10.1177/002199836800200308.

[25] M. H. Zamri, H. M. Akil, S. Safiee, Z. A. M. Ishak, and A. A. Bakar, “Predicting the Coefficient of Thermal Expansion of Pultruded Composites with a Natural-Fiber Reinforcement,” *Mech. Compos. Mater.*, vol. 50, no. 5, pp. 603–612, Nov. 2014, doi: 10.1007/s11029-014-9448-5.

[26] T. Mori and K. Tanaka, “Average stress in matrix and average elastic energy of materials with misfitting inclusions,” *Acta Metall.*, vol. 21, no. 5, pp. 571–574, May 1973, doi: 10.1016/0001-6160(73)90064-3.

[27] J. D. Eshelby, “The determination of the elastic field of an ellipsoidal inclusion, and related problems,” *Proc. R. Soc. Lond. Ser. Math. Phys. Sci.*, vol. 241, no. 1226, pp. 376–396, Aug. 1957, doi: 10.1098/rspa.1957.0133.

[28] C. Dong, “Coefficient of Thermal Expansion of Single-Wall Carbon Nanotube Reinforced Nanocomposites,” *J. Compos. Sci.*, vol. 5, no. 1, p. 26, Jan. 2021, doi: 10.3390/jcs5010026.

[29] X. Long, T. Su, Z. Chen, Y. Su, and K. S. Siow, “Tunable Coefficient of Thermal Expansion of Composite Materials for Thin-Film Coatings,” *Coatings*, vol. 12, no. 6, p. 836, Jun. 2022, doi: 10.3390/coatings12060836.

[30] J. J. Liu, L. J. Yao, B. Li, and X. Y. Tong, “Study on the Influence of Manufacturing Defects on Coefficient of Thermal Expansion of Plain Weave C/SiC,” *Adv. Mater. Res.*, vol. 502, pp. 56–59, Apr. 2012, doi: 10.4028/www.scientific.net/AMR.502.56.

[31] Y. Li *et al.*, “Cryogenic damage mechanisms of CFRP laminates based on in-situ X-ray computed tomography characterization,” *Compos. Sci. Technol.*, vol. 247, p. 110413, Mar. 2024, doi: 10.1016/j.compscitech.2023.110413.

[32] K. Fujishiro, T. Ogasawara, K. Mizutani, H. Kumazawa, and T. Aoki, “Microscopic damage behavior in CFRP cross-ply laminates at cryogenic temperature,” *Compos. Sci. Technol.*, vol. 256, p. 110774, Sep. 2024, doi: 10.1016/j.compscitech.2024.110774.

[33] M. Salgado, J. M. Guerrero, L. Carreras, and J. Renart, “An Automated Image Processing Method to Detect Progressive Matrix Cracking in CFRP Composites Using X-Ray Micro-Computed Tomography,” *J. Nondestruct. Eval.*, vol. 45, no. 3, p. 104, Sep. 2026, doi: 10.1007/s10921-026-01387-x.

[34] O. Vallmajó, A. Arteiro, J. M. Guerrero, A. R. Melro, A. Pupurs, and A. Turon, “Micromechanical analysis of composite materials considering material variability and microvoids,” *Int. J. Mech. Sci.*, vol. 263, p. 108781, Feb. 2024, doi: 10.1016/j.ijmecsci.2023.108781.

[35] B. A. Bednarcyk, B. L. Hearley, and E. J. Pineda, “Multiscale Modeling of Thermoplastic Matrix Composites for Cryogenic Hydrogen Storage Applications,” *Modelling*, vol. 6, no. 4, p. 151, Nov. 2025, doi: 10.3390/modelling6040151.

[36] Z. Blackman *et al.*, “Sustainable basalt fiber reinforced polyamide 6,6 composites: Effects of fiber length and fiber content on mechanical performance,” *Compos. Part C Open Access*, vol. 14, p. 100495, Jul. 2024, doi: 10.1016/j.jcomc.2024.100495.

[37] G. Sun, S. Tong, D. Chen, Z. Gong, and Q. Li, “Mechanical properties of hybrid composites reinforced by carbon and basalt fibers,” *Int. J. Mech. Sci.*, vol. 148, pp. 636–651, Nov. 2018, doi: 10.1016/j.ijmecsci.2018.08.007.

[38] S.-Y. Fu, X. Hu, and C.-Y. Yue, “EFFECTS OF FIBER LENGTH AND ORIENTATION DISTRIBUTIONS ON THE MECHANICAL PROPERTIES OF SHORT-FIBER-REINFORCED POLYMERS,” *J. Soc. Mater. Sci. Jpn.*, vol. 48, no. 6Appendix, pp. 74–83, 1999, doi: 10.2472/jsms.48.6Appendix_74.

[39] C. T. Sun and R. S. Vaidya, “Prediction of composite properties from a representative volume element,” *Compos. Sci. Technol.*, vol. 56, no. 2, pp. 171–179, Jan. 1996, doi: 10.1016/0266-3538(95)00141-7.

[40] X. Deng, M. S. Hoo, Y. W. Cheah, and L. Q. N. Tran, “Processing and Mechanical Properties of Basalt Fibre-Reinforced Thermoplastic Composites,” *Polymers*, vol. 14, no. 6, p. 1220, Mar. 2022, doi: 10.3390/polym14061220.

[41] M. Y. Shiino, F. M. Monticeli, and M. V. Donadon, “Limited strength of short fiber composites: Identification of variables affecting the critical fiber length,” *J. Compos. Mater.*, vol. 57, no. 11, pp. 1927–1940, May 2023, doi: 10.1177/00219983231166565.

[42] R. Hill, “Elastic properties of reinforced solids: Some theoretical principles,” *J. Mech. Phys. Solids*, vol. 11, no. 5, pp. 357–372, Sep. 1963, doi: 10.1016/0022-5096(63)90036-X.

[43] S. Firooz, S. Saeb, G. Chatzigeorgiou, F. Meraghni, P. Steinmann, and A. Javili, “Systematic study of homogenization and the utility of circular simplified representative volume element,” *Math. Mech. Solids*, vol. 24, no. 9, pp. 2961–2985, Sep. 2019, doi: 10.1177/1081286518823834.

[44] H. Shen and L. C. Brinson, “A numerical investigation of the effect of boundary conditions and representative volume element size for porous titanium,” *J. Mech. Mater. Struct.*, vol. 1, no. 7, pp. 1179–1204, Nov. 2006, doi: 10.2140/jomms.2006.1.1179.

[45] T. Kanit, S. Forest, I. Galliet, V. Mounoury, and D. Jeulin, “Determination of the size of the representative volume element for random composites: statistical and numerical approach,” *Int. J. Solids Struct.*, vol. 40, no. 13–14, pp. 3647–3679, Jun. 2003, doi: 10.1016/S0020-7683(03)00143-4.

[46] K. Breuer and M. Stommel, “RVE modelling of short fiber reinforced thermoplastics with discrete fiber orientation and fiber length distribution,” *SN Appl. Sci.*, vol. 2, no. 1, p. 91, Jan. 2020, doi: 10.1007/s42452-019-1890-5.

[47] S. G. Advani and C. L. Tucker, “The Use of Tensors to Describe and Predict Fiber Orientation in Short Fiber Composites,” *J. Rheol.*, vol. 31, no. 8, pp. 751–784, Nov. 1987, doi: 10.1122/1.549945.

[48] S. C. Garcea, Y. Wang, and P. J. Withers, “X-ray computed tomography of polymer composites,” *Compos. Sci. Technol.*, vol. 156, pp. 305–319, Mar. 2018, doi: 10.1016/j.compscitech.2017.10.023.

[49] C. Paltán, J. Costa, and J. Fajardo, "Computed Tomography of Polymer Composites Reinforced with Natural Short Fiber," in *Computational Science and Its Applications – ICCSA 2019*, vol. 11623, S. Misra, O. Gervasi, B. Murgante, E. Stankova, V. Korkhov, C. Torre, A. M. A. C. Rocha, D. Taniar, B. O. Apduhan, and E. Tarantino, Eds., in Lecture Notes in Computer Science, vol. 11623. , Cham: Springer International Publishing, 2019, pp. 452–467. doi: 10.1007/978-3-030-24308-1_37.

[50] S. M. García-Rodríguez, J. Costa, V. Singery, I. Boada, and J. A. Mayugo, "The effect interleaving has on thin-ply non-crimp fabric laminate impact response: X-ray tomography investigation," *Compos. Part Appl. Sci. Manuf.*, vol. 107, pp. 409–420, Apr. 2018, doi: 10.1016/j.compositesa.2018.01.023.

[51] C. Breite *et al.*, "A synchrotron computed tomography dataset for validation of longitudinal tensile failure models based on fibre break and cluster development," *Data Brief*, vol. 39, p. 107590, Dec. 2021, doi: 10.1016/j.dib.2021.107590.

[52] J. Schindelin *et al.*, "Fiji: an open-source platform for biological-image analysis," *Nat. Methods*, vol. 9, no. 7, pp. 676–682, Jul. 2012, doi: 10.1038/nmeth.2019.

[53] D. Legland, I. Arganda-Carreras, and P. Andrey, "MorphoLibJ: integrated library and plugins for mathematical morphology with ImageJ," *Bioinformatics*, vol. 32, no. 22, pp. 3532–3534, Nov. 2016, doi: 10.1093/bioinformatics/btw413.

[54] C. Composites, "CX Composites, 'Basalt chopped fibre,' technical data sheet."

[55] M. Bahrami, J. Abenojar, and M. A. Martínez, "Comparative Characterization of Hot-Pressed Polyamide 11 and 12: Mechanical, Thermal and Durability Properties," *Polymers*, vol. 13, no. 20, p. 3553, Oct. 2021, doi: 10.3390/polym13203553.

Appendix

1. Binarization Macro: https://drive.google.com/file/d/1eUoQgdfGfM5ZNQvVrGEUv0cp-7IVqYX7/view?usp=sharing
2. Fibre tracker tool: https://drive.google.com/file/d/1KvQ2qicyAwFbRJS6bQDJUvhP_Kji4PO0/view?usp=sharing
3. Napari viewer: https://drive.google.com/file/d/1b8rS6c1E2k-rVSIcOfeIIDnz2-JsqjX2/view?usp=sharing